PON Ricerca e Innovazione 2014- 2020
Unione Europea
Ministero dell'Istruzione, dell'Università e della Ricerca

Università degli Studi di Napoli Federico II

Use of advanced microscopy and microfluidics to study liquid process transformations in wormlike micellar systems

Carla Caiazza

A research project sponsored by
Procter&Gamble

Supervised by:
Prof. Stefano Guido
Dr. Denis O'Sullivan
Vincenzo Guida

A thesis presented for the degree of Doctor of Philosophy in Industrial Products and Processes Engineering

January 2018

Contents

Abstract

During the last decades, solutions of wormlike micelles have been successfully used in a number of diverse applications, for instance as proppants in oil industry, drag-reduction agents, heat-transfer fluids, and carrier in drug-delivery systems.

One of the most extensive use of wormlike micelles is as additives in a wide variety of consumer goods, including hard-surface cleaners, dish-wash and laundry-detergents, body-soaps and shampoos. In fact, thanks to their reological properties, they act as thickener in such products, thereby ensuring the possibility to properly tune the viscoelastic behaviour of the final formulation. This is a particularly critical aspect for home-care and personal-care products, as high viscosity is desired to increase their stability, and to suspend particles, colorants and perfumes in the solution; on the other hand, elastic properties are required to ensure a proper dosage of the product, which otherwise couldn't flow through the pump of a dispenser, or would form filaments after being squeezed out of a bottle; finally, viscoelastic products appear more appealing to consumers.

The widespread utilization of wormlike micelles is at the base of an huge industrial interest in understanding the flow-behaviour of these solutions. In fact, a constitutive model which describes these systems would allow a predictive analysis and modelling of the operation-

units involved in manufacturing processes, such as pipes, tanks and static mixers, pumps and injector-nozzles, giving the possibility to predict industrially-relevant quantities, such as blending and pressure-drop.

On the other hand, wormlike micellar systems generated a considerable interest in the basic research world, thanks to their rheological and flow-properties, characterized by the occurrence of several flow-instabilities, some of which haven't been observed in other complex fluids, and which look ubiquitous in such systems. In fact, due to the effect of the flow-deformation on the microstructure of the solution, wormlike micelles show a complex non-linear flow-behaviour even under very simple flow-conditions.

Nowadays, many of these flow-induced phenomena have been extensively reported in a variety of systems, and studied by varying the physico-chemical parameters of the solution, the flow-conditions, and the analytical techniques. In spite of all these efforts, there is still no constitutive model which allows one to predict the onset of flow-instabilities under strong-flows. In fact, the physical nature of these phenomena have not been fully elucidated yet, and, even if several mechanisms have been proposed, the debate is still open.

In this scenario, microfluidics has emerged in the last decade as a powerful tool to get a deeper insight into the flow-behaviour of wormlike micellar solutions. In addition to the well-known advantages allowed from this techniques - low costs, chemical consumption and experimental time, and small space required for the setup - microfluidic devices show features which make them an elite instrument to investigate wormlike micellar solutions, as the high confinement of the flow-geometry facilitates the onset of the surface-force driven instabilities; furthermore, they can easily be coupled with many optical

techniques, enabling unique flow-visualization possibilities.

Here, microfluidics is coupled with advanced microscopy, in order to get a deeper insight into the flow-behaviour of a wormlike micellar model system. Thanks to direct visualization of the flowing solution, the onset of flow-induced structuring has been detected, and its effects on the velocity-profiles have been analysed. The effects of confinement are then analysed by scaling the flow-geometry up to pilot-scale.

On the other hand, a complete rheological characterization of the model system is reported. By matching several measurement-techniques, a new approach to high-shear rheology is implemented. The measurements so-obtained, together with a complete study of the wall-slip behaviour of the solution, are then used to model the flowing solution, by using the a software for computational fluid dynamics (CFD) analysis. The prediction of this analysis are then compared to experimental results.

Lastly, the onset of demixing-phenomena has been detected in a complex microfluidic device, by coupling microfluidics, rotational rheometry, electrical-conductivity and dry-mass measurements.

Chapter 1

Introduction

1.1 From surfactants to wormlike micelles

Surfactants are amphiphilic molecules, as they contain both a small hydrophilic-group, referred to as 'head', and a hydrophobic-group, generally consisting in a relatively-short hydrocarbon-chain, referred to as 'tail'.

When a small amount of surfactant molecules are added to an aqueous solution, they preferably locate at the water/air interface, with the head-groups surrounded by water molecules, and the tail-groups in air. This phenomenon, known as surfactant adsorption at the interface, minimizes the contact between the hydrophobic tail-groups and the water molecules. Thanks to the strong interaction between the tails and the air, and the heads and the water, the interfacial-tension of the system decreases.

In reality, not all the surfactant molecules move towards the interface. In fact, despite the repulsion between the tails and the water, the solvation of the molecules would result in a less-ordered system, with a higher entropy. Thus, in order to minimize the free energy of the

system, surfactant molecules at the interface and in the bulk are in a dynamic-equilibrium.

As surfactant is progressively added to the solution, the interface saturates and the overall entropy-increment due to the molecules in the bulk becomes smaller and smaller, up to a surfactant concentration at which this increment is not big enough to ensure the molecules-solvation anymore. This threshold-value of the concentration is referred to as 'critical micelle concentration' (cmc). Over this value, surfactant molecules spontaneously self-assemble in supramolecular aggregates, in such way that there are only head-groups at the water/surfactant interface, while the tails are isolated from water, being turned inwards the micelle (Fig.1.1). The number of surfactant molecules in each micelle is known as aggregation number, N.

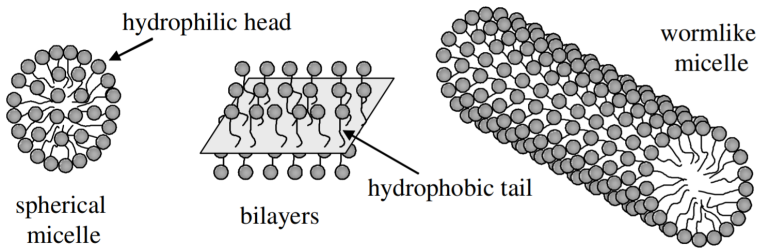

Fig. 1.1: *Various surfactant self-assembled structures: spherical micelle, bilayers, and wormlike micelle (adapted from [96])*

In self-assembling processes, a sphere is the most favoured morphology, as it ensures the minimum interface-area to volume ratio, and the minimum aggregation number. Despite this, sometimes the conditions required for aggregation in spherical micelles are not met. In fact, regardless of the micelle morphology, the aggregation number can be evaluated both as the ratio between the surface-area of the micelle and that of the surfactant head-group (a_s), and as the ratio be-

tween the volume of the micelle and that of the surfactant. As this latter is approximately equal to the volume of the hydrophobic-group (v), in a spherical micelle of radius R

$$N = \frac{4\pi R^2}{a_s} = \frac{4\pi R^3}{3v} \tag{1.1}$$

hence

$$\frac{v}{Ra_s} = \frac{1}{3} \tag{1.2}$$

The radius of the aggregate can't exceed the maximum extended length of the hydrophobic-tail (l). In fact, if $R > l$, the micelle would be characterized by an empty-core. Thus, the formation of a spherical micelle can only occur when the constraint

$$\frac{v}{la_s} \leq \frac{1}{3} \tag{1.3}$$

is satisfied, for instance when the surfactant has a large head group or a small tail.

The ratio $v/(la_s)$ is referred to as packing parameter [59], and allows one to give a good prediction on the morphology of the aggregates in a solution. When $v/(la_s) > 1/3$, surfactant molecules self-assemble in elongated micelles, named rods, constituted by a cylindrical elongated-body and two hemispherical endcaps, whose diameter can be larger than that of the cross-section of the body [81]. A rod-like micelle is referred to as wormlike micelle, when its overall length is much greater than its persistence length [114], which is the minimum distance between two parts of the micelle whose orientations are completely uncorrelated. By following the same reasoning applied to spherical micelles, it can be demonstrated that the self-assembly in such micelles would require an empty-core if $v/(la_s) > 1/2$. Thus, when this happens, surfactant molecules self-assemble in more complex geometries, such as vesicles and bilayers [18, 26, 79, 111, 122].

Although the packing parameter only takes into account the shape of the single surfactant molecules, a number of physico-chemical parameters, such as the pH and the temperature of the solution, the surfactant and salt concentrations and chemistry, and the flow-conditions [16, 59, 81, 118, 122], affect the molecule-geometry, and thus the morphology of the micelles. For instance, Fig.1.2 shows how salt concentration causes micelle growth and entanglement.

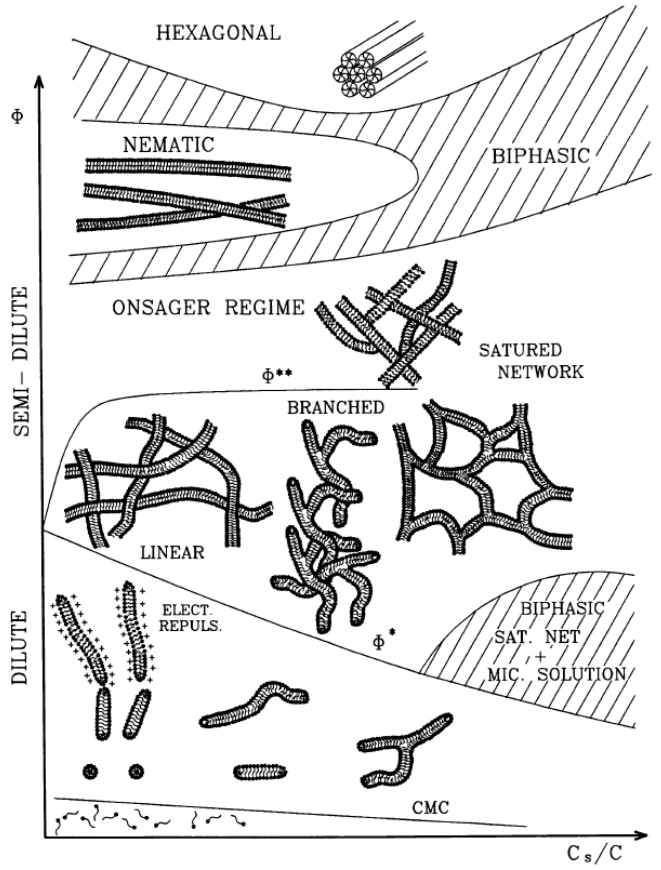

Fig. 1.2: *Effect of surfactant volume fraction (ϕ) and ratio of salt and surfactant molar concentrations (C_s/C) on micellar morphology [70]*

In fact, in the dilute regime, an increase of the salt concentration

induces the transition from small aggregates to linear and eventually branched rods; in the semi-dilute regime, instead, this growth results in branching of the wormlike micelles, up to the formation of multi-connected structures and, finally, a saturated network; lastly, ordered phases are reported in literature, as effect of phase-separation [70].

1.2 Wormlike micelles as living polymers

As mentioned, under specific physico/chemical conditions, one-dimensional growth of surfactant-based micelles results in long and semi-flexible cylindrical-aggregates, referred to as wormlike micelles.

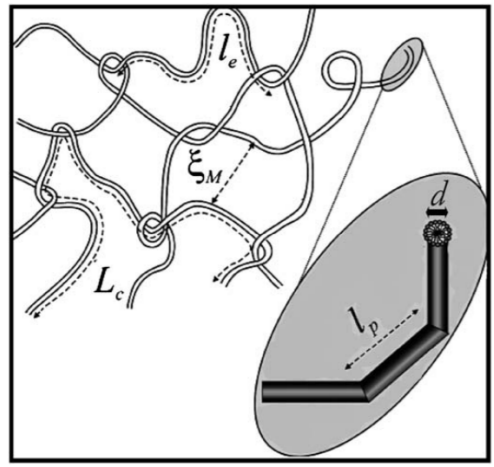

Fig. 1.3: *Characteristic lengths of a network of wormlike micelles [73]*

Fig.1.3 depicts a schematic representation of a wormlike micellar network and its characteristic structural-parameters:

- the cross-section radius, r_{cs}, is the radius of the section of the cylindrical-body of the micelle;
- the persistence length, l_p, is, as already defined, the minimum

distance between two parts of the micelle whose orientations are completely uncorrelated;

- the contour length, L_c, is the overall curvilinear length of the micelle; in a network, $\bar{L}_c$ is the average value of the contour lengths of all the micelles;
- the entanglement length, l_e, is the curvilinear distance between two entanglement points in the network;
- the mesh size, ξ_M, or the average distance between two micelles.

Tab.1.1 reports the characteristic lengths of a wormlike micellar solution of cetyltrimethylammonium bromide (CTAB) and sodium salicylate, as a function of temperature and R = [NaSal]/[CTAB].

Tab. 1.1: *Characteristic lengths of a 0.01M CTAB solution as a function of temperature and R (adapted from [43])*

R, -	**T, °C**	ξ_M, nm	l_p, **nm**	l_e, **nm**	$\bar{L}_c$, **nm**
0.4	20	45	36	51	4865
0.4	22	47	45	49	2782
1.0	22	40	34	75	933
1.0	25	40	30	48	455
1.5	20	41	29	51	1282
1.5	22	41	29	52	884
1.5	25	39	29	47	612
2.0	20	35	29	39	1517
2.0	22	35	29	40	1216
2.0	25	37	29	44	869
4.0	22	39	33	46	408

Wormlike micelles morphology resembles the one of polymers; furthermore, their rheological-behaviour is similar to that of a visco-

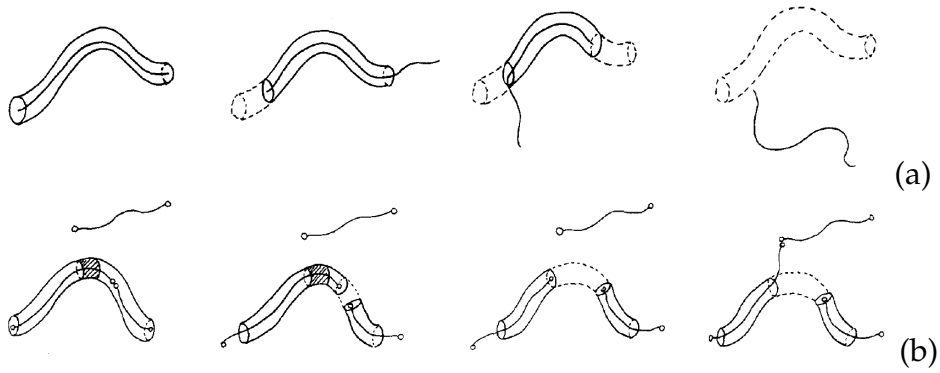

Fig. 1.4: *Reptation of a polymer chain (a), and relaxation of a wormlike micelle undergoing both reptation and scission/recombination reactions (b) (adapted from [21])*

elastic-polymer solutions [93]. Despite these analogies, wormlike micelles and polymers are quite different: in a polymer, monomers are chemically-bonded together, whereas in a self-assembled aggregate, surfactant molecules are weakly-held together by physical attractions, so that wormlike micelles are in a dynamic-equilibrium, continuously undergoing scission and recombination reactions. This ability to break and reform gives the micelles additional mechanisms for stress-relief in respect of those characterizing the polymers, such as the reptation (Fig.1.4). Because of this difference, wormlike micelles are commonly referred to as 'equilibrium polymers' or 'living polymers'.

1.3 Linear rheology

1.3.1 Cates model

In 1987, Cates developed a model to describe the linear rheology of entangled wormlike micelles, modifying the Doi-Edwards model

for entangled polymers, by taking into account the effects of scission/recombination reactions (Fig.1.5).

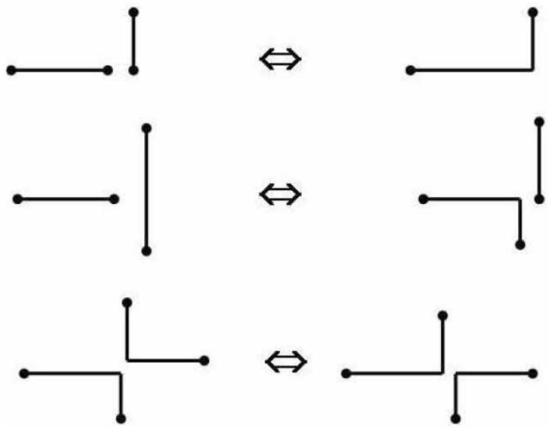

Fig. 1.5: *Main types of scission/recombination reactions: top, reversible-scission; middle, end-interchange; bottom, bond-interchange [23]*

Two assumptions underlie this model:

- chain-scission occurs at any point on the chain with the same probability per unit of time and length, and the rate of its reverse-reaction - i.e. chain-recombination - is just proportional to the product of the concentrations of the two reacting-subchains;
- after a chain-breakage, a subchain recombines with the one it is detached from or with another randomly-chosen one, with the same probability.

Furthermore, tube-evaporation is considered to be negligible. In fact, Turner et al. [108] suggest that this mechanisms becomes important only in very-rapid-reaction limit, i.e when $\tau_{br}/\tau_{rep} \lesssim (l_e/\bar{L}_c)^{3/2}$.

When all these assumptions hold, an exponential size-distribution of the micelles is predicted, whether they are linear or branched [23],

by:

$$c(L) \propto \exp\left[-\frac{L_c}{\bar{L}_c}\right], \quad \bar{L}_c \propto \varphi^n \exp\left[\frac{\beta E}{2}\right], \quad \beta = \frac{1}{k_B T} \tag{1.4}$$

where E is the free energy of both the endcaps in a linear micelle, or of each crosslink in a branched one, φ is the volume-fraction of the surfactant, and n is a parameter related to the morphology of the micelle (for instance, $n = 1/2$ for linear micelles).

Depending on the relative values of the characteristic relaxation-time through reptation (τ_{rep}) and through breakage/recombination (τ_{br}), Cates model predicts several dynamic-regimes, with characteristic time τ:

- when $\tau_{br}/\tau_{rep} > 1$, all the scission and recombination-reactions are slow, thus the main mechanism of stress-relaxation is the reptation; in this regime, the micellar solution behaves as a polymer solution, and $\tau = \tau_{rep}$;
- when $l_e/\bar{L}_c < \tau_{br}/\tau_{rep} < 1$, i.e. in the fast-reaction limit, the behaviour of the solution is described by the Maxwell model with a single relaxation-time (sec.1.3.2), $\tau = \sqrt{\tau_{rep}\tau_{br}}$, exhibiting a monoexponential stress-relaxation and a linear creep response;
- when $(l_e/\bar{L}_c)^3 < \tau_{br}/\tau_{rep} < l_e/\bar{L}_c$, relaxation is dominated by breathing-fluctuations, and $\tau = \tau_{rep}^{1/4}\tau_{br}^{3/4}(l_e/\bar{L}_c)^{-1/4}$;
- when $\tau_{br}/\tau_{rep} < (l_e/\bar{L}_c)^3$, relaxation is dominated by local Rouse-like modes, and $\tau = \tau_{rep}^{1/2}\tau_{br}^{1/2}(l_e/\bar{L}_c)^{1/2}$.

Later on, Cates et al. [76, 107, 108] studied the effect of both end-interchange and bond-interchange reactions (Fig.1.5), reporting that:

- they don't affect the polydispersity of the micelles;
- the end-interchange shows the same relaxation-dynamics of the reversible scission with the same time, τ_{br};
- the bond-interchange slows down the dynamics in both fast-reaction and breathing regime, and affects the value of τ_{rep}/τ_{br}

at which they arise:

- the fast-reaction limit occurs when $(l_e/\bar{L}_c)^{3/2} < \tau_{br}/\tau_{rep} < < 1$, and $\tau = \tau_{rep}^{2/3}\tau_{br}^{1/3}$;
- the breathing regime occurs when $(l_e/\bar{L}_c)^4 < \tau_{br}/\tau_{rep} < < (l_e/\bar{L}_c)^{3/2}$, and $\tau = \tau_{rep}^{2/5}\tau_{br}^{3/5}(l_e/\bar{L}_c)^{-2/5}$.

1.3.2 Maxwell model

The multi-mode Maxwell model empirically describes the relaxation-modulus of a fluid, $G(t)$, by using a sum of exponential functions:

$$G(t) = \sum_{i=1}^{N} G_i e^{-t/\tau_i} \tag{1.5}$$

where τ_i are the discrete relaxation-times and G_i are the moduli of the fluid. The set of (τ_i, G_i) couples is called discrete relaxation-spectrum.

It's possible to describe the response of a Maxwellian fluid to small-angle oscillatory shear (SAOS), by coupling the Eq.1.5 with the definitions of storage and loss moduli, respectively:

$$G'(\omega) \equiv \omega \int_0^\infty \sum_{i=1}^{N} G_i e^{-t/\tau_i} sin(\omega t) dt = \sum_{i=1}^{N} \frac{G_i(\omega\tau_i)^2}{1+(\omega\tau_i)^2} \tag{1.6}$$

$$G''(\omega) \equiv \omega \int_0^\infty \sum_{i=1}^{N} G_i e^{-t/\tau_i} cos(\omega t) dt = \sum_{i=1}^{N} \frac{G_i(\omega\tau_i)}{1+(\omega\tau_i)^2} \tag{1.7}$$

As predicted by the Cates model, in the fast-reaction limit, the linear viscoelastic-response of a wormlike micellar solution can often be described by a single-mode Maxwell model [4, 91, 92, 95, 102, 110], with relaxation time $\tau = \sqrt{t_{rep}t_{br}}$. Hence

$$G(t) = G_0 e^{-t/\tau} \tag{1.8}$$

and

$$G'(\omega) = G_0 \frac{(\omega\tau)^2}{1+(\omega\tau)^2}; \quad G''(\omega) = G_0 \frac{\omega\tau}{1+(\omega\tau)^2} \tag{1.9}$$

where G_0 is the plateau modulus.

As shown in Fig1.6, at low angular-frequency the single-mode Maxwell model is in good agreement with the data.

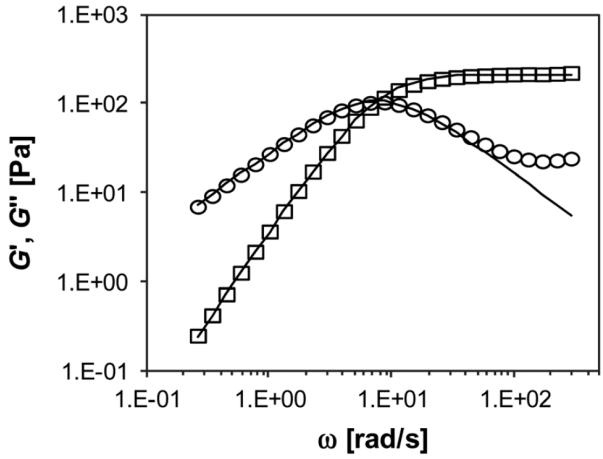

Fig. 1.6: *Frequency sweep data (G′ (○), and G′ (□)) fitted to the single-mode Maxwell model (continuous line) for an aqueous solution of 10% w/w sodium laureth sulfate (SLES) in 1M NaCl [87]*

From such a graph, one can directly evaluate the parameters of the model: the plateau modulus is the asymptotic value of the storage modulus, and the relaxation-time is the reciprocal of the crossover-frequency, i.e. the frequency at which the storage modulus exceeds the loss modulus, and the system loses its mainly-viscous behaviour, becoming predominantly elastic.

Furthermore, Fig.1.6 shows a deviation from model-prediction for high angular-frequency. This deviation can find two explanations, both predicted by Cates model [46]:

- the single-mode Maxwell model only describes the linear visco-elastic-response of the solution in the fast-reaction limit, i.e. when $\tau_{br} \ll \tau_{rep}$;

- either breathing or local Rouse-motion are becoming dominant.

Any deviation from the model can be emphasized by using the Cole-Cole plot, showing the storage modulus vs the loss modulus, which results in a perfect semi-circle when the single-mode Maxwell model applies.

Granek et al. [46] modelled the phenomena inducing a deviation from the semi-circle, predicting different responses (Fig1.7):

- when the assumption $\tau_{br} \ll \tau_{rep}$ is not met, G'' decreases with G' at high frequencies, but doesn't describe a perfect semi-circle;
- breathing and Rouse motions result in a turnup of G'' at very high angular-frequency.

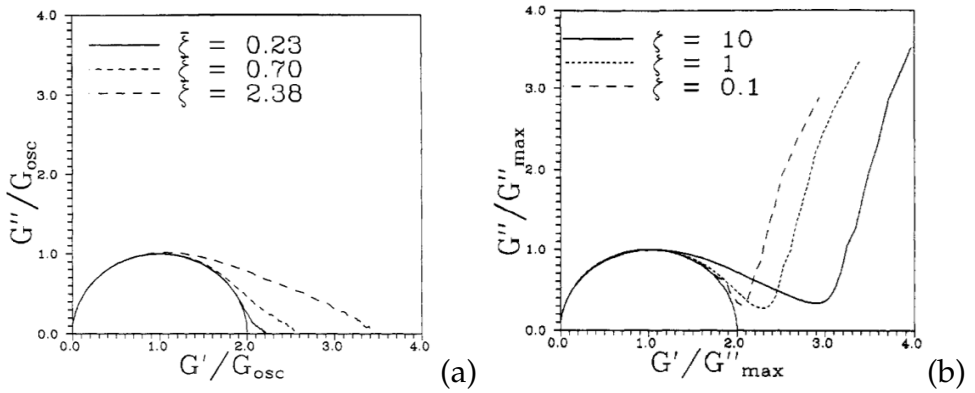

Fig. 1.7: *Deviation from single-mode Maxwell model for high values of $\zeta = \tau_{br}/\tau_{rep}$ (a) and when breathing and local Rouse-reactions are dominant (b) [64]*

Furthermore, Granek et al. [46] showed that the high-frequency minimum in the storage modulus is related to the average value of the contour lengths and to the entanglement length through

$$\frac{G''}{G_0} \sim \frac{l_e}{\bar{L}} \tag{1.10}$$

1.3.3 Scaling-laws

Cates et al. [22] suggest that, as for polymers, some properties of a wormlike micellar solution show scaling-laws with the volume-fraction of the surfactant, which they evaluated by using a mean-field approach:

- as already depicted, when $\tau_{br}/\tau_{rep} > 1$, the system behaves as a polymeric solution, and follows the scaling-laws of such a system, e.g. $G_0 \sim \varphi^{2.25}$, $\tau = \tau_{rep} \sim \varphi^3$, $\xi_M \sim \varphi^{-0.75}$, $\eta_0 = G_0\tau \sim$ $\sim \varphi^{5.25}$ [32];
- in the fast-reaction regime, the onset of scission and recombination reactions complicates the dynamic of the system, leaving some scaling-laws unchanged, such as those of the plateau modulus G_0 and of the mesh size ξ_M, but affecting others, e.g. $\tau = \sqrt{\tau_{rep}\tau_{br}} \sim \varphi^{1.25}$, and $\eta_0 = G_0\tau \sim \varphi^{3.5}$.

For years, numerous authors have reported deviations from these scaling-laws, which mainly find two explanations [17, 63, 67, 91]:

- their validity is restricted to some linear entangled micelles; in a branched network, they fail because of the presence of additional mechanisms of stress-relaxation, that are not taken into account in the Cates model, e.g. the ghostlike-crossing between micelles, and the sliding of branching-points on branched micelles (Fig.1.8);
- Berret [10] argued that, even for linear micelles, the distribution $c(L) \propto \exp(-L_c/\bar{L}_c)$ is suitable only for describing neutral or highly-screened micelles; as Cates predictions are based on a mean-field approach, any deviation from this distribution affects the scaling-laws.

The presence of sliding-mechanisms in branched network has been first reported by Lequeux [69], and it is been often invoked to explain

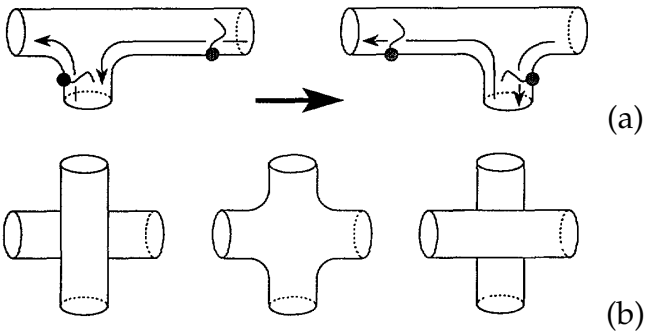

Fig. 1.8: *Additional mechanisms for stress-relaxation: sliding (a) and ghostlike-crossing (b) (adapted from [1])*

the dependence of η_0 from the salt content. In fact, it is widely reported [61, 92, 102, 118] that increasing salt concentration in micellar solution promotes the growth of the micelles, thereby considerably increasing the zero viscosity of the fluid. Despite this, a further increase of salt concentration induces a decrease of the viscosity [18, 48, 92], which has been related to the direct observation of branched micelles [94, 116, 121]. In fact, assuming that the sliding of branching-points is fast enough, in such a system the relaxation-time is faster than in a linear system, hence the viscosity decreases.

Furthermore, since the late '80s several authors [48, 92] have reported systems in which the viscosity shows a second maximum as a function of salt concentration; nowadays there is no universally-accepted theory to explain this phenomenon.

1.4 Non-linear rheology

When a wormlike micellar solution undergoes shear rates high enough to disturb its inner structure ($Wi = \dot{\gamma}\tau_R > 1$), it exhibits a non-linear rheological response. Thanks to the ability of the micelles to

break and reform, and thus to their additional mechanisms for stress-relaxation, the dynamics of these systems in non-linear regime show peculiar phenomena, some of which are not observed in polymers solutions and melts.

This complex flow-behaviour has been observed in a number of wormlike micellar systems, but is still unpredictable a priori [24, 112, 114], primarily because it is still not fully understood.

1.4.1 Shear banding

For solutions of wormlike micelles, Cates model predicts a non-monotonic flow-curve [21, 22, 46, 105] . As the shear rate is increased, the predicted flow-curve shows a maximum at ($\dot{\gamma}_M$, τ_M), where τ_M is the maximum stress that a micelle can hold before its tube breaks. At higher shear rates, a decreasing branch is predicted, up to a point ($\dot{\gamma}_m$, τ_m) at which the increasing contribution of the solvent causes an upturn in the flow-curve (Fig.1.9).

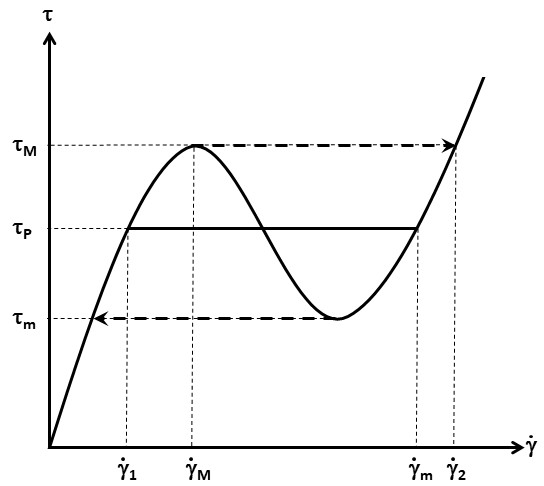

Fig. 1.9: *Flow-curve of a wormlike micellar solution*

The decreasing branch of this curve consists of non-stable points. Thus, in that range of shear rates, the system has to find a way to recover a steady-flow condition:

- when the shear stress is increased from low values, the shear rate continuously increases as well, up to $\dot{\gamma}_M$; a further increase in the shear stress results in a discontinuity of the shear rates, and the flow-curve jumps to the branch of high shear rate predicted by Cates ('top-jumping'); similarly, by decreasing the shear stress from high values, the flow-curve jumps from $(\dot{\gamma}_m,\ \tau_m)$ to the branch of low shear rate ('bottom-jumping');
- when the shear rate is increased, the shear stress increases as well, up to a value, $\dot{\gamma} = \dot{\gamma}_1$, after which a further increase of the shear rate doesn't result in an increase of the shear stress, which stays constant $(\tau = \tau_P)$; thus, the flow-curve shows a stress plateau which extends over several decades, up to a second critical value, $\dot{\gamma} = \dot{\gamma}_2$, after which the shear rate increases again.

The stress plateau in the flow-curve of wormlike micellar solution has been first reported by Rehage and Hoffmann in 1988 in a CPyCl/NaSal system [92], and, since then, has been observed in a broad number of systems [10, 23, 66, 68, 78, 79, 83, 118].

Although Cates model predicts non-stable points only when the shear rate is such that $\dot{\gamma}_M < \dot{\gamma} < \dot{\gamma}_m$, the range over which the system shows a stress plateau is wider, $\dot{\gamma}_1 < \dot{\gamma} < \dot{\gamma}_2$. In fact, Grand et al. [45] reported the possibility to overcome the plateau value of the stress, τ_P, by slowly increasing the shear rate over $\dot{\gamma}_1$, developing the metastable branch between $\dot{\gamma}_1$ and $\dot{\gamma}_M$.

According to the theory of Spenley [105], the stress plateau is related to a shear-banded flow: when the shear rate exceeds the first crit-

ical value, $\dot{\gamma}_1$, the fluid separates into two or more macroscopically-distinct bands, facing the same stress (τ_P), but supporting different local rates, whose average equals the fixed shear rate. In the simplest configuration, the solution splits into two phases, supporting $\dot{\gamma}_1$ and $\dot{\gamma}_2$; as the shear rate increases, the high-shear band becomes thicker and thicker, eventually covering the whole system; then, a further increase of the shear rate results in an increase of the shear stress. Although this configuration is the most common one, the onset of more bands has been both predicted [86, 118] and detected [35, 54].

Despite a great effort in detecting and analysing the shear banding transition in wormlike micellar solutions, there are still open questions.

One of the biggest challenges concerns the physical nature of this instability. In fact, it is generally believed that, in concentrated surfactant solutions, shear banding relates to an isotropic-to-nematic transition, the stress plateau relating to a growing nematic phase that coexists with an isotropic phase [5, 8, 41, 74, 98]. However, this phenomenology would not explain the onset of a shear banding transition in some dilute systems [115], which are too far from the nematic zone in the static-phase diagram [11, 33] (see Fig1.1). In this regime, in fact, shear banding has been ascribed to stress-fluctuations, which, above a critical shear rate, are usually related to the growth of birefringent [109], shear-induced structures [36, 92, 112], that may return to their initial morphology upon stopping the flow, with a relaxation time ranging over several order of magnitude [56]. On the other hand, several authors [18, 25] reported the formation of irreversible flow-induced structured phases (FISPs).

So far, several mechanisms have been proposed to take into account the behaviour of both concentrated and dilute solutions, as a

flow-induced shift in the isotropic-to-nematic phase boundary [96]; or the micelles disentanglement in the high-shear zones of the flow, leading to the coexistence of entangled and disentangled phases [57]; or a flow-induced demixing, leading to a concentration-gradient [47, 52, 72, 99].

Schmitt et al. [99], who first suggested the role of demixing in the strong-flow of wormlike micellar solutions, showed that concentration-gradients result in a very slight increase of the shear stress as a function of the shear rate, i.e. to a non-zero slope of the plateau (which, thus, is a pseudo-plateau). Both the onset of a stress pseudo-plateau [47, 52] and of concentration-gradients [15] have been later reported for several concentrated banded-systems. Despite this, several authors stress the difference between systems showing a stress pseudo-plateau and those showing a 'real' plateau, expecting the first ones to behave as pure-thinning fluids, and the second ones to show real banding [58, 82]. Thus, the question of whether the evidence of a stress pseudo-plateau could be related to shear banding or not is still open.

The picture becomes even more complex when the system consists of branched micelles. The presence of these aggregates creates an even more complex picture, as the possibility for a solution of branched wormlike micelles to show shear banding is still under investigation. In fact, although low-branched systems can show classical banding, in some highly-branched micellar solutions there is no evidence of shear banding or isotropic-to-nematic transition [13, 14]. This phenomenon can be ascribed to the increasing effect of the additional mechanisms of stress-relief induced by the branching points, which give a non-zero slope to the stress-plateau, thus inducing a new branch of stable points in the flow-curve [94]. Nevertheless, it has

been reported that an increase of the salt concentration, together with the development of branched structures, moves the system closer to a phase-boundary [100], beyond which the solution demixes into two phases. This phenomenon underlies the presence of shear-induced structures, that have been detected in branched micellar systems under flow by using SALS and SANS [60, 72, 100], and Liberatore et al. [72] suggest the presence of micron-sized shear-bands in these shear-induced structures.

Thus, even the question of whether an highly-branched wormlike micellar solution can exhibit shear banding or not is still open.

To summarize:

- both dilute and concentrated wormlike micellar systems can show shear banding, which results in a stress plateau in the flow-curve;
- in dilute systems, shear banding results in birefringent shear-induced structures, driven by stress-fluctuations;
- in concentrated systems, shear banding results in an isotropic-to-nematic transition, that can be driven by concentration-gradients;
- a stress pseudo-plateau is theoretically predicted in solutions undergoing concentration-gradients;
- the behaviour of solutions showing a stress pseudo-plateau is still under investigation, and the debate whether these can show shear banding or they are just thinning fluids is still open;
- micellar branching can result in a stress pseudo-plateau;
- low-branched micellar solutions can undergo shear banding;
- the question of whether a highly-branched micellar solution can exhibit shear banding is still open, as in some systems a high level of branching seems to be able to suppress shear banding, but in other there is evidence of shear-induced structuring.

Overview of the thesis

The lack of understanding on fundamental aspects of the flow-behaviour of wormlike micellar solutions justifies this work.

Here, we study a concentrated solution of highly-branched wormlike micelles that displays a stress pseudo-plateau, as detected in rheological measurements.

In the present work, microfluidics is exploited to investigate the complex flow-behaviour of such a system, characterized by remarkable flow-induced structuring-phenomena in the pseudo-plateau zone, related to flow-induced demixing, which doesn't result in an isotropic-to-nematic transition.

Structure of the thesis

The thesis is presented as follows:

- in the chapter 'Rheology', the rheology of the model system has been fully characterized, by matching a number of different techniques, as mechanical rheology and microrheology. Furthermore, the wall-slip behaviour of the solution has been characterized, and the slip velocity has been modelled;
- in the chapter 'Microfluidics', the flow-behaviour of the solution in a highly-confined geometry has been investigated. Here, by

coupling microfluidics with advanced optical microscopy and μPIV (particle image velocimetry) techniques, the correlation between the flow-induced structuring and the evolution of the velocity-profile has been analysed. Lastly, the results of these analysis have been related to the rheological properties of the system investigated;

- in the chapter 'Flow in pipes', the scale up of the results from microfluidics has been performed, by using pipes of several materials and sizes. Furthermore, by fixing the flow rate and measuring the pressure-drop through the pipes, additional rheological data have been extracted;
- in the chapter 'CFD analysis', the flow curve of the wormlike micellar solution and the developed model of wall-slip, have been used to perform a CFD analysis, in the same conditions of the microfluidic experiments; than the possibility to predict experimental results by assuming a pure-thinning behaviour of the model system has been investigated;
- in the chapter 'Concentration-gradients', microfluidics is coupled with rotational rheometry, electrical-conductivity and dry-mass measurements, in order to investigate the occurrence of flow-induced concentration-gradients within the solution.

Chapter 2

Rheology

2.1 Abstract

Production and processing of wormlike micellar solutions, as well as their industrial and daily applications, involve a broad variety of operations, in some of which the system experiences high shear rates. Modelling and predicting the flow behavior of a wormlike micellar solution in such processes requires rheological data covering a wide range of shear rates, up to around 100 000s^{-1}. These values are well beyond the instrumental limits of rotational rheometry, that can hardly reach shear rates as high as 1 000s^{-1}. Other rheological techniques are better suited to investigate high shear rate ranges, but, on the other hand, they provide a worse performance at low shear rates.

In this scenario, matching several measurement-techniques can play a key-role in filling the gap between classical rotational rheometry and high shear rate data. In fact, by coupling techniques with different characteristic shear rates, one can cover the whole operating-range of the most common industrial operation-units involved in processing of wormlike micellar solutions.

Here, we measure the flow-curve of a widely-used wormlike micellar solution in an extended range of shear rates and frequencies, by using classical mechanical rheology tests, together with microrheology techniques.

2.2 Model system

The model system consists in a CTAB ($C_{19}H_{42}BrN$, PM=364.45, purity $\geq$ 99% - Sigma Aldrich) and NaSal (HOC_6H_4COONa, PM=160.10, purity $\geq$ 99.5% - Sigma Aldrich) aqueous solution. CTAB has been added to distilled water in a concentration of 0.05M, and stirred for a few minutes. After the addition of NaSal in a 0.045M concentration, the solution has been mixed for about two hours, and then left to stand at least one day.

According to [48], the concentration of NaSal is high enough to overcome the first maximum in the curve of salt concentration vs zero-shear viscosity. Thus, the system is expected to be branched.

2.3 Rotational rheometry

2.3.1 Frequency sweep test

In order to verify the Maxwellian behaviour of the model system, SAOS measurements have been run. Thus, a frequency sweep test has been run at 20°C with 2% strain in a controlled-stress rheometer (Anton Paar MCR-302), equipped with a standard-steel cone geometry (D=40mm, cone angle=1°). Three sweep-cycles have been run, to ensure the steady-state conditions.

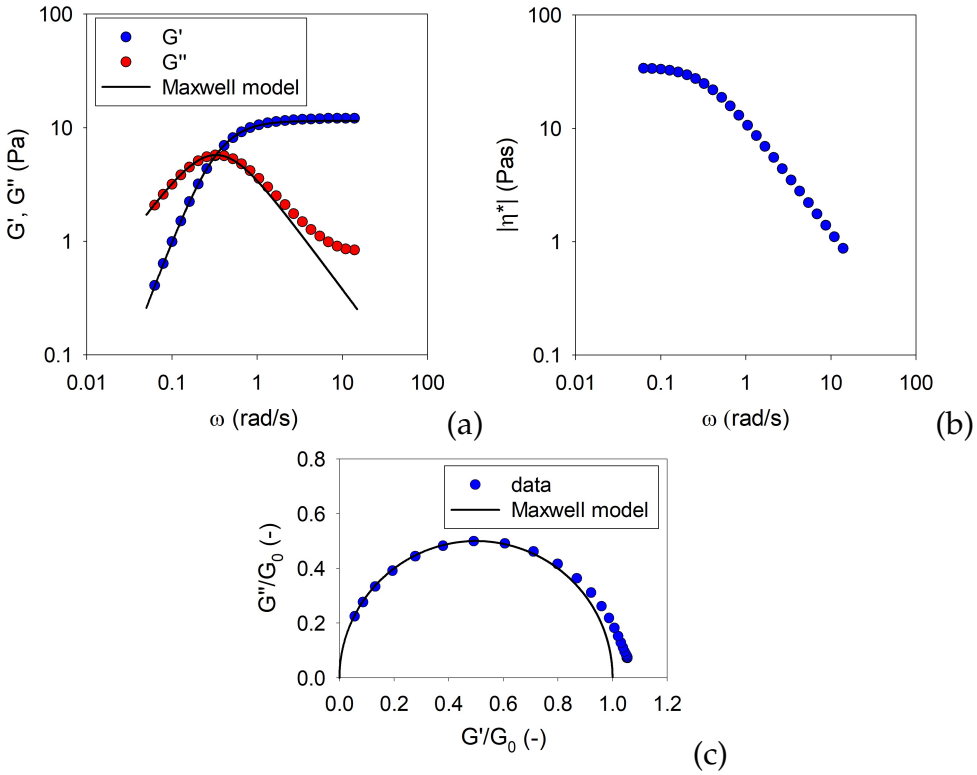

Fig. 2.1: *Frequency sweep test results: (a) measured storage (●) and loss (●) modulus, and Maxwell model prediction (filled line); (b) complex viscosity; (c) Cole-Cole plot of the data (●), and Maxwell model prediction (filled line)*

Fig.2.1 shows the storage and loss moduli and the complex viscosity, together with the Cole-Cole plot of the solution, proving the good agreement of the data with the Maxwell model up to high frequencies.

As reported in Sec.1.3.2, using the storage and loss moduli, it is possible to evaluate $G_0 = 11.48$Pa, and $\tau = 3.04$s.

2.3.2 Shear rate sweep and creep tests

The steady-state viscosity of the model system has been measured at 20°C in a controlled-stress rheometer (AR-G2, TA Instruments),

equipped with a standard-steel cone geometry (D=40mm, cone angle=2°). Experiments have been performed in both shear rate and shear stress mode, to cover a range of shear rates as broad as possible.

For each fixed shear rate or stress, the response of the system has been measured for a long time. Thus, in order to prevent the sample evaporation, a solvent trap has been used, and the sample has been replaced before each measurement - i.e. each sample has been used to run one experiment with one constant value of shear rate or stress. Lastly, before each measurement, the sample has been conditioned for 100s at the desired temperature.

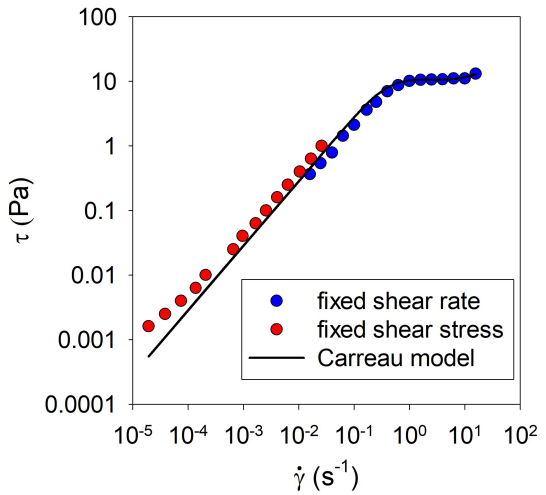

Fig. 2.2: *Flow-curve: shear rate sweep (●), creep test (●) and Carreau model fit (filled line)*

The steady flow-curve so-obtained is shown in Fig.2.2, where the data are fitted to a Carreau model. This results are in good agreement with rheology reported in literacture [89].

Within the range $1\text{s}^{-1} \leq \dot{\gamma} \leq 10\text{s}^{-1}$, the slope of the fitting curve - i.e. $d\tau/d\dot{\gamma}$ - never equals zero, with an average value of 0.147. Although a 'real' plateau (with zero slope) hasn't been detected, the tran-

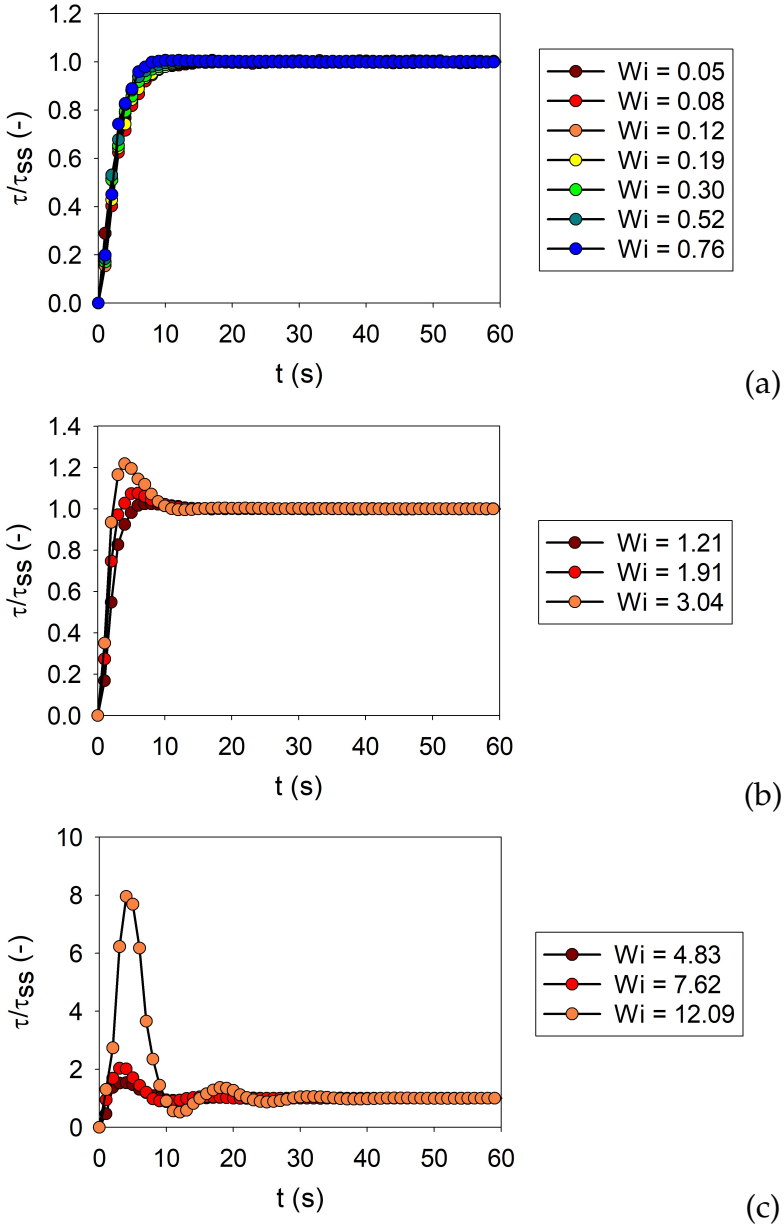

Fig. 2.3: *Transient rheological response under constant shear rate: (a) $Wi << 1$, (b) $Wi \sim 1$, (c) $Wi >> 1$; data are normalized with respect to the steady-state stress, τ_{ss}*

sient rheological response at constant shear rate (Fig.2.3) shows how increasing the shear rate affects the dynamic of the system:

- when $Wi \ll 1$, the system shows a fast and monotone response, reaching its steady-state in a time on the same order of magnitude than the relaxation-time;
- when $Wi \sim 1$, the response is still fast, but non monotone, and the shear stress shows an overshoot before it reaches its steady-state;
- when $Wi \gg 1$, the system reaches its steady-state after a very long time, through a under-damped response.

Such a behaviour indicates that, at low values of Wi, the dynamic of the system is governed by one process (or several processes with the same characteristic-times); then, when Wi increases, at least two processes with very different characteristic-times coexist. It is well-known that wormlike micelles solutions under strong-flow conditions show very long transients [7, 9, 10, 45, 56], eventually related to fluctuating responses, but, to the best of our knowledge, only a few papers reported such a behaviour [7, 103]. Berret [7] related the response at high values of Wi to an isotropic-to-nematic transition which occurs on a time-scale much higher than τ_R.

Lastly, Fig.2.4 shows the dynamic response during creep. The dumped fluctuations at flow-startup are related to a combined effect of the instrument inertia and the solution elasticity [2].

The curves of the compliance at different value of stress overlap one each other.

In fact, as reported in Fig.2.5, the system shows non-zero first normal-stress difference only when $Wi > 1$, i.e. when $\dot{\gamma} > 0.33s^{-1}$; this indicates that all the experiments in shear stress mode lie in the linear viscoelastic regime, this explaining the independence of the compli-

ance from the stress.

2.3.3 Plate-plate geometry

In anticipation of studying the possible wall-slip of the flowing solution, which requires the analysis of flow-curves at several gaps, the procedure to use a plate-plate geometry is presented.

As it is well known, in a parallel-plate geometry the flow-field is not homogeneous, i.e. the shear rate is not constant along the radius. The rheometer reports the shear rate at the rim of the plate, and an average shear stress, named 'apparent shear stress', τ_a. Assuming no-slip conditions and neglecting the inertial forces, the shear stress at the rim of the plate, τ, can be evaluated through [75]:

$$\tau = \frac{\tau_a}{4}\left(3 + \frac{d\,log(M)}{d\,log(\dot{\gamma})}\right) \tag{2.1}$$

where M is the torque exerted on the plate.

From this point forward, this correction, together with the gap-error correction presented below, has been applied to all data generated using parallel plates geometry, and the corrected values so-obtained are referred to as $\dot{\gamma}$ and η. In order to get an analytical form of $d\,log(M)/d\,log(\dot{\gamma})$, before applying Eq.2.1, data have been fitted using a Carreau model.

2.3.3.1 Gap-error correction

It's been widely reported [29, 31] that the use of a parallel-plates geometry induces error measurements. In fact, the measured viscosity of both newtonian and non-newtonian fluids decreases as the gap between the plates decreases, approaching the nominal viscosity of the fluid when the gap is higher than 200-300 μm.

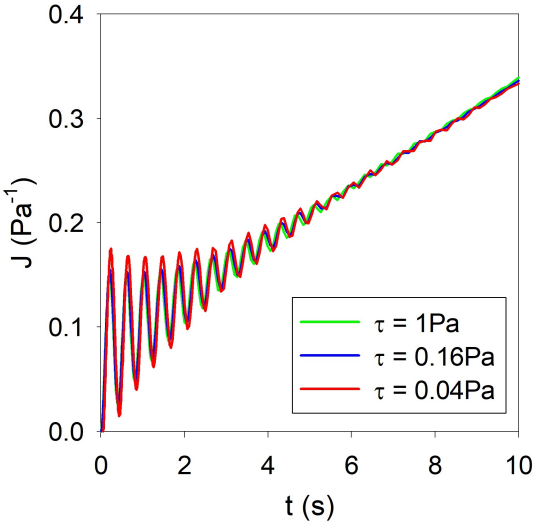

Fig. 2.4: *Transient rheological response under constant shear stress*

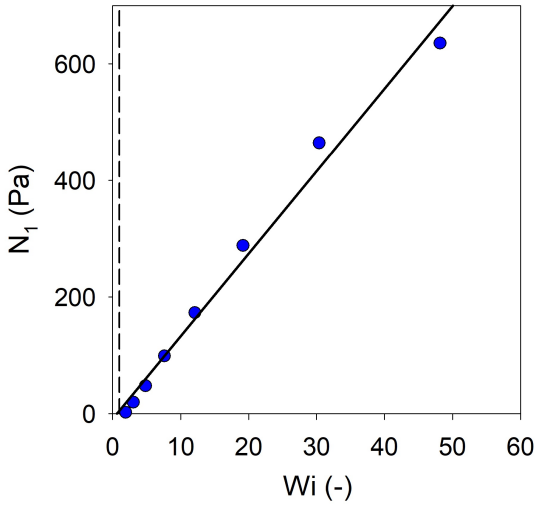

Fig. 2.5: *First normal stresses difference; the dashed line is a reference to* $Wi = 1$

This error has been reported to arise from many sources, such as lack of parallelism induced from a misalignment of the plate (Fig.2.6), non-concentricity and non-flatness of the plate, wall-slip effects, or the squeeze of the air during the zeroing-procedure [29, 30, 53].

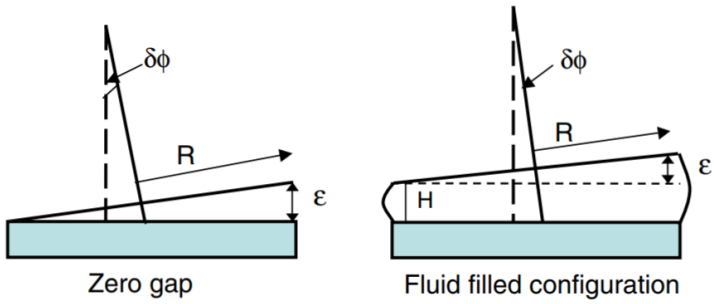

Fig. 2.6: *Effect of the misalignment of the plate during gap-zeroing (left) and after sample-loading (right) (adapted from [88])*

In 1985, Connelly and Greener [29] proposed a procedure to correct the measured viscosity, suggesting to take into account every source of error by introducing a term ε, named 'gap-error'. This term has to be added to the nominal gap, δ, to evaluate the effective one. Thus, the shear rate evaluated from the rheometer at the rim and the real one are, respectively

$$\dot{\gamma}_M = \frac{\Omega R}{\delta}, \;\; \dot{\gamma} = \frac{\Omega R}{\delta + \varepsilon}; \tag{2.2}$$

and the corresponding viscosities are

$$\eta_M = \tau \frac{\delta}{\Omega R}, \;\; \eta = \tau \frac{\delta + \varepsilon}{\Omega R}; \tag{2.3}$$

hence,

$$\dot{\gamma}_M = \dot{\gamma} \frac{\delta + \varepsilon}{\delta}, \;\; \eta_M = \eta \frac{\delta}{\delta + \varepsilon} \tag{2.4}$$

Once the viscosity η_M is measured as a function of the fixed gap, δ, data can be fitted by using Eq.2.4, thus extracting the real viscosity, η, and the gap-error, ε.

The most commonly-used approach to this correction consists in linearizing the Eq.2.4:

$$\frac{\delta}{\eta_M} = \frac{\delta}{\eta} + \frac{\varepsilon}{\eta} \tag{2.5}$$

Therefore, the plot of δ/η_M vs δ represents a straight line, whose slope is $1/\eta$, and whose intercept with the y-axis is ε/η.

On the other hand, once the plate is attached to the rheometer, opening or closing the gap doesn't have any impact on the gap-error. Thus, once a fluid has been tested to apply the Eq.2.5, one can repeat the procedure with another fluid (withour removing the plate), and has to get the same gap-error.

In order two study the effect of the linearization on the Eq.2.4, several fluids have been tested in shear rate mode at 20°C, using a controlled-stress rheometer (AR-G2, TA Instruments), equipped with a standard-steel plate (D=40mm).

After zeroing, the used procedure is:

1. a sample is loaded, a high value of the gap is fixed, and the sample is trimmed;
2. the sample is conditioned at chosen temperature for 1000s;
3. viscosity is measured for 60s at $\dot{\gamma} = 50\text{s}^{-1}$;
4. the gap is lowered to a new value, the sample is trimmed, and the viscosity is measured again as (3);
5. point (4) is replicated several times;
6. the gap is opened, and the sample is gently removed,, without detaching the plate.

The procedure has been replicated with four samples:

- oil C200 Flow Cup Viscosity Standard (Paragon Scientific Ltd., certified nominal $\eta(20°C) = 559.2cP$);
- pure glycerol (P&G, nominal $\eta(20°C) = 1412cP$ [101]);
- commercial liquid honey (Meli, unknown nominal viscosity);

- oil - see previous one.

Then, The linear form of the correction has been applied, and both the nominal viscosity and the gap-error have been evaluated (Tab.2.1).

Tab. 2.1: *Gap-error correction using a linear fit of the measured viscosity*

sample	**nominal viscosity η_N, cP**	**evaluated real viscosity η, cP**	**evaluated gap-error ε, μm**
Oil	559.2	572.4	72.51
Glycerol	1412	1382.3	22.72
Honey	unknown	10788.2	0.27
Oil	559.2	588.0	80.84

Thus, linearizing the equation Eq.2.4 results in a non-constant gap-error, which is inconsistent with the used procedure. This might be related to the η_M term in the denominator of Eq.2.5. In fact, when the tested fluid has been changed, the evaluated gap-error changed as well, while it is almost constant when testing the same fluid twice.

Nevertheless, the deviation of the evaluated viscosity from the nominal one is small ($\sim$ 2%), thus showing that the linear form of Eq.2.4 can be applied to evaluate the real viscosity, even though is not suitable for evaluating the gap-error, which shows a standard deviation of 38.9μm.

The direct use of the Eq.2.4 gives a more reliable gap-error. Here, the non-linear tool of the JMP statistical software has been used to directly fit η_M as a function of δ (Fig2.7).

The results of this fit are reported in Tab.2.2, and show a great consistency of all the evaluated gap-errors, with a standard deviation of 6.6μm. This procedure doesn't affect the 'quality' of the measured

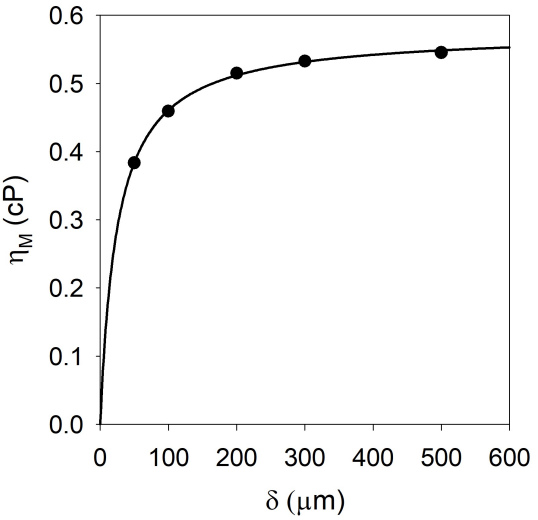

Fig. 2.7: *Measured viscosity as a function of the gap (●), and non-linear fit of the data (filled line)*

viscosity (deviation from nominal viscosity $\sim 3.6\%$).

Tab. 2.2: *Gap-error correction using a non-linear fit of the measured viscosity*

sample	**nominal viscosity η_N, cP**	**evaluated real viscosity η, cP**	**evaluated gap-error ε, μm**
Oil	559.2	575.6	24.97
Glycerol	1412	1365.6	39.66
Honey	unknown	10683.3	29.11
Oil	559.2	584.6	26.66

When the tested fluid shows wall-slip effect, the gap-error and the slip velocity can't be evaluated separately, as they affect the same parameters, and both become more relevant as the gap between the

plates is lowered. As the possible presence of wall-slip in the model system has to be considered and studied, from this point forward the gap-error is measured before any experiment in parallel plates, by testing a newtonian fluid (glycerol). Then, this fluid is gently removed without detaching the plate, and the designed test is performed.

Lastly, measured data are corrected using the gap-error previously evaluated. This step won't be reported every time.

2.3.4 Hysteresis and evaporation

In order to study both the presence of evaporation and/or any hysteresis-effects, several tests have been carried at 20°C using a controlled-stress rheometer (AR-G2, TA Instruments), equipped with a standard-steel plate (D=40mm), fixing δ=500μm. Three flow-curves have been measured:

- for the first one, the procedure described in Sec.2.3.2 has been used; thus, each sample has been used to run one experiment with one constant value of shear rate;
- for the second one, one sample has been used to measure the whole flow-curve, increasing the shear rate;
- for the third one, one sample has been used to measure the whole flow-curve, decreasing the shear rate.

All the measurements have been done without removing the plate from the rheometer and, before the use, every sample has been conditioned for 100s at chosen temperature.

Results are shown in Fig.2.8. All the data perfectly overlap, thus showing that, on the time required to measure the whole flow-curve, evaporation is not relevant; furthermore, there is no hysteresis. Lastly, data are consistent with measurements obtained with a cone geometry (Sec.2.3.2), thus validating the corrections presented in Sec.2.3.3.

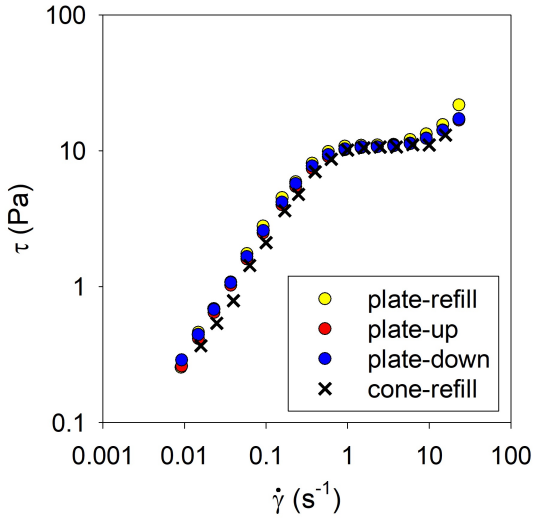

Fig. 2.8: *Flow-curve: refilling the sample for each shear rate, in a plate-plate geometry (●) and in a cone-plate geometry (✖); without refilling the sample, in a plate-plate geometry, increasing (●) and decreasing (●) the shear rate*

2.3.5 Slip velocity

The possible slip-velocity of the fluid has been studied by using two different rheometers. In fact, in order to evaluate any wall-slip on standard-steel, experiment made in Sec.2.3.4 (refer to the first flow-curve) have been replicated with the same rheometer and geometry, by changing the gap.

Then, a similar study has be done in a controlled-stress rheometer (HAAKE MARS III, Thermo Scientific), equipped with a standard-steel plate (D=35mm) and a Rheoscope module, on which different base plates can be fixed. Several measurements have been done, fixing a standard-steel base-plate or a transparent-glass base-plate on the Rheoscope module, and lowering the gap.

Before every measurement, the sample has been conditioned for

100s, in order to reach T = 20°C. The results of these experiments are reported in Fig.2.9.

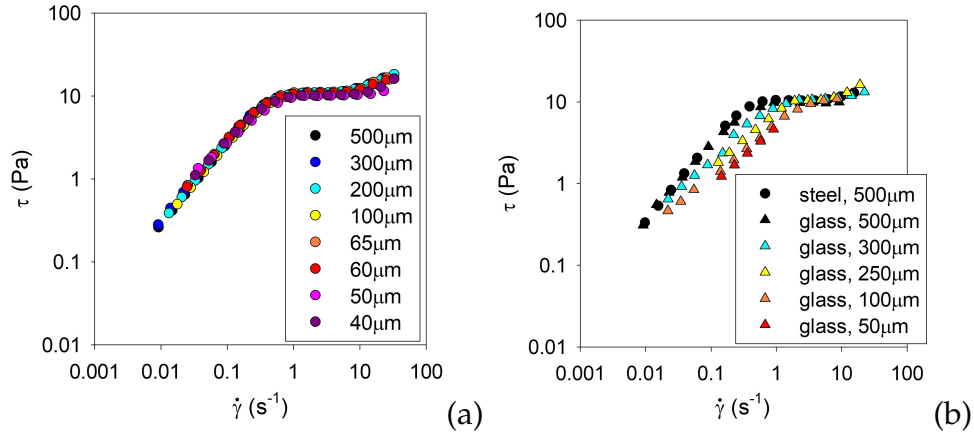

Fig. 2.9: *Flow-curve as a function of the gap, measured (a) in an AR-G2 rheometer using steel plates, and (b) in an HAAKE MARS III rheometer, using two steel plates, or one glass and one steel plates*

All the measurements made in steel plates collapse on the same flow-curve.

On the other hand, the flow-curves measured using a glass plate show an increasing right-shift as the gap between the plates is lowered. This behaviour is indicative of the presence of wall-slip. In fact, the shear rate reported from the rheometer is

$$\dot{\gamma} = \frac{\Omega R}{\delta} = \frac{v}{\delta} \tag{2.6}$$

where Ω is the angular velocity of the rheometer, v is the velocity of the plate at the rim, R is the radius of the plate, and δ is the gap between the plates.

Due to the presence of wall-slip, for fixed shear stress, the actual shear rate the sample faces is (Fig.2.10)

$$\dot{\gamma}_{real} = \frac{\Omega R - v_{slip}}{\delta} = \frac{v - v_{slip}}{\delta} \tag{2.7}$$

which is smaller than the measured one.

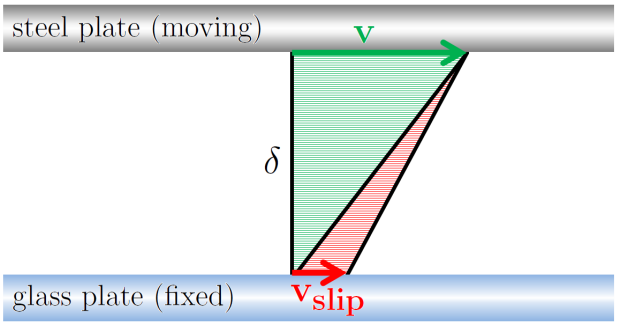

Fig. 2.10: *The onset of wall-slip phenomena reduces the actual shear rate*

Thus, when wall-slip occurs, the rheometer reports a shear rate higher than the real one. This effect causes the right-shift of the flow-curve. When $\delta = 500\mu m$, the flow-curve collapses to the one measured by using two steel plates, this suggesting that any slip-effect has became negligible. Furthermore, it is worth noting that, when a glass plate is used, lowering the gap doesn't induce a pure right-shift of

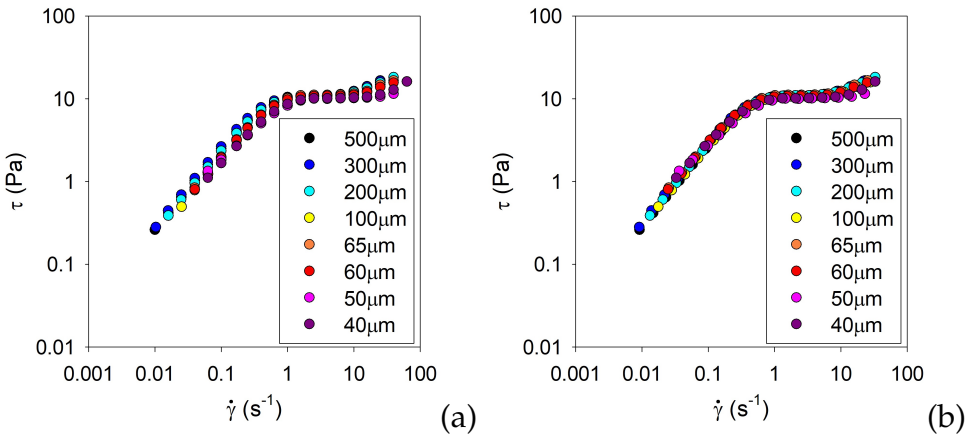

Fig. 2.11: *Flow-curve as a function of the gap, measured in an AR-G2 rheometer using steel plates, (a) before and (b) after gap-error correction*

the pseudo-plateau, but shortens it. Thus, whatever is the physical-phenomenology at the base of such a pseudo-plateau, it is affected by the occurrence of wall-slip phenomena.

Lastly, Fig.2.11 shows the importance of the gap-error correction. In fact, uncorrected measurements show a fictitious-shift in the same direction of that induced from wall-slip phenomena. Thus, when gap-error correction in not applied, wall-slip can be overestimated or, as from Fig.2.11(a), a non-existent slip-velocity could be evaluated.

2.3.5.1 Modelling

From Eq.2.6 and Eq.2.7, for fixed stress and gap, the slip velocity is

$$v_{slip} = \delta(\dot{\gamma}\big|_{\tau,\delta} - \dot{\gamma}_{real}\big|_{\tau,\delta}) \tag{2.8}$$

The rheometer can't have access to the real value of shear rate, but, when $\delta \to \infty$, the measured shear rate equals the real one

$$v_{slip} = \delta(\dot{\gamma}\big|_{\tau,\delta} - \dot{\gamma}\big|_{\tau,\delta\to\infty}) \tag{2.9}$$

As already depicted, wall-slip becomes negligible when $\delta = 500\mu m$ (Fig.2.9), and $\dot{\gamma}\big|_{\tau,\delta\to\infty} = \dot{\gamma}\big|_{\tau,\delta=500\mu m}$. Thus, Eq.2.9 becomes

$$v_{slip} = \delta(\dot{\gamma}\big|_{\tau,\delta} - \dot{\gamma}\big|_{\tau,\delta=500\mu m}) \tag{2.10}$$

Both $\dot{\gamma}\big|_{\tau,\delta}$ and $\dot{\gamma}\big|_{\tau,\delta=500\mu m}$ are known, but, in order to apply the Eq.2.10, data at the same shear stress are required. Thus, data has been fitted, focusing on τ <11Pa. As the shear stress is a function of both the shear rate and the gap, the aim here is to make a bivariate-fit of the data.

First, in the range of interest, each flow-curve has been modelled separately as $\tau = k\dot{\gamma}^n$. Tab.2.3 shows the values of the parameters of such a fit, when $\tau[=]$Pa and $\dot{\gamma}[=]s^{-1}$.

Tab. 2.3: *Parameters of a power-law fit of the flow-curves*

Gap, μm	k	n
500	15.826	0.719
300	10.872	0.710
250	8.279	0.753
100	6.101	0.713
50	5.263	0.721

As the exponent n is constant, the dependence of the shear stress on the gap can be described as a dependence of the only pre-factor k on the gap, i.e. $\tau = k(\delta)\dot{\gamma}^n$. Furthermore, Fig.2.12 suggests that $k(\delta) = a + b\delta$.

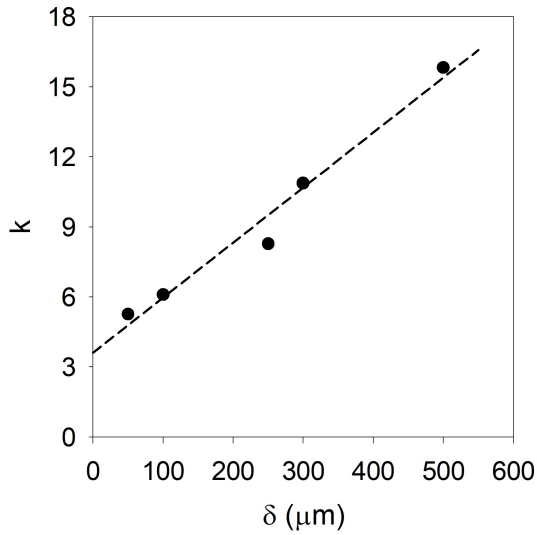

Fig. 2.12: *Pre-factor k as a function of the gap δ*

In conclusion, the model used to describe the flow-curve is

$$\tau = (a + b\delta)\dot{\gamma}^n \tag{2.11}$$

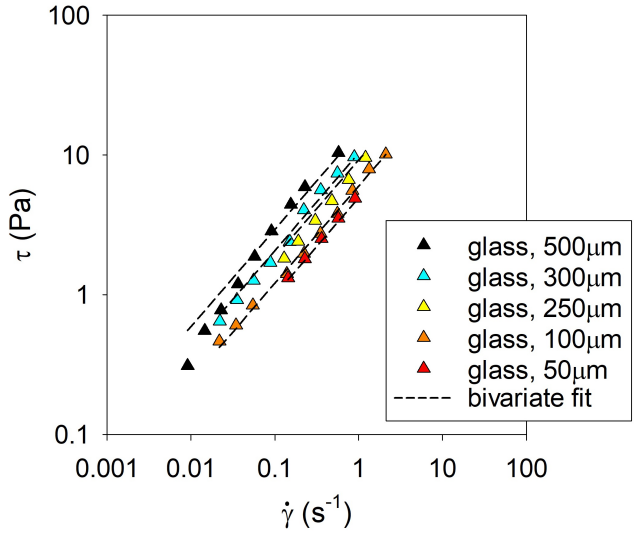

Fig. 2.13: *Bivariate-fit of the flow-curves at different gaps, in the range of interest*

As shown in Fig.2.13, such a model properly describes the data. It is now possible to use the Eq.2.11, which has been applied to every

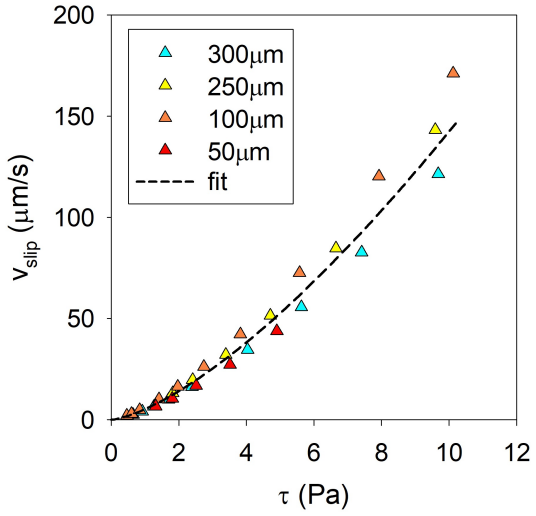

Fig. 2.14: *Slip velocity as a function of shear stress and gap*

value of the gap (Fig.2.13).

As all the obtained values of the slip velocity collapse on the same curve, there is no evidence of an effect of the gap on the wall-slip. Thus, the slip-velocity is a function of the only shear stress, and is well described by

$$v_{slip} = v_{slip,0}\tau^m \tag{2.12}$$

with $v_{slip,0} = 5.2$ and $m = 1.44$ when $v_{slip}[=]\mu m$ and $\tau[=]Pa$ (Fig.2.14).

2.4 Microrheometry

The measuring-range of a conventional rheometer is limited by practical problems, such as shear-induced fracturing or sample-ejection. The use of emerging measurement-techniques, such as microrheometry, helps to overcome these limits and to reach shear rates and frequencies much higher than those provided by a rotational rheometer [27, 28, 44, 88].

Microrheometry-techniques can be sorted in [28]:

- interfacial-rheology techniques, aiming to characterize the static and dynamic-properties of fluids-interfaces;
- bulk-rheology techniques, that extract rheological-properties of the fluid by studying the motion of probe-particles within it:
    - the active techniques require the application of a local stress to the probe-particles, and measure the so-induced displacement;
    - the passive ones analyse the molecular-motions of the particles in the resting sample due to thermal or Brownian fluctuations.

In addition to these techniques, microfluidic devices can be exploited to extract rheological information on the flowing system, by

studying its bulk-response (rheometry-on-a-chip) or its local behaviour (Sec.3.4).

Here, the measurement-range of a rotational rheometer has been extended by using microrhometry commercial-devices:

- the pure-shear and the pure-extensional flow have been investigated in a rheometer-on-a-chip (Sec.2.4.1);
- the scattering behaviour of probes embedded within the sample has been investigated using diffusing wave spectroscopy (Sec.2.4.2).

2.4.1 Rheometer-on-a-chip

It is possible to extract rheological information of a system flowing through a well-described geometry, by monitoring the pressure-drop as a function of the flow-rate [75]; for instance, when a straight-pipe is used, one can evaluate the shear rate and the shear stress.

When the flow-geometry is a microfluidic chip, the device that can perform such an analysis is referred to as 'rheometer-on-a-chip', and virtually shows no limits to the flow-rate one can provide.

Here, the VROC (RheoSense) has been used. This commercial rheometer-on-a-chip exploits an array of sensors to measure the pressure-drop the fluid faces in a microchannel while flowing with a specific flow-rate, controlled by a syringe-pump.

Based on the chosen flow-geometry, the VROC can be used to study the response of the model system under several types of flow: a rectangular slit provides a pure-shear flow, while a hyperbolic contraction as designed in [83] provides a pure-extensional one (Fig2.15).

As explained in the following sections, measurements from the VROC may require several corrections, in order to take into account the possible non-newtonian behaviour of the flowing system, and

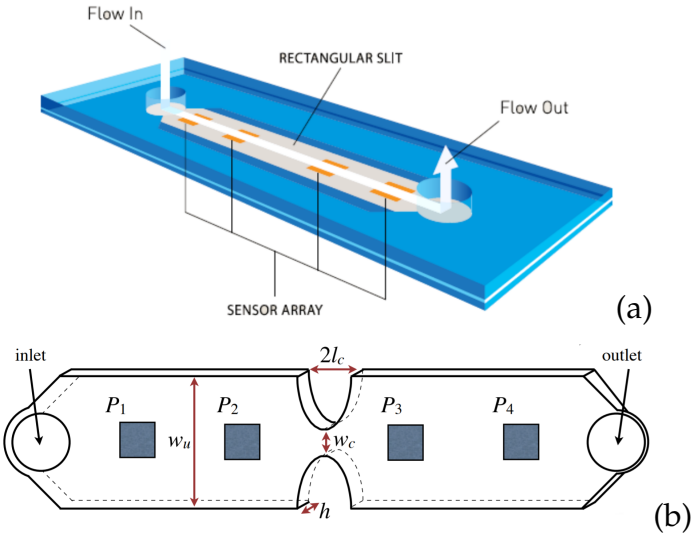

Fig. 2.15: *Flow geometries used in the VROC: (a) rectangular slit [123], and (b) hyperbolic contraction (adapted from [83])*

other effects induced by the design of the flow-geometry. The VROC is not always able to perform these corrections, thus data provided from the instrument may require further post-processing.

2.4.1.1 Shear flow

When studying the simple-shear flow in the straight channel, the VROC takes into account the non-newtonian behaviour of the model system, by extracting the shear rate from the fixed flow-rate and the shear stress from the measured pressure-drop, and then applying the Weissenberg-Rabinowitsch-Mooney (W.R.M.) correction [123]:

$$\tau = \frac{\Delta P}{l}\frac{wh}{2w+2h}, \quad \dot{\gamma}_a = \frac{6Q}{wh^2}, \quad \dot{\gamma} = \frac{\dot{\gamma}_a}{3}\left(2 + \frac{d\,log(\dot{\gamma}_a)}{d\,log(\tau)}\right) \tag{2.13}$$

where Q is the fixed flow-rate, w and h are the width and the height of the channel, respectively, and $\Delta P/l$ is the measured pressure-drop per unit of length.

Fig.2.16 shows the obtained data at T = 20°C, together with the measurements from rotational rheology.

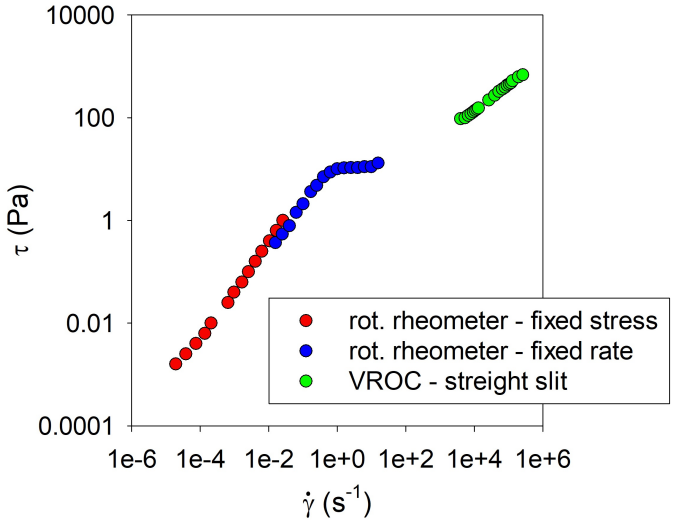

Fig. 2.16: *Flow-curve from VROC (●) and rotational rheometer (●,●)*

The upper limit of the VROC is related to the maximum pressure the system can sustain, which is high enough to reach shear rates as high as $\sim$260 000s^{-1}. On the other hand, the minimum shear rate one can operate is related to the sensitivity of the pressure-sensors, which isn't high enough to allow measurements from microrheometry to 'join' those from rotational rheology, this inducing a 'hole' in the flow-curve for 15s$^{-1} \lesssim \dot{\gamma} \lesssim$4 000s^{-1}.

2.4.1.2 Extensional flow

The flow-geometry used to study the pure-extensional flow is characterized by a hyperbolic contraction (Fig.2.15) as described in [83]. This, for given flow-rate, provides a constant extensional rate $\dot{\varepsilon}$ along the centerline.

In this case, data provided by the VROC have to be postprocessed to get corrected measurements. In fact, in an ideal case,

$$\dot{\varepsilon} = \frac{Q}{l_c h}\left(\frac{1}{w_c} - \frac{1}{w_u}\right), \quad \eta_e = \frac{\Delta P_e}{\varepsilon_H \dot{\varepsilon}} \tag{2.14}$$

where Q is the flow-rate, $\varepsilon_H = ln(w_u/w_c)$ is the Hencky strain at the throat of the contraction, ΔP_e is the pressure-drop over the contraction due to extensional flow, and h, w_u, l and w_c are the height and the width of the channel, and the length and the width of the contraction, respectively.

In reality, two sources of error have to be considered:

- even in the contraction throat, the flow is characterized by a shear flow contribution, due to fluid shearing near the walls. Thus, the pressure-drop over the contraction due to extensional flow is $\Delta P_e = \Delta P_c - \Delta P_s$, where ΔP_c is the overall pressure-drop, and ΔP_s is that due to shear flow;
- pressure-sensors aren't located exactly at the inlet and at the outlet of the contraction, thus $\Delta P_c \neq P_2 - P_3$.

The VROC extracts ΔP_c from $P_2 - P_3$ by using

$$\Delta P_c = (P_2 - P_3)\left[1 - \frac{1}{2}\left(\frac{P_1 - P_4}{P_2 - P_3} - 1\right)\frac{L_{23} - 2l_c}{L}\right] \tag{2.15}$$

where $2l_c$ and L are the length of the contraction and that of the whole microchannel, respectively.

Thus, the only required postprocessing concerns the evaluation of ΔP_s.

The correction protocol reported in [124] suggests to use

$$\Delta P_s = \frac{2^{n+2}}{n+1}\left(\frac{2n+1}{n}\right)^n \left(\frac{l_c}{h}\right)^{n+1} \left\{\left(\frac{w_u}{wu - w_c}\right)^{n+1} + \left(\frac{w_c}{w_u - w_c}\right)^{n+1}\right\} \tag{2.16}$$

where, assuming that the shear viscosity is well-described by a power-law of the shear rate, m and n are the power-law parameters. In this flow-geometry, the VROC can't establish the value of these parameters, which have to be separately evaluated by using a straight slit, and then applied through Eq.2.16 to correct the pressure-drop.

Fig.2.17 shows the corrected data at T = 20°C obtained in both flow geometries, together with the fit of measurements obtained using a straight slit (Sec.2.4.1.1).

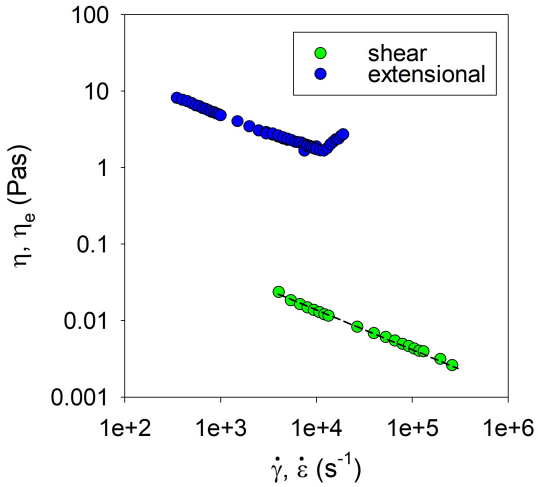

Fig. 2.17: *Shear (●) and extensional (●) viscosity, and fit of shear viscosity (dashed line)*

As before, operating-range is defined by the sensitivity of the sensors and by the maximum pressure the slit can face.

When $\dot{\varepsilon} \gtrsim 10^4 s^{-1}$, data show an upturn in extensional viscosity. Although extensional thickening has been reported in several solutions of wormlike micelles [65, 90, 113] and related to flow-induced chain-stretching, the abrupt upturn of the viscosity can be indicative of the onset of secondary-flows, as the upstream vortices reported in [83].

2.4.2 DWS

In a diffusing wave spectroscopy (DWS) experiment, the scattering-behaviour of a turbid sample hit by a laser-beam can be used to evaluate the time-dependent mean-square-displacement (MSD) of the sample, $\langle \Delta r^2(\tau) \rangle$.

When a clear sample has to be analysed, it can be seeded with microparticles, and the evaluated $\langle \Delta r^2(\tau) \rangle$ represents the MSD of such particles. In this case, the choice of the microparticles is crucial, as they have to behave as probes of the overall mechanical characteristics of the system. Thus, their dimension have to be much larger than any characteristic length of the system, as smaller particles can move within the fluid-matrix; then, their scattering-contributions have to be larger than that of the system, and there has to be no chemical-interaction between the particles and the system. When such particles can be considered as a tracer, the evaluated MSD can be considered as a measure of the overall mechanical-properties of the system.

Once the laser has hit the sample, the temporal fluctuations of the intensity of the scattered light in one point ('speckle'), $I(t)$, can be used to evaluate the intensity correlation-function, $g(\tau) - 1$, where

$$g(\tau) = \frac{\langle I(t) I(t+\tau) \rangle_t}{\langle I(t)^2 \rangle_t} \tag{2.17}$$

The intensity correlation-function can in turn be used to evaluate the MSD through

$$g(\tau) - 1 = \left[\int_0^\infty P(s) \exp\left(-\frac{1}{3} k^2 \langle \Delta r^2(\tau) \rangle \frac{s}{l^*} \right) ds \right]^2 \tag{2.18}$$

where $P(s)$ is the distribution-function of photon random-walking trajectories of length s in the sample, which depends on the geometry in which the sample is contained; $k = 2 * \pi n / \lambda$ is the wavenumber of

the light of wavelength λ in a medium of refractive index n, and l^* is the transport mean free-path, which represents the average length of a single step in the random-walk of each photon, and which depends on the particle size and concentration, and the refractive indices of the medium and the particle.

Actually, the analysis here presented is referred to the simplest case, which is that of non-interacting scatterers in the analysed sample. This assumption doesn't hold in strongly-interacting colloids, such as concentrated suspensions, in which the concentration of scatterers is high. This interaction affects l^* and the relationship between $g(\tau) - 1$ and $\langle \Delta r^2(\tau) \rangle$, in such a way that has been reported in several papers.

Assuming that the Stokes-Einstein equation [77] can be applied to all the frequencies, the unilateral Laplace transformation of the $\langle \Delta r^2(\tau) \rangle$ data, i.e. $\langle \Delta r^2(s) \rangle = \int_0^\infty \langle \Delta r^2(\tau) \rangle \exp(-s\tau) d\tau$, can be directly used to evaluate the complex modulus of the sample, putting $s = i\omega$:

$$G^*(\omega) = \frac{k_B T}{\pi R s \langle \Delta r^2(i\omega) \rangle} \tag{2.19}$$

where k_B is the Boltzmann constant, T is the temperature, and R is the radius of the tracer particles.

Lastly, as well known, the storage and loss moduli can be extracted by $G^*(\omega) = G'(\omega) + iG''(\omega)$.

Here, the behaviour of the model system is studied with the DWS Rheolab III (LS Instruments), in which the fluctuations of the intensity of the scattered light is measured in a number of speckles (in the so-called 'speckle pattern'), so that a large number of statistically-independent measurements are obtained. Then, the DWS Rheolab III automatically runs the over-described analysis, in which the $g(\tau)$ function is an average on all the speckles.

Thanks to its high sensitivity, the DWS Rheolab III can detect even subnanometer-displacements of small particles, up to very high frequencies.

Here, 15 drops of a solution of Polybead monodisperse polystyrene microspheres (d = 1μm, Polysciences Inc.) have been added to 10ml of wormlike micellar model system, and the scatter they generate has been measured using a 680nm laser in transmission-mode at T = 20°C

Fig.2.18 shows the obtained data, together with measurements from rotational rheometer (Sec.2.3.1).

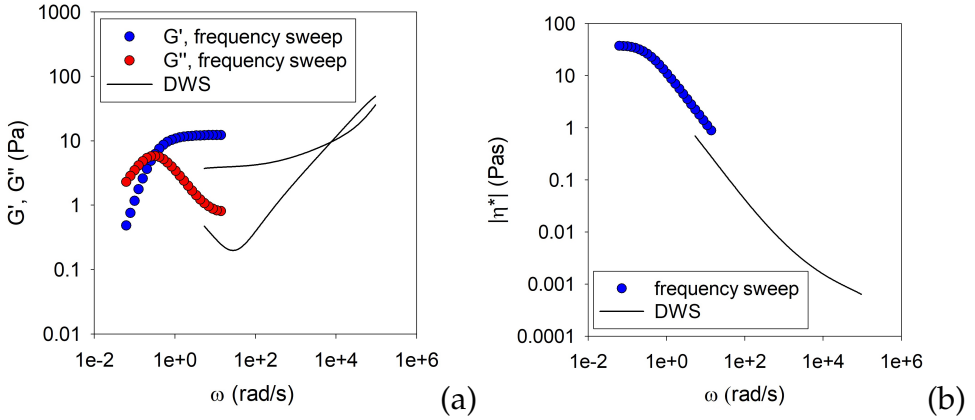

Fig. 2.18: *Oscillatory response: (a) storage and loss moduli from rotational rheology (●,●) and DWS (filled line); (b) complex viscosity from rotational rheology (●) and DWS (filled line)*

The values of G′ and G″ from DWS are shifted with respect to those from frequency sweep measurements. This shift has been related to uncertainties in the experiments and to interactions between the system and the particles [84]. Nevertheless, data can be just shifted up to get the overlap with measurements by mechanical rheology. Supplier suggests that, when the shifting-factor (i.e. $G'_{rheo}/G'_{DWS} = G''_{rheo}/G''_{DWS} = |\eta^*_{rheo}|/|\eta^*_{DWS}|$) is less than 10, the spectroscopy mea-

surements are reliable.

Fig.2.19 shows the corrected data, in terms of G′ and G″, and complex viscosity, $|\eta^*|$. This measurement has been replicated six times, and the average shift factor is 3.21.

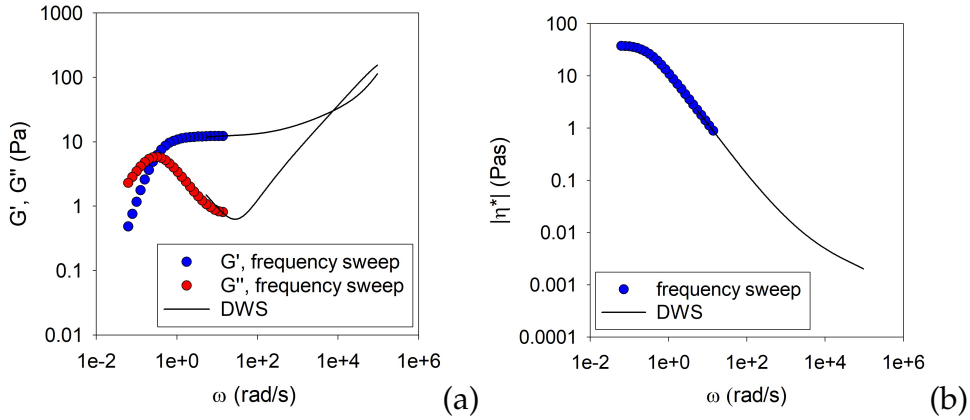

Fig. 2.19: *Oscillatory response: (a) storage and loss moduli from rotational rheology (●,●) and DWS (filled line); (b) complex viscosity from rotational rheology (●) and DWS (filled line) - corrected data*

2.4.2.1 Measurement of structural parameters

DWS measurements allow the evaluation of structural parameters [43, 84], i.e. the entanglement length, l_e, the persistence length, l_p, the average contour length, $\bar{L}$, and the mesh size, ξ. The used equations are

$$\omega_0 = \frac{k_B T}{8\eta_s l_p^3}, \quad \xi \sim \left(\frac{k_B T}{G_0}\right)^{1/3}, \quad l_e \approx \frac{\xi^{3/2}}{l_p^{2/3}}, \quad \frac{G''_m in}{G_0} \approx \frac{l_e}{\bar{L}} \tag{2.20}$$

where ω_0 is the frequency after which $G', G'' \sim \omega^{3/4}$, η_s is the solvent viscosity, k_B is the Boltzmann constant, T is the temperature, G''_{min} is the minimum of G'', and G_0 is the stress plateau (here evaluated as the value of G' corresponding to the minimum of G'').

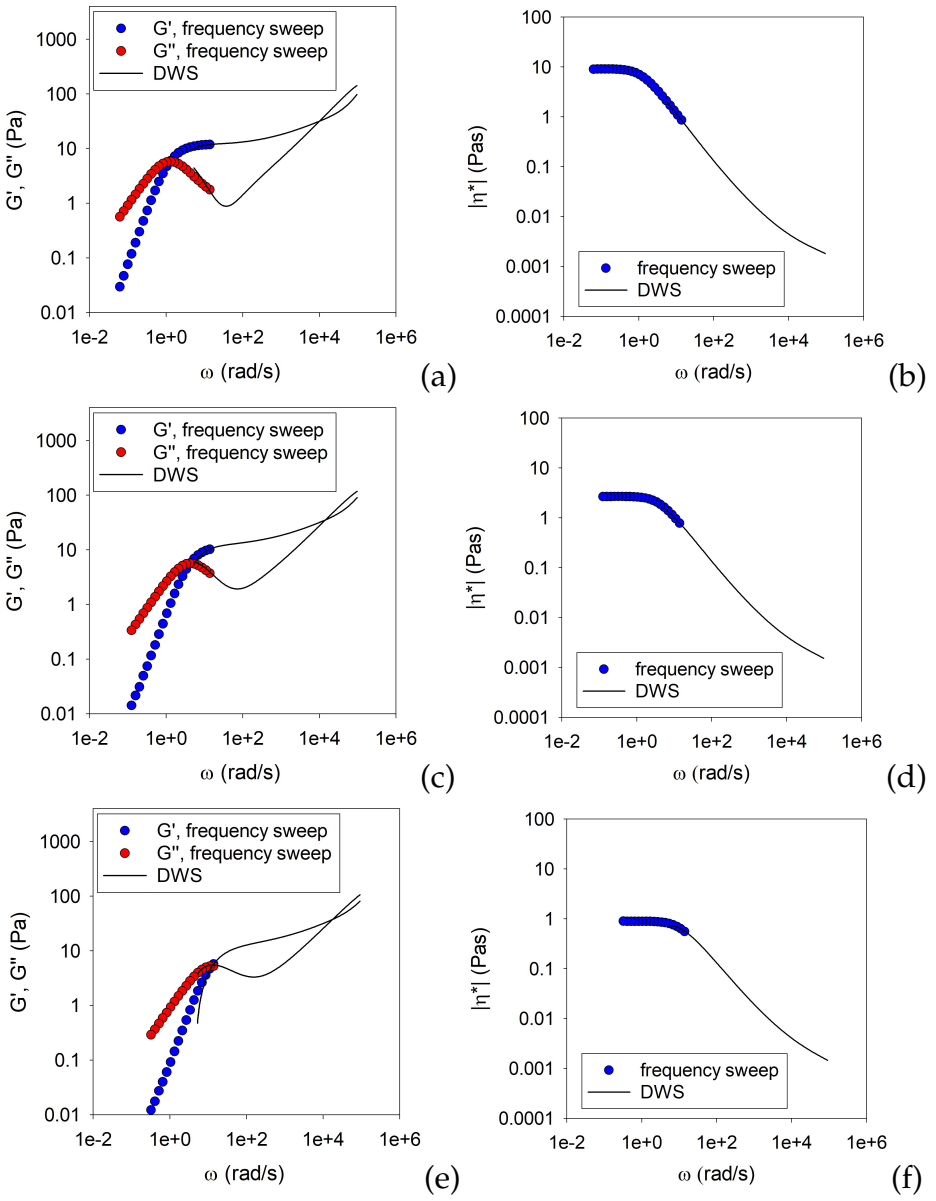

Fig. 2.20: *Oscillatory response from rotational rheology and DWS, in terms of storage and loss moduli and complex viscosity, at different temperatures: (a, b) T = 30°C, (c, d) T = 40°C, (e, f) T = 50°C*

Here, DWS measurements have been replicated at T = 30,40,50°C, in order to evaluate the effect of the temperature on the structural parameters. Every test has been replicated five times for each temperature. In order to measure the shifting-factor, SAOS measurements have been repeated at these temperatures, as well, using the procedure described in Sec.2.3.1.

Fig.2.20 shows the corrected data in terms of G' and G'', and complex viscosity, $|\eta^*|$.

Tab.2.4 reports the evaluated structural parameters as a function of the temperature. The value of the shifting-factor has been reported, as well. It can be appreciated how the temperature has a very slight effect on persistence and entanglement lengths, and mesh size, but has a major impact on the average contour length.

Lastly, Fig.2.21 shows that temperature affects the zero-viscosity much more than the high-frequency one, with no effect when $10^2 \text{rad/s} \lesssim \omega \lesssim 10^3 \text{rad/s}$.

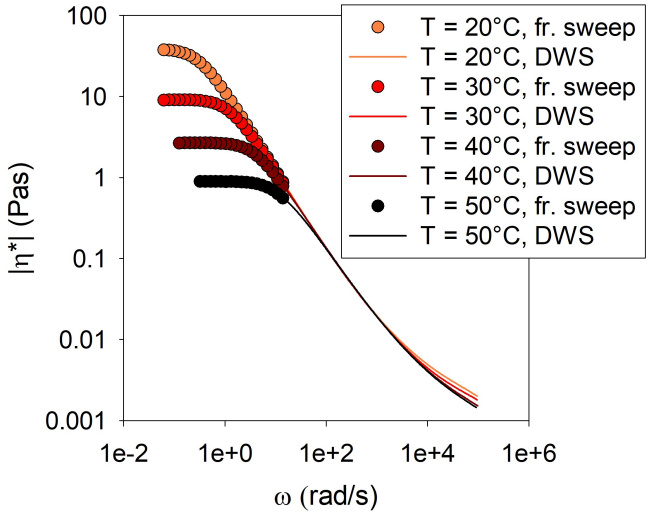

Fig. 2.21: *Complex viscosity from rotational rheology (circle) and DWS (line) as a function of the temperature*

Tab. 2.4: *Characteristic lengths and shifting-factor as a function of temperature*

T, °C	l_p**, nm**	ξ**, nm**	l_e**, nm**	$\bar{L}$**, nm**	**shifting-factor, -**
20	39.9 ± 0.45	68.8 ± 2.72	98.9 ± 6.00	2346.4 ± 361.4	3.21 ± 0.17
30	36.0 ± 0.94	73.4 ± 0.40	118.1 ± 2.60	1947.8 ± 251.1	3.23 ± 0.09
40	33.2 ± 0.56	70.6 ± 0.61	116.9 ± 1.89	777.2 ± 27.1	1.05 ± 0.05
50	31.1 ± 0.60	67.4 ± 1.70	112.9 ± 6.25	466.4 ± 34.4	0.36 ± 0.01

Chapter 3

Microfluidics

3.1 Abstract

Many analytical-techniques have been used to relate the rheology and fluid-dynamics of a wormlike micellar solution to its morphology, including particle image velocimetry (PIV) [57, 78], nuclear magnetic-resonance (NMR) [3, 71, 74], flow-induced birefringence (FIB) analysis [42, 50, 82], and scattering (SALS, SANS, SAXS) measurements [39, 72].

Among the others, microfluidics has been emerged in the last decade as a powerful tool to get a deeper insight into the flow-behaviour of a wormlike micellar solution [70, 80, 117, 119]. In fact, besides a number of other advantages that characterize this technique - such as low costs and chemical-consumption, fast responses, small space required for the setup - two features make microfluidics an elite instrument to study wormlike micellar solutions under flow-conditions. In fact, flow-instabilities are surface-force driven phenomena, and thus are promoted by highly-confined flow-geometries, such as a microfluidic channel.

Furthermore, microfluidic devices are small and clear. Thanks to this feature, microfluidics can be easily coupled to microscopy-techniques, this allowing a direct visualization of any flow-structuring phenomenon in the studied system.

Here, microfluidics has been coupled to advanced microscopy techniques and μPIV analysis, in order to study the wormlike micellar solution of interest, and the effect of flow-induced structuring on the evolution of velocity-profiles has been investigated.

3.2 Materials and methods

3.2.1 Model system

The model system is designed to couple optical and confocal analysis. In fact, in order to investigate the flow-behaviour of the wormlike micellar solution in confocal microscopy, a fluorescent dye has to be added to the system. Such a dye is not required in optical microscopy. Nevertheless, as already depicted, a slight change in the solution formulation - including the addition of a dye - can have a major impact on its rheology and microstructure.

Here, in order to remove this effect, the model system has been prepared only once, its formulation including the dye. Then, this system has been used both in confocal and optical microscopy experiments.

First, Rhodamine B (Sigma Aldrich) has been added to distilled water in a concentration of 10ppm. Then, the solution has been prepared as in Sec.2.2, replacing the distilled water with the solution water/rhodamine. Lastly, the system has been seeded with a solution of monodisperse polystyrene particles (d=1μm - Polysciences), whose

concentration is 2.5% solid (1 drop every 50ml of solution). The obtained system has been mixed for about two hours, and then left to stand at least one day.

3.2.2 Setup

The experiments have been performed in a 180µm inner-diameter silica-microcapillary (Polymicro Technologies), with a length of about 6cm.

For the bright-field experiments, the capillary has been connected through a 1mm inner-diameter ETFE tube (IDEX) to a micropump-system, consisting in a MFCSTM-FLEX pressure-driven flow-controller (FLUIGENT), and then placed on the motorized x-y stage of an Axiovert S100 TV inverted microscope (Zeiss), equipped with a v4.3 digital high-speed camera (Phantom). The flow on the capillary-midplane has been thus visualized using a N-Achroplan 100x/1.25 oil-immersion objective (Zeiss) (Fig.3.1).

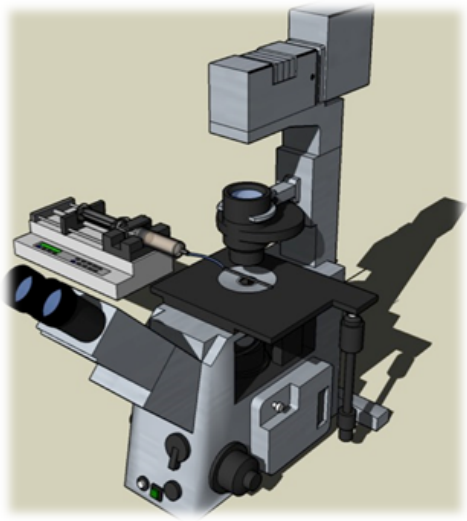

Fig. 3.1: *Schematic view of the experimental setup*

Furthermore, the same setup has been used to study any possible birefringence in the flowing solution. For this purpose, crossed polarizers have been placed above and below the capillary, and the flow on the capillary-midplane has been visualized using a Plan-Neofluar 40x/1.30 and an Achrostigmat 10x/0.25 objectives (Zeiss).

For the confocal light experiments, the capillary polyimide-coating has been removed through carbonization using a flame. Then, the capillary has been connected through a 1mm inner-diameter stainless-steel tube (IDEX) to a 10ml glass syringe (Hamilton), mounted on a PHD ULTRA programmable syringe-pump (Harvard Apparatus). The capillary has thus been placed on the stage of an LSM 5 PASCAL laser scanning microscope (Zeiss), and the flow on the capillary-midplane is visualized using a Plan-Apochromat 63x/1.4 oil-immersion objective (Zeiss) (Fig.3.1).

Due to its highly-elastic behaviour, the dripping of the solution outside the capillary induces periodic accelerations and decelerations of the solution inside the capillary, as qualitatively shown in Fig.3.2.

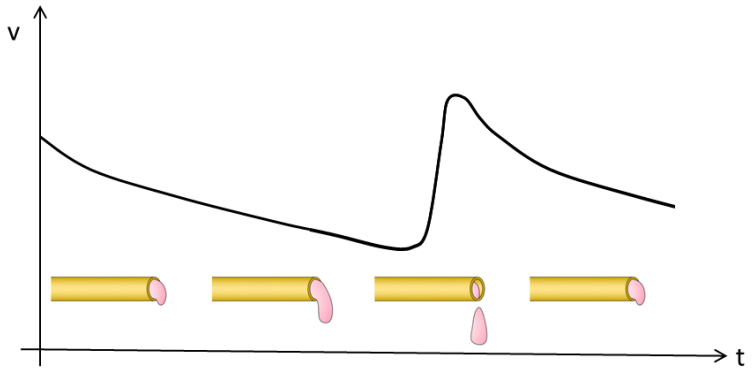

Fig. 3.2: *Effect of the dripping outside the capillary on the detected velocity of the solution*

In order to avoid this effect, the outlet of the capillary has been

immersed in the wormlike micellar solution, between two glass slides (Fig.3.3).

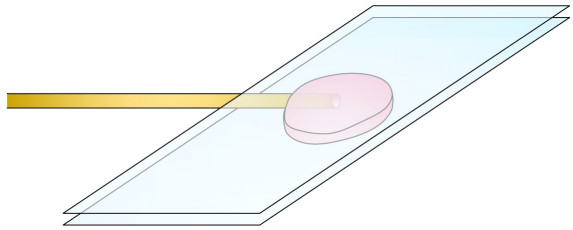

Fig. 3.3: *Outlet of the capillary, immersed in the wormlike micellar solution between two glass slides*

3.2.3 Particle-tracking

Particle-tracking is a powerful way to extract quantitative information from microfluidic experiments, and it has been successfully used to study the relationship between the onset of the shear banding and the alteration of the fluid velocity-pattern [11, 97]. Thus, it is worth matching all these techniques: thanks to optical microscopy, it is possible to visualize the flowing system and any structure within it; the particle-tracking analysis allows one to detect how the velocity-profile changes with the fluid-structuring; the microfluidics ensures the highly-sheared flow.

In the bright-field experiments, the high magnification of the objective allows one to visualize the 1μm polybeads suspended in the model system; on the other hand, the high acquisition-rate of the camera allows one to follow their motion through the capillary. Particles are small, inert, and added in small amount to the wormlike micellar solution; thus, they can be used as tracers, their motion describing the solution flow-behaviour.

In order to minimize any error, the tracking-procedure has been fully automated. In fact, the large array of images produced by the camera has been processed off-line using the automatic Track Object tool of the software Image-Pro Plus 6.0, which gives the position of each particle in every single image of the array.

Then, in order to extract the velocity-profile from these positions, the software MATLAB R2014b has been used to write a custom code, which evaluates the velocity of each particle, v_p, as

$$v_p = f \cdot \Delta x \cdot f_{cal} \tag{3.1}$$

where f is the acquisition-frequency of the camera, Δx is the displacement of a single particle between two subsequent frames (Fig.3.4), and f_{cal} is the spatial calibration-factor of the image.

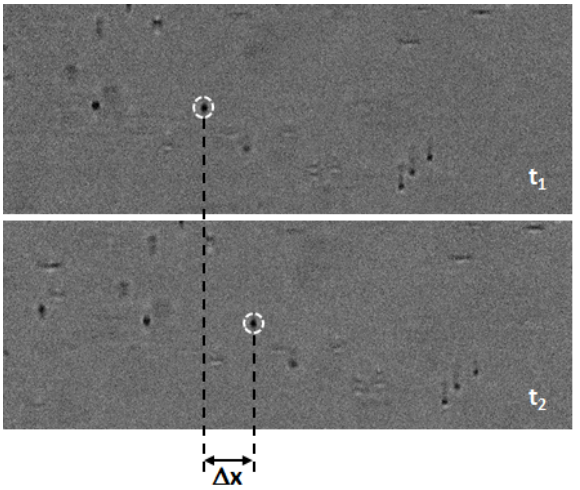

Fig. 3.4: *Displacement of a polystyrene particle between two subsequent acquired frames*

Then, the code groups the particles within the same radial position ($\pm 0.5\mu m$), and averages their velocities, thus giving the complete velocity-profile.

The difference in the refractive indices of the glass (n$\sim$1.48) and of the wormlike micellar solution (n$\sim$1.33), induces an apparent shift of the tracers-positions toward the capillary-centerline- The code takes into account this optical artifact, and corrects the velocity-profile by using the Snell's law. The formulas which allows one to make this correction are fully described in [104].

3.3 Velocity-profiles and flow-induced structuring

The effect of flow on the wormlike micellar microstructure has been studied over a wide range of fixed pressure-drop (ΔP = 100-375mbar), i.e. the pressure-drop in the overall setup. Sec.3.4.1 elucidates the correlation between this latter and the pressure-drop in the capillary.

The flow-induced response, expressed in terms of both velocity-profiles and structuring, is shown in Fig.3.5. To ensure that steady-state conditions have been reached, for every fixed pressure-drop, the experiments have been performed at least 3 times. In the following, the average velocity-profiles are reported, the error-bars representing the standard deviations. In order to avoid any entrance-effect, in every experiment the image acquisition has been performed at a distance of 3cm from the inlet.

At low pressure-drop ($\Delta P \leq$ 200mbar), there is no evidence of any structuring on high scale, and the velocity-profile looks almost flat. Actually, the velocity smoothly decreases moving from the centerline to the capillary wall.

Increasing the pressure-drop (210mbar $\leq \Delta P \leq$ 220mbar), the so-

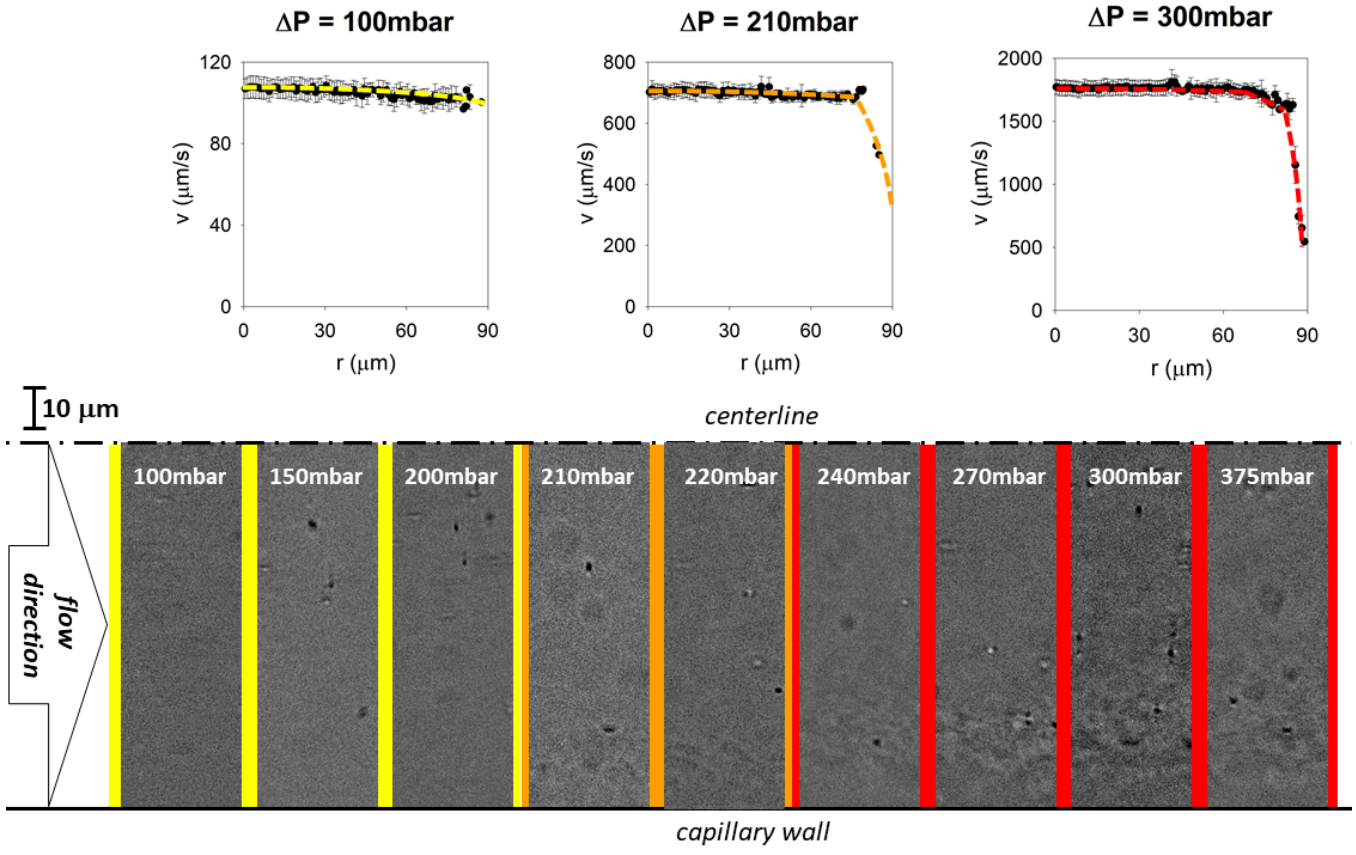

Fig. 3.5: *Correlation between flow-induced structuring and evolution of the velocity-profile*

lution still shows a plug-flow in the inner-core, while velocity dramatically decreases close to the capillary-wall. The transition between the two sections looks abrupt, this meaning that the velocity-profile shows a real discontinuity-point.

Together with the transition to a non-continuous velocity-profile, the solution shows the formation of a high-graininess zone close to the capillary wall, which seems to become bigger and bigger as the pressure-drop increases.

Fig.3.6 shows the correlation between the velocity-profile and the microstructure of the wormlike micellar solution under flow. As already depicted, the flat velocity-profile corresponds to an homogeneous microstructure; then, when 210mbar $\leq \Delta P \leq$ 220mbar, the discontinuity-point of the velocity-profile is located at the interface between the homogeneous and high-graininess zone.

Both Fig.3.5 and Fig.3.6 suggest a segregation of the tracer. In fact, for every velocity-profile, the most of the particles are detected in the plug-core zone, and just a couple of the hundreds analysed are located in the grainy-zone. Nevertheless, there is no evidence of a radial motion of the particles within the investigated window, this suggesting that segregation is already completed, or is still occurring on a scale larger than the analysed one.

This transition has been detected in confocal experiments, as well (Fig.3.6). Although the scanning-time of the confocal microscope results in a distortion of the acquired images, it is clear how crossing ΔP = 210mbar causes the rise up of flow-structures by the capillary walls.

A further increase of the pressure-drop ($\Delta P \geq$ 240mbar) results in an even more complex response (Fig.3.5). The velocity-profile shows three different slopes, with the onset of a new discontinuity-point, which corresponds to a further growth of the graininess-zone, eventu-

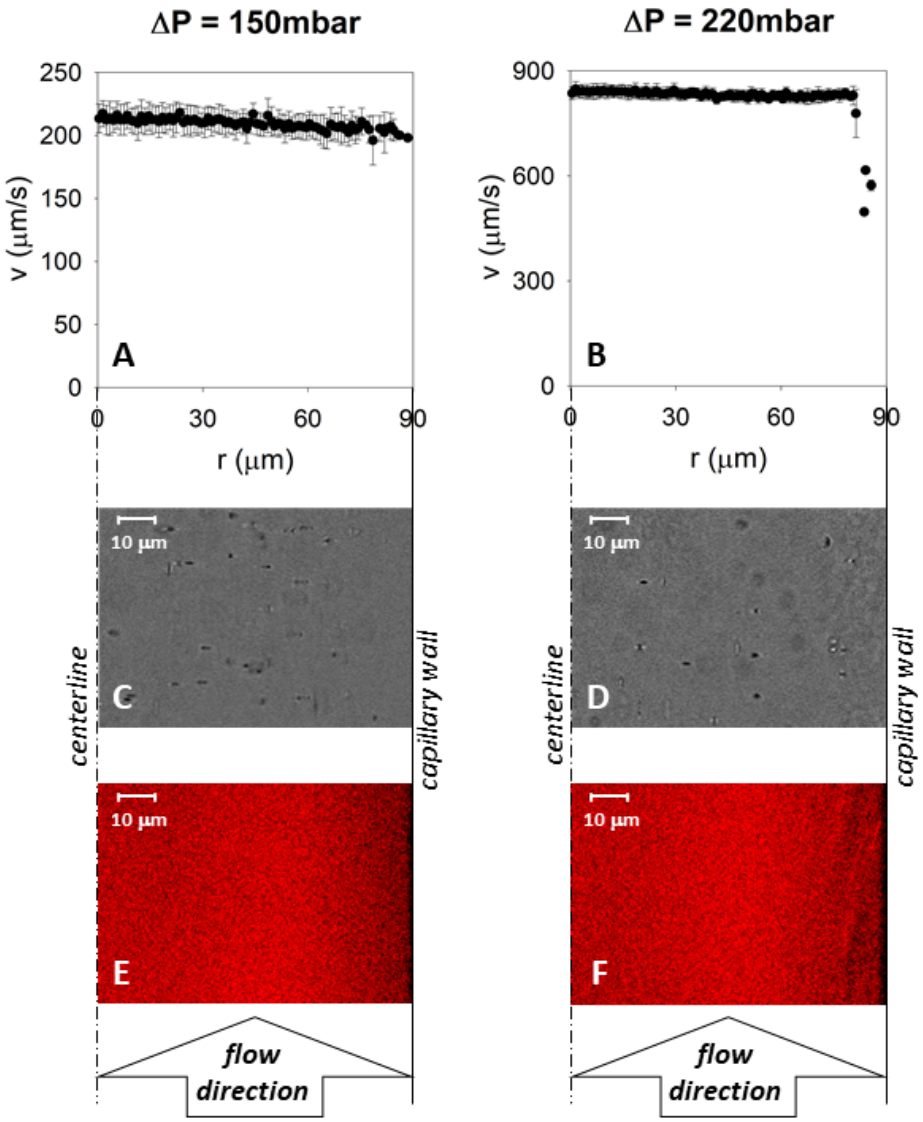

Fig. 3.6: *Correspondence between the sections of the velocity-profiles (top panels) and different phases of the solution, detected both in bright-field (center panel) and in confocal microscopy (bottom panel)*

ally leading to a detachment from the capillary-walls. The two discontinuity-points can be roughly located at the interface between the homogeneous zone and the high-graininess one, and where the structured fluid detaches from the walls.

The transition to a velocity-profile with two discontinuity-points occurs when $\Delta P = 240$mbar. Nevertheless, by looking at the plot in full scale, it can be quite hard to appreciate the three sections of the velocity-profile. Obviously, this behaviour can be easily detected by properly zooming the plot (Fig.3.7).

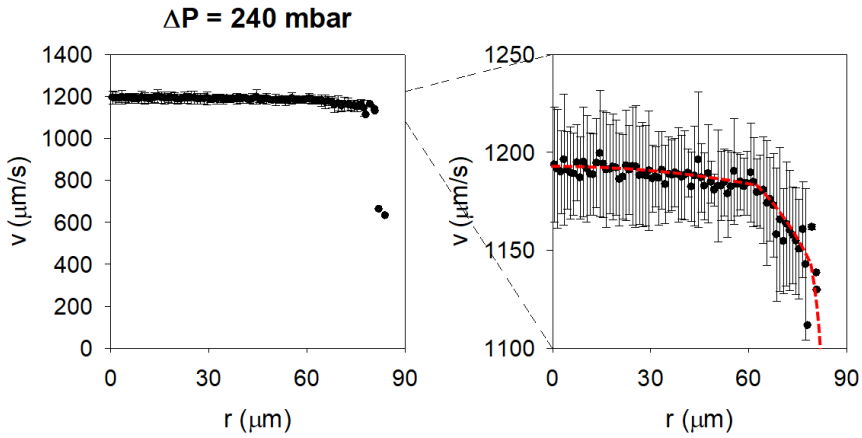

Fig. 3.7: *Velocity-profile at $\Delta P = 240$mbar, showing two discontinuity-points*

For every pressure-drop, the velocity seems to never reach the zero-value by the wall. Understanding if there's a wall-slip effect, or if the velocity abruptly goes to zero in a very thin layer by the wall, goes beyond the scope of this study. Using the particle-tracking technique, in fact, it is not possible to resolve the flow behavior on a characteristic length smaller than the particle diameter. This means that it has been impossible to describe the velocity-profile in a layer closer to the wall than 1μm.

The reliability of the automatic measurement of the velocity-profile has been investigated, too. For every pressure-drop, the flow-rate has been measured by weighting the solution flowing out of the capillary at predetermined intervals. Then, these values have been compared with the flow-rate obtained by integration of the velocity-profile.

As shown in Fig.3.8, the results perfectly superimpose for every pressure-drop, this proving that the velocity-profile has been correctly determined. The consistency of these measurements is shown by the error bar, which, in most data points, is about the same size as the symbols in the graph.

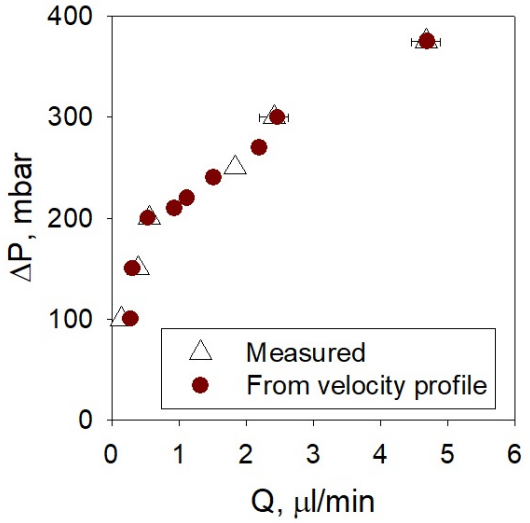

Fig. 3.8: *Flow rate as a function of pressure-drop, evaluated by weighting the capillary outflow at predetermined intervals (△) and by integration of the velocity-profile (●)*

Lastly, it is worth underlining that the flow-structuring doesn't result in a highly-ordered phase. In fact, there is no evidence of a birefringent behaviour of the graininess-zone (Fig.3.9), this proving that, even is such a concentrated system, the flow-structuring is not neces-

sarily related to the formation of a nematic phase.

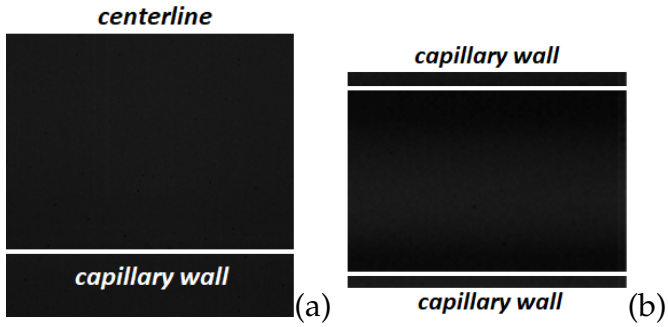

Fig. 3.9: *Birefringence-analysis at high pressure-drop (ΔP = 375mbar): (a) 40x and (b) 10x magnifications*

3.4 Microrheology

The analysis of the velocity-profiles can also provide a rheological characterization of the model system. In fact, the evaluation of both the shear rate and the shear stress is possible by using:

$$\dot{\gamma}(r) = \frac{dv}{dr}, \quad \tau(r) = \frac{\Delta P_{cap}}{L}\frac{r}{2} \tag{3.2}$$

where ΔP_{cap} is the pressure-drop in the capillary. As already depicted, this value differs from the fixed pressure-drop, and Sec.3.4.1 clarifies how it has been evaluated.

The $v(r)$ function has been obtained for every pressure-drop with a piecewise-polynomial fit of the measured velocity (Fig.3.10). Thus, every section of the velocity-profile has been fitted with a quadratic function, and the discontinuity-points have been used as junction-points, this meaning that the fitting functions of two adjacent sections of the velocity-profile have the same value in each discontin-

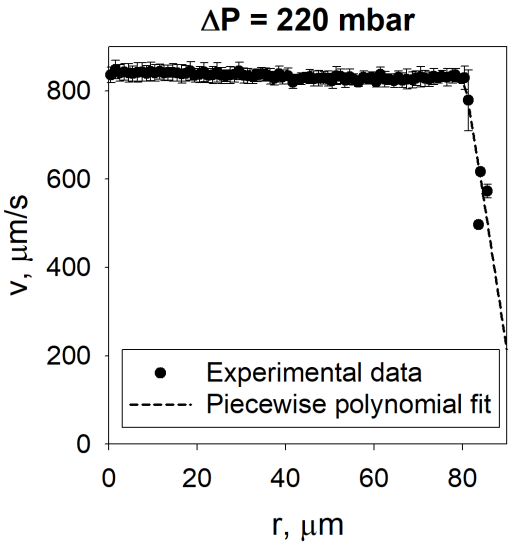

Fig. 3.10: *Velocity-profile at ΔP = 220mbar (●) and its piecewise-polynomial fit (dashed line)*

uity-point. Furthermore, the axial symmetry has been ensured by fixing $d\,v/d\,r = 0$ on the centerline.

The use of the particle-tracking analysis in a microfluidic device to get rheological information shows several advantages. First, this analysis overcomes the limits of both rotational rheometers, where it is hard to reach high shear rates, and commercial devices as the VROC, where the sensitivity of the instrument limits the minimum shear rate. In fact, when there are no wall-slip effects, thanks to this approach it is possible to reach shear rates as high as $10^7 s^{-1}$ [62].

Furthermore, this approach allows the study of the local response of the flowing solution, whereas commercial devices as the VROC analyse the bulk-behaviour of the system. As consequence, when particle-tracking and microfluidics are coupled to get rheological measurements, one experiment at fixed flow-rate provides the whole flow-curve - the higher the flow-rate, the wider the flow-curve - whereas

the VROC provides one point of the flow-curve for each flow-rate.

Lastly, the Eq.3.2 doesn't require any correction.

Fig3.11 shows the flow-curves obtained at three different values of ΔP. Measurements obtained with the rotational rheometer are reported, as well; their good agreement with analysis from microfluidic experiments confirms the robustness of microfluidic approach.

Furthermore, this analysis gives a deeper insight into the physical nature of the pseudo-plateau detected in bulk-rheology when ($\dot{\gamma} > \dot{\gamma}^* \simeq 1\text{s}^{-1}$). In fact, the analysis of the velocity-profiles shows that, at a location corresponding to the discontinuity-points, the solution exhibits one value of shear stress, but two values of the shear rate, this resulting in one or more discontinuities of the flow-curve. Thus:

- when $\Delta P \leq 200$mbar, the solution faces low shear rates ($\dot{\gamma} < \dot{\gamma}^*$);
- when 210mbar $\leq \Delta P \leq$ 220mbar, at a radius corresponding to the unique discontinuity-point of the velocity-profile, shear stress about equals the value at which the pseudo-plateau detected in rotational rheology begins. As already shown, this point is located at the interface between structured and homogeneous regions, and the value of shear rate in this latter is about $\dot{\gamma}^*$;
- when $\Delta P \geq 240$mbar, the second discontinuity-point leads to a new discontinuity in the flow-curve. In this case, the shear stress is within the range in which rotational rheometry shows a stress pseudo-plateau.

So, all the discontinuities of the velocity-profiles can be associated to points on the stress pseudo-plateau of the flow-curve; on the other hand, they are related to the rise up of a high-graininess zone in the flowing solution. Thus, for this model system, the onset of the stress pseudo-plateau is itself a signature of its flow-structuring.

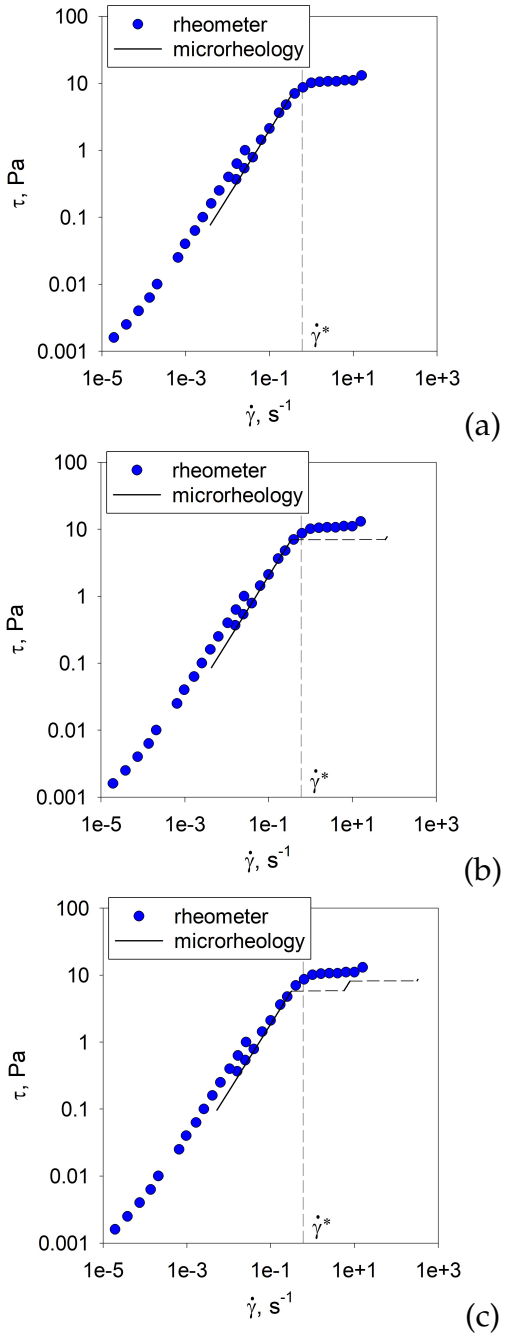

Fig. 3.11: *Flow-curve from the velocity-profile (dashed line) and from rotational rheology (●):*
(a) ΔP = 200mbar, (b) ΔP = 220mbar, (c) ΔP = 300mbar

3.4.1 Pressure-drop in capillary

As already pointed out, Eq.3.3 requires the value of pressure-drop in the capillary, whereas the fixed pressure-drop is the one in the whole setup. The relation between these two is:

$$\Delta P = \Delta P_{cap} + \Delta P_{inlet} + \Delta P_{tube} \tag{3.3}$$

where ΔP_{tube} is the pressure-drop in the ETFE tube connecting the pump to the capillary, ΔP_{inlet} is the concentrated pressure-drop due to the flow-section contraction at the capillary-inlet.

These two terms can be grouped in another one:

$$\Delta P_0 = \Delta P_{tube} + \Delta P_{inlet} \tag{3.4}$$

hence the Eq.3.3 becomes

$$\Delta P = \Delta P_{cap} + \Delta P_0 \tag{3.5}$$

As previously said, by weighting the solution flowing out of the capillary at predermined times, it is possible to evaluate the flow-rate as a function of the pressure-drop; replicating this procedure for several lengths, allows one to derive ΔP_{cap}, which is the only term in ΔP depending on the capillary length, as detailed in the following.

It has to be pointed out that data in Fig.3.12 are reported in double logarithmic scale, this making hard to appreciate the effective magnitude of the error-bars, whose actual size is reported in Fig.3.8.

Data in Fig.3.12 suggest a power-law dependence of the pressure-drop on the flow-rate. Assuming that both ΔP_0 and ΔP_{cap} show a power-law dependence on Q, Eq.3.5 becomes

$$\Delta P = a_1 Q^{n_1} + a_2 f(L) Q^{n_2} \tag{3.6}$$

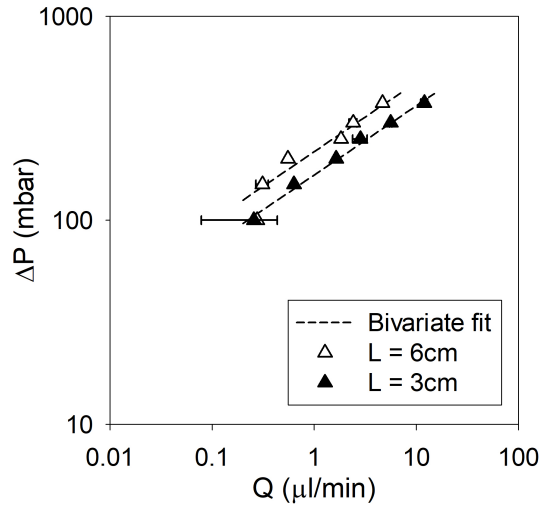

Fig. 3.12: *Pressure-drop in the setup as a function of the flow rate, at L = 3cm (△) and L = 6cm (▲), and bivariate fit of the data (dashed line)*

Considering $f(L)$ as a first-degree polynomial, the pressure-drop becomes:

$$\Delta P = a_1 Q^{n_1} + a_2 L Q^{n_2} \tag{3.7}$$

As shown in Fig.3.13, experimental data are in good agreement with this model, and, when $\Delta P[=]$mbar, $L[=]$cm and $Q[=]$µm, the fitting constants are a_1 = 123.44, a_2 = 15.16, n_1 = 0.28 and n_2 = 0.45.

Furthermore, the dependence of the only ΔP_{tube} as a function of the flow rate has been evaluated. Thus, the capillary has been removed, and a gravimetric-analysis of the solution flowing out of the tube has been carried out. As shown in Fig.3.13, data are properly fitted by:

$$\Delta P_{tube} = b Q^m \tag{3.8}$$

with b = 120.34 and m = 0.27 when $\Delta P_{tube}[=]$mbar and Q=µm. Once again, the small error bars in Fig.3.13 show the consistency of these measurements.

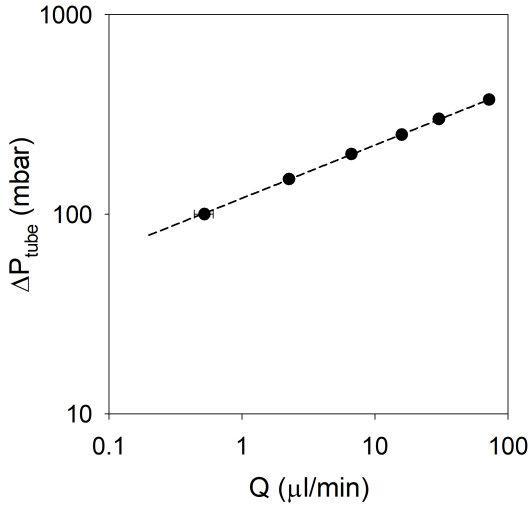

Fig. 3.13: *Pressure-drop in the tube as a function of the flow rate (●), and non-linear fit of the data (dashed line)*

Lastly, from the Eq.3.4, the term ΔP_{inlet} can be evaluated as the difference between ΔP_0 and ΔP_{tube} (Fig.3.14).

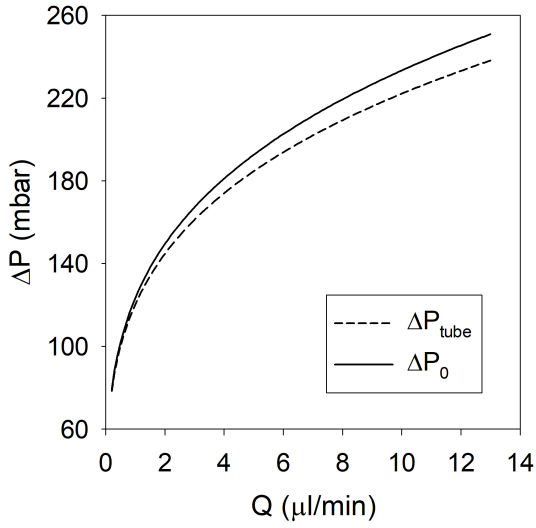

Fig. 3.14: *Fit of ΔP_0 as $\Delta P_0 = a_1 Q^{n_1}$, and fit of ΔP_{tube} as from Eq.3.8*

Chapter 4

Flow in pipes

4.1 Abstract

Although microfluidics allows one to get a microscopic and direct visualization of a flowing wormlike micellar solution, the flow-behaviour of such a system in a microfluidic device can hardly represent those in most common industrial operation-units.

In fact, the length scale of these units is orders of magnitude bigger than that of microfluidic devices, and thus confinement effects are mitigated.

Furthermore, industrial operation-units are usually not made of glass, and it is already been shown the effect of the flow-geometry material of the response of wormlike micellar systems (Sec.2.3.5).

For these reasons, scaling the results from microfluidics is required.

Here, the scale-up from a glass capillary to steel pipes is performed. This study has involved a number of different pipes, both in glass and in steel, and with different diameters, in order to separately study the impact of the length scale and the material of the flow-geometry on the behaviour of the wormlike micellar solution.

Measurements have been used to obtain rheological data. By properly choosing the investigated flow rates, experiments in pipes have been designed to fill the gap between the data obtained from mechanical rheology and those from the rheometer-on-a-chip.

4.2 Materials and methods

The model system has been prepared as in Sec.2.2.

As schematized in Fig.4.1, the scale-up from a glass capillary to steel pipes has been realized in several steps.

First, only the nominal diameter (DN) of the flow-geometry has been changed, leaving the material unchanged; thus, a set of glass pipes with nominal diameter of 1mm (DN1) has been used. Then, the glass pipes have been replaced with a set of standard-steel (SS) pipes, leaving the nominal diameter unchanged (DN1). Lastly, the nominal diameter has been changed once again, by using a set of SS pipes with nominal diameter of 6mm (DN6).

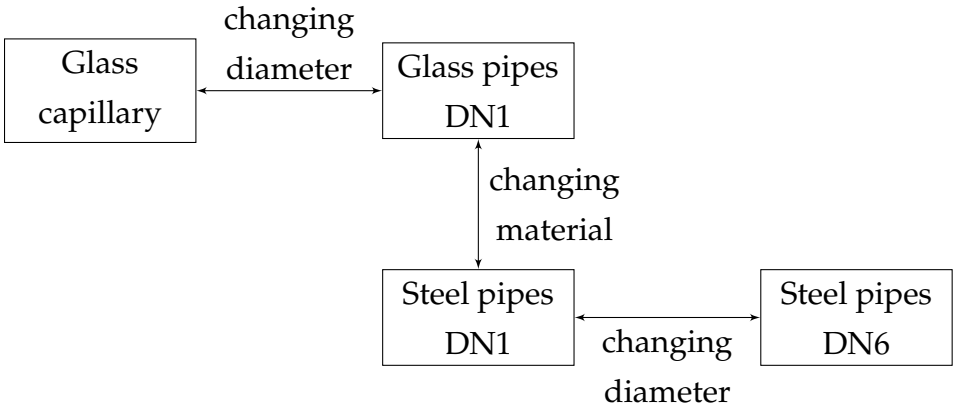

Fig. 4.1: *Steps for scale-up from glass microcapillary to steel pipes*

Each set consists of a number of pipes of different lengths. For each diameter and material of the pipe, in fact, several lengths have been used, in order to evaluate the effect of the residence-time. Furthermore, most measurements require some post-processing, in order to remove the additional pressure-drop related to entrance and exit effects. This correction requires the evaluation of the pressure-drop as a function of the length of the pipe (L_{pipe}), for fixed flow-rate, as elucidated in Sec.4.2.1.1. The flow through the pipe has been provided by a 500D syringe-pump (Teledyne Isco). The outlet of the pump is a plastic piping, which is connected through a SS 90° elbow to a SS pipe (DN6). This latter feeds the pipe selected for the experiment, whose outlet is connected to a SS pipe (DN6). The setup ends with another SS 90° elbow and another SS pipe (DN6) (Fig.4.2).

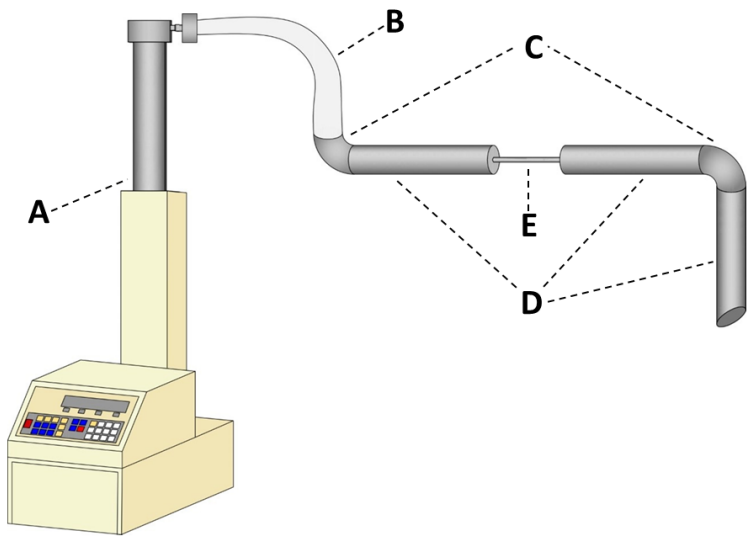

Fig. 4.2: *Schematic view of the experimental setup: (A) syringe pump, (B) plastic piping, (C) SS 90° elbows, (D) SS pipes (DN6), and (E) selected pipe*

Tab. 4.1: *Summary of the differences between the experiments in pipes*

Pressure-drop measurements system	**Pipe**			**Investigated flow-rate, ml/min**	**Scheme**
	Material	**DN, mm**	L_{pipe}**, cm**		
Pressure sensors	SS	1	5, 7, 10, 30	0.12-83.75	Fig.4.3(b)
	SS	6	30, 80	0.001-83.75	Fig.4.3(a)
	Glass	1	10, 30	0.12-16.75	Fig.4.3(c)
Differential-pressure transmitter	SS	1	5, 7, 10, 30	0.0008-0.84	Fig.4.3(b)
	Glass	1	10, 30	0.012-0.18	Fig.4.3(c)

The most of the measurements has been performed with pressure-sensors (AutomationDirect). Nevertheless, when the pressure-drop is low, measuring the pressure in two different points of the setup induces a big error. For this reason, some measurements have been performed using a Deltabar PMD75 differential-pressure transmitter (Endress+Hauser).

Tab.4.1 summarizes the differences between the experiments.

4.2.1 Results

Similarly to the analysis described in Sec.2.4.1, rheological information can be obtained by extracting the shear rate from the fixed flow-rate, and the shear stress from the measured pressure-drop, and then applying the Weissenberg-Rabinowitsch-Mooney (W.R.M.) correction [75]:

$$\tau = \frac{\Delta P}{L_{pipe}} \frac{R}{2}, \quad \dot{\gamma}_a = \frac{4Q}{\pi R^3}, \quad \dot{\gamma} = \frac{\dot{\gamma}_a}{4} \left(\frac{1+n}{n} \right) \tag{4.1}$$

where $n = d\,log(\tau)/d\,log(\dot{\gamma}_a)$, and R is the radius of the pipe.

Moreover, depending on the selected pipe, the Bagley correction might or might not be necessary. For example, when a DN6 SS pipe is used, the solution faces neither contractions nor expansions between the point P_1 and P_2 at which the pressure is measured (Fig.4.3a). Furthermore, the distance between these two points is exactly L_{pipe}. For these reasons, Eq4.1 can be directly applied.

When the other pipes (Fig.4.3b, Fig.4.3c) are used, on the contrary, the measured pressure-drop takes into account of extra-terms, due to the contractions and expansions of the flow-geometry, and to the fact that the distance between P_1 and P_2 is bigger than L_{pipe}. Performing the well-known Bagley correction, the sum of these terms has been evaluated, and removed from the measured pressure-drop.

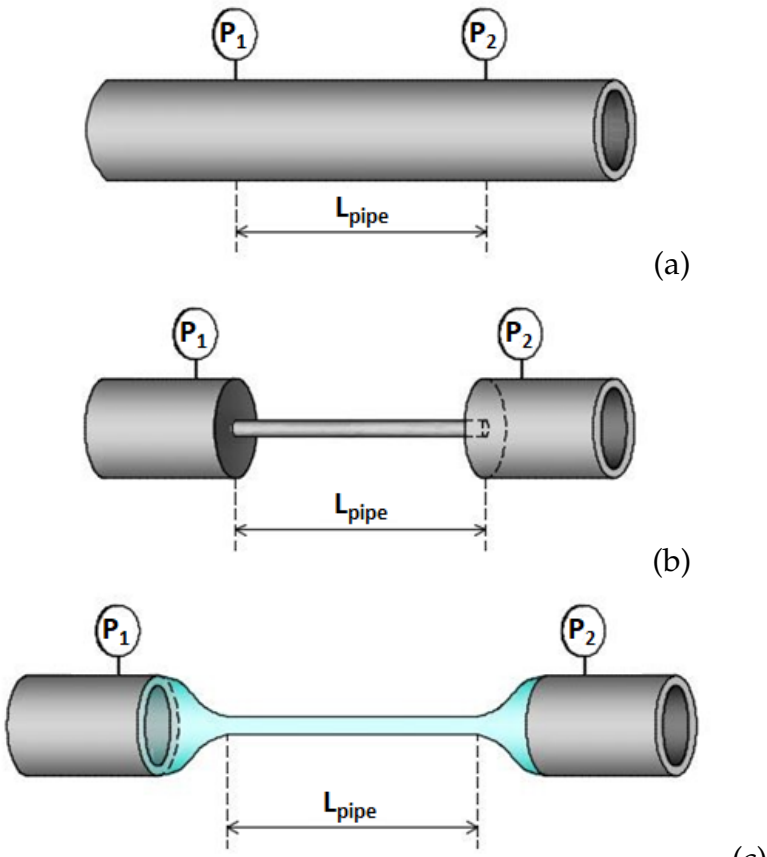

Fig. 4.3: *Position of the pressure measurement-device and shape of the flow-geometry for different selected pipes: (a) steel DN6, (b) steel DN1, (c) glass DN1*

4.2.1.1 Bagley correction and modelling

For every set of pipes, the pressure-drop has been measured and modelled as a function of both the flow rate and the length of the pipe, $\Delta P(Q, L_{pipe})$. Once such a model has been obtained, the extra-term that has to be removed (ΔP_0) can be by obtained putting $L_{pipe} = 0$.

First, the Bagley plot has been built. Thus, ΔP has been plot at constant flow rate versus L_{pipe}/R, and then a linear fit of the data has been performed (Fig.4.4). The extrapolation to zero of such a fit gives ΔP_0 for fixed flow-rate.

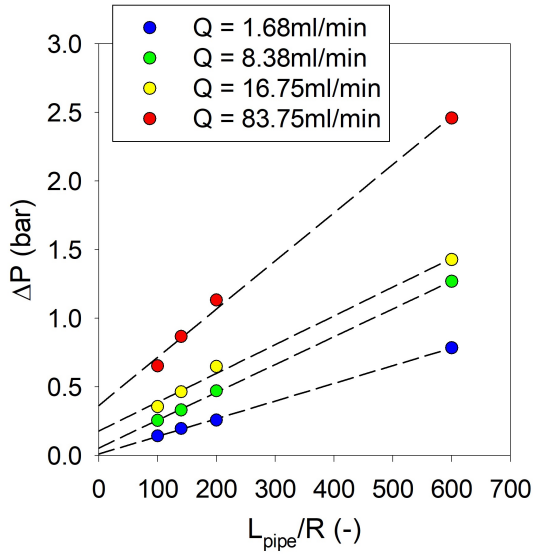

Fig. 4.4: *Bagley plot for selected flow-rates*

In principle, such a procedure would allow the evaluation of the effective pressure-drop, ΔP_{pipe}, from every measurement. Actually, for a few experiments ($\sim 10\%$), just one length of the pipe is used for each flow-rate. For this reason, ΔP has to be modelled as a function of both the length of the pipe and the flow-rate, in order to extrapolate ΔP_0 where experiments don't allow its evaluation.

Bagley plot shows the linear dependence of ΔP on the ratio L_{pipe}/R. Thus,

$$\begin{aligned}\Delta P(Q,L) &= \Delta P_0(Q) + \Delta P_{pipe}(Q,L) \\ &= \left(a\frac{L_{pipe}}{R} + b\right) f(Q) \end{aligned} \tag{4.2}$$

where the only dependence of the flow-rate, $f(Q)$, has to be evaluated.

The term $\Delta P_0(Q)$ is independent of the length of the pipe, thus

$$\Delta P(Q,L) = a\frac{L_{pipe}}{R} f_1(Q) + b f_2(Q) \tag{4.3}$$

$$\Delta P_{pipe}(Q,L) = a\frac{L_{pipe}}{R} f_1(Q), \;\; \Delta P_0(Q) = b f_2(Q) \tag{4.4}$$

Fig.4.5 shows ΔP_0 as a function of the flow-rate, for SS DN1 and glass DN1 pipes.

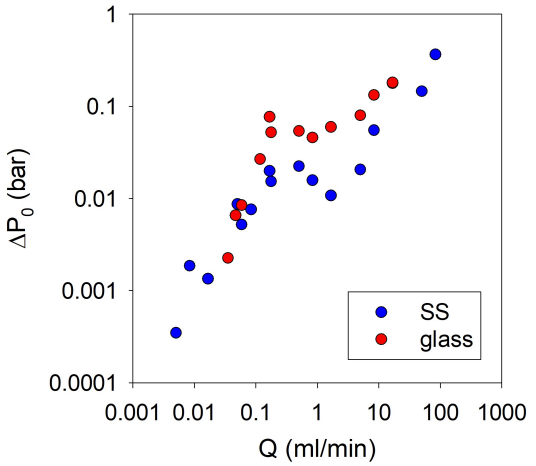

Fig. 4.5: *ΔP_0 as a function of the flow-rate, in steel DN1 pipes (●) and glass DN1 pipes (●)*

The term ΔP_0 is not strictly monotone - neither in steel or glass pipes - and, regardless of the material of the pipe, it doesn't increase

with the flow-rate, when 0.17ml/min<Q<1.68ml/min. It is not possible to discern if ΔP_0 is actually decreasing or showing a plateau - i.e. the negative trend of the data is just fictitious and related to experimental-error. This behaviour could be related to the onset of complex flow-phenomena in the contraction and expansion.

Because of this behaviour, the multivariate-fit indicated in Eq.4.3 has been separately performed in the three ranges of flow-rate, i.e. Q<0.17ml/min, 0.17ml/min<Q<1.68ml/min and Q>1.68ml/min.

Among other functions, $f_1 = c_1 Q^{n_1}$ and $f_2 = c_2 Q^{n_2}$ are the best suitable for fitting all the data.

In conclusion, the model used to describe the pressure-drop is

$$\Delta P(Q, L) = k_1 \frac{L_{pipe}}{R} Q^{n_1} + k_2 Q^{n_2} \tag{4.5}$$

where $k_1 = ac_1$, $k_2 = bc_2$, n_1 and n_2 are defined just on a specific range of flow-rate.

4.2.1.2 Flow-curve

Eq.4.5 allows the evaluation of the effective pressure-drop in the pipes, $\Delta P_{pipes} = k_1 L_{pipe} Q^{n_1} / R$, when a SS DN1 pipe or a glass DN1 pipe is used. As already depicted, ΔP_{pipes} is directly measured in SS DN6 pipes.

Fig.4.6 shows the flow-curve extracted from Eq.4.1. For every set of pipes, measurements at the same shear rates have been reported as average in a single point (together with the error-bar), regardless of those factors which don't affect the shear stress - i.e. the length of the pipe, and the pressure-drop measurement-system.

Fig.4.7 confirms that the different values of the shear strain in the experiments don't affect the measurements. In fact, by using the shear

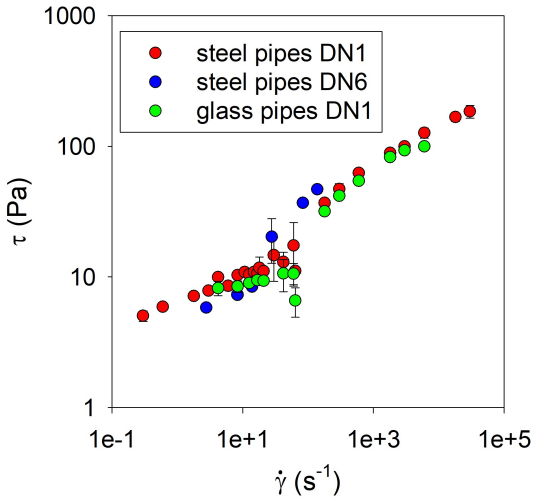

Fig. 4.6: *Flow-curve from the three sets of pipes: steel DN1 (●), steel DN6 (●) and glass DN1 (●)*

strain as colour-scale of the points on graph, no real trend of the data can be appreciated.

Except for the range $25\text{s}^{-1} \lesssim \dot{\gamma} \lesssim 123\text{s}^{-1}$, all the measurements are

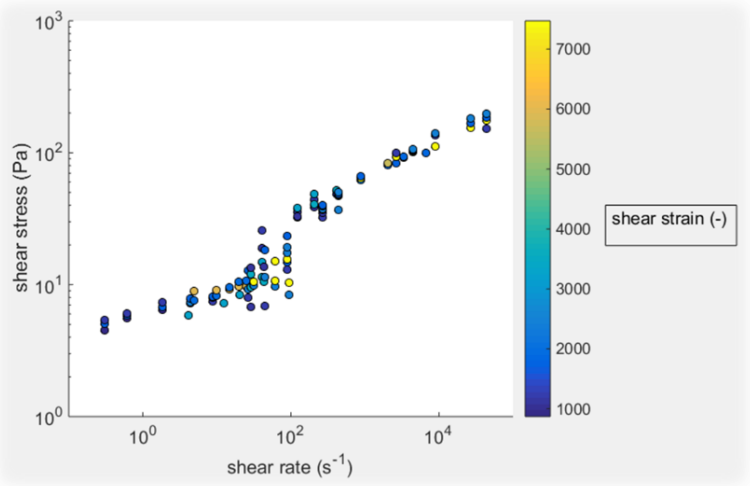

Fig. 4.7: *Shear stress against shear rate, parametric in shear strain*

consistent for every set of pipes. In fact, they show very small error-bars. Furthermore, data from the three sets of pipes collapse on the same flow-curve.

The agreement of the flow-curves is not trivial, as different materials have been used. This result is consistent with the evidence that the effects of the wall-slip are not detectable above 500μm (Sec.2.3.5).

Within the range $25\text{s}^{-1} \lesssim \dot{\gamma} \lesssim 123\text{s}^{-1}$, data are very scattered for every set of pipes. A comparison with data from rotational rheometer (Fig.4.8) shows that this range is located right at the end of the stress pseudo-plateau. This suggests that the dynamic response of the wormlike micellar solution exiting the stress pseudo-plateau is complex, too.

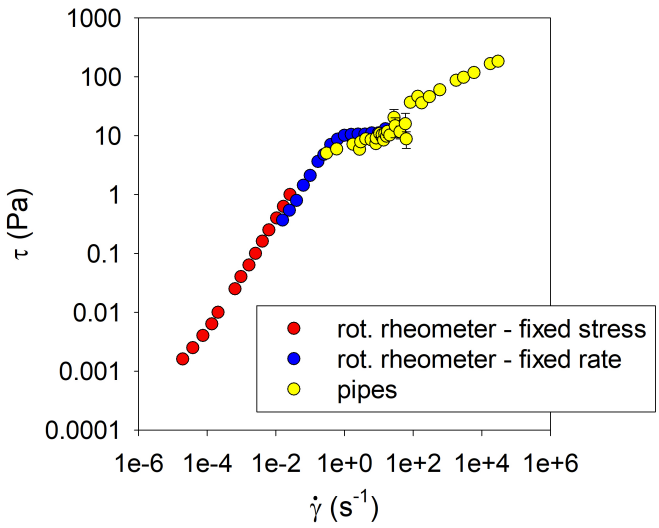

Fig. 4.8: *Flow-curve from measurements of pressure-drop in pipes (●) and from rotational rheology (●,●)*

Chapter 5

CFD analysis

5.1 Abstract

Computational Fluid Dynamics (CFD) is a powerful tool to simulate process-phenomena such as fluid-flow, mass and heat-transfer, or chemical reactions in various industrial operation-units, as reactors, pipes, mixers and pumps, through the numerical solution of the mass, momentum and energy equations.

Here, CFD analysis has been carried out on the selected model system, assuming a pure-thinning behaviour.

The flow-curve and the model of slip-velocity previously obtained have been here used to simulate the flow of the wormlike micellar solution through a glass microcapillary. The geometry and conditions have been properly designed to simulate the flow-channel used in the experiments (Sec.3.3), and the fully-developed flow-condition has been checked.

Velocity-profiles predicted from the simulation have then been compared with experimental data from microfluidics, in order to assess the validity of the hypothesis of pure-thinning behaviour.

5.2 Simulation

The numerical simulation has been carried out with the software COMSOL Multiphysics. A 2D-axialsymmetric geometry has been implemented, and steady-state study has been performed, using a laminar flow module.

The flow-geometry consists of a rectangle (width = $9 * 10^{-5}$m, height = $1 * 10^{-2}$m). The inlet, outlet and wall conditions have been set as reported in Fig.5.1.

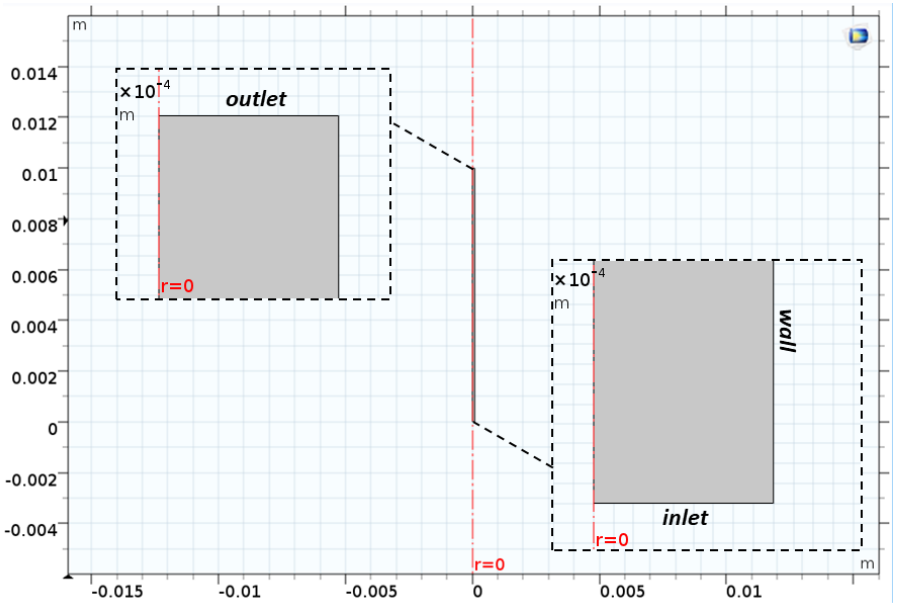

Fig. 5.1: *Flow-geometry and boundary-conditions implemented in COMSOL Multiphysics*

At the inlet, a plug-flow condition has been fixed, and the fully-developed flow has been analysed. In order to verify that the implemented length of the pipe ensures this condition, the overlapping of the velocity-profiles at several distances from the inlet (d = $8 * 10^{-3}$m

and $9 * 10^{-3}$m) has been verified.

The mesh selected is physics-controlled and extremely fine.

5.2.1 Material properties

The solution density is 995kg/m^3, and the viscosity has been evaluated from the measured flow-curve, taking into account all the rheological measurements done so far (Fig.5.2).

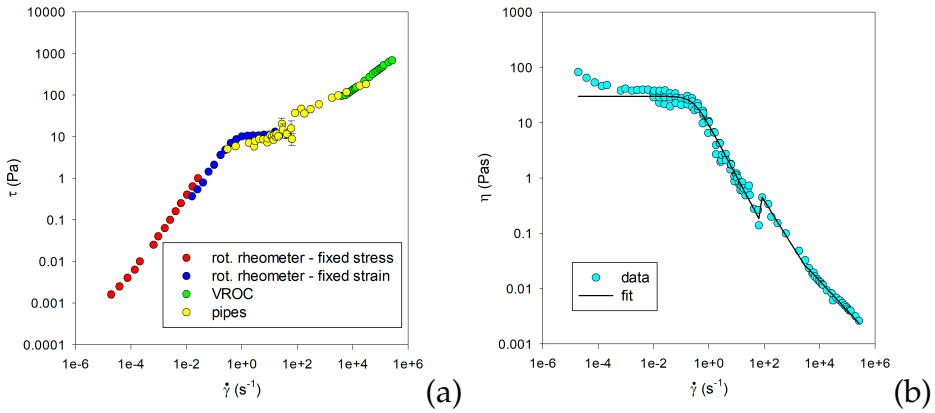

Fig. 5.2: *Rheological data from several techniques: (a) flow-curve from rotational rheology (●,●), pressure-drop measurements in pipes (●) and rheometer-on-a-chip (●), and (b) viscosity (from all the techniques)*

In order to implement the viscosity as a piecewise function, data has been grouped and fitted in four ranges (Fig.5.3):

- when $\dot{\gamma} \leq 63.64\text{s}^{-1}$, data have been fitted to a Carreau model:

$$\eta = \eta_0 + \frac{\eta_\infty - \eta_0}{(1 + (\lambda\dot{\gamma}))^n} \tag{5.1}$$

  where η_0 = 0Pas, η_∞ = 30.14Pas, λ = 3.46s, and n = 0.47;
- when $83.38\text{s}^{-1} \leq \dot{\gamma} \leq 3001.67\text{s}^{-1}$, a power-law has been used, thus $\eta = k_1\dot{\gamma}_1^n$, with $k_1 = 15.51$ and $n_1 = -0.80$ when $\eta[=]$ Pas and $\dot{\gamma}[=]$ s^{-1};

- when $3001.67\text{s}^{-1} \leq \dot{\gamma} \leq 261660.59\text{s}^{-1}$, a second power-law has been used, and $\eta = k_2\dot{\gamma}_2^n$, with $k_2 = 1.98$ and $n_2 = -0.54$ when $\eta[=]$Pas and $\dot{\gamma}[=]$ s^{-1};
- lastly, when $63.64\text{s}^{-1} \leq \dot{\gamma} \leq 83.38\text{s}^{-1}$, a linear function has been assumed, $\eta = a + b\dot{\gamma}$, with $a = -0.84$Pas and $b = 0.02\text{s}^{-1}$.

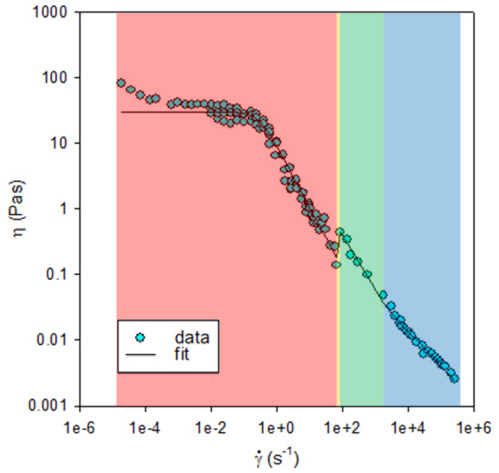

Fig. 5.3: *Fit of the viscosity over four ranges of shear rates*

5.3 Results

Aim of this simulation is to compare the velocity-profile predicted from the CFD analysis for a pure-thinning fluid with results from microfluidics.

For this reason, the fixed velocity at the inlet of the pipe has to be such that the flow-rate is the same as measured in microfluidic experiments (Fig.3.8). Obviously, this value can be easily evaluated as $v_{in} = Q/(\pi R^2)$ (Tab.5.1), where Q has already been evaluated by integration of the experimental velocity-profiles (Sec.3.3).

Moreover, the wall-slip behaviour has to be simulated. Here, a pa-

Tab. 5.1: *Flow-rate and plug-velocity at the inlet of the capillary, for every pressure-drop*

ΔP, **mbar**	**Q**, **µl/min**	v_{plug}, **m/s**
100	0.285	1.0E-4
150	0.306	2.0E-4
200	0.536	3.5E-4
210	0.931	6.1E-4
220	1.117	7.3E-4
240	1.519	9.9E-4
270	2.193	1.4E-3
300	2.462	1.6E-3
375	4.690	3.1E-3

rametric-sweep of the slip-velocity has been performed, and the shear stress at the wall has been evaluated. As shown in Fig.5.4, among

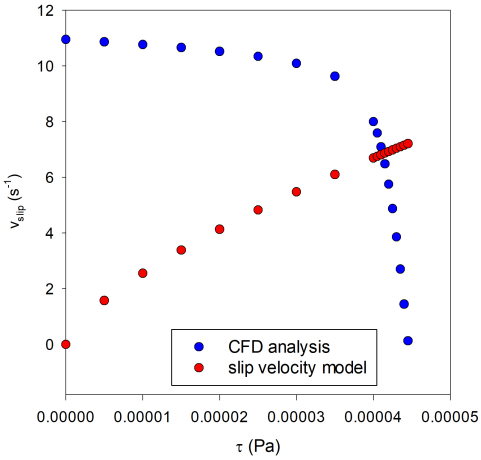

Fig. 5.4: *Slip-velocity vs wall shear stress from wall-slip model (●) and numerical simulation (●)*

all these simulations, only one can be accepted, as only one couple of values (v_{slip},τ) satisfies the model of wall-slip developed in Sec.2.3.5.1.

Results of this analysis are reported in Fig.5.5 for three values of the inlet-velocity.

At very low inlet-velocity (v_{plug} = 1.0E-4m/s and ΔP = 100mbar), the CFD analysis is in perfect agreement with the data from experiments. On the other hand, for high values of the inlet-velocity (v_{plug} = 3.1E-3m/s and ΔP = 375mbar), the simulation is not able to predict the flow-behaviour of the solution. This, together with the evidence of directly-visualized flow-structuring, proves that the flow-behaviour is more complex than that of a pure-thinning fluid.

Lastly, it is worth underlining the difference between the predicted velocity-profile and the measured one, when v_{plug} = 2.0E-4m/s and ΔP = 150mbar. Under these conditions, there is no evidence of flow-structuring on high scale (Sec.3.3), and the measured shear rate is too small to reach the stress pseudo-plateau (Sec.3.4); nevertheless, the assumption of pure-thinning fluid is not good enough to predict the real flow-behaviour of the wormlike micellar solution. This discrepancy suggests the presence of some complex phenomena on a scale smaller than the detected one.

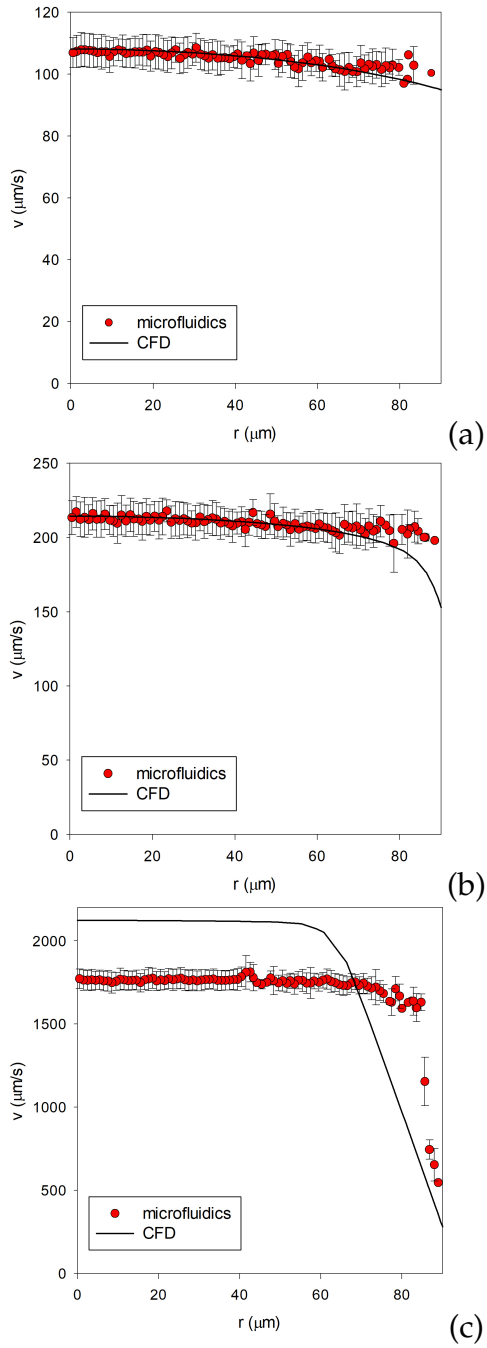

Fig. 5.5: *Comparison between experimental (●) and predicted (filled line) velocity-profiles for (a) ΔP = 100mbar, (b) ΔP = 150mbar and (c) ΔP = 300mbar*

Chapter 6

Concentration-gradients

6.1 Abstract

Direct-visualization of the flowing solution in a microchannel has shown the onset of structuring phenomena under strong-flow conditions. The values of the shear rate within such structures are consistent with the stress pseudo-plateau detected with rotational rheometry.

On one hand, dynamic response of the model system in rotational rheometer is consistent with an isotropic-to-nematic transition within the stress plateau, on the other hand there is no evidence of a high-ordering within the structures developed in the microchannel, as the birefringence-analysis highlights.

Here, microfluidics is coupled with rheology, electrical-conductivity and dry-mass measurements, in order to further investigate the physical nature of the shear-induced structures, with particular focus on the possible onset of flow-induced concentration-gradients.

6.2 Materials and methods

The model system has been prepared as in Sec.2.2.

In order to investigate the possible concentration-gradients developed within the flowing system, a microfluidic 'splitter' has been used. This consists in a 1-in-3 flow-geometry. Fig.6.1 shows the principle of the experiment: if the solution flowing in the main channel shows a concentration-gradient c(r), the split of the main flow in three different channels provides three outflows characterized by diverse concentrations; when the flow-geometry is symmetric, the two side-outflows have the same concentration.

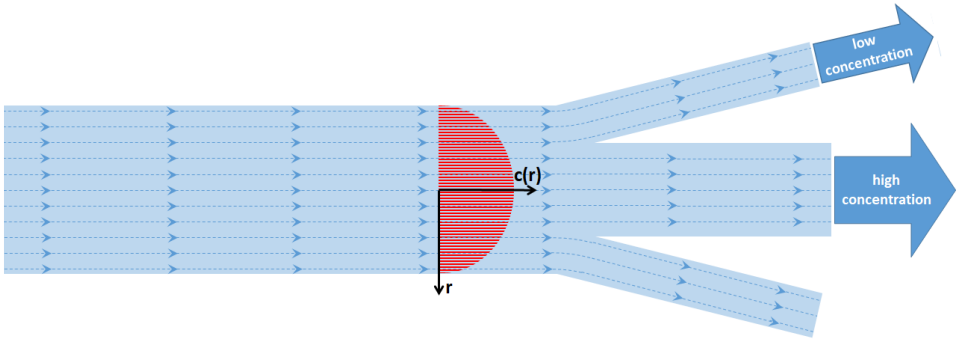

Fig. 6.1: *Operating principle of the splitter*

Here, the selected flow-geometry is a μ-Slide III 3in1 (Ibidi) (6.2), made of a hydrophobic polyethylene-derivative. The height of all the channels is 0.4mm. The μ-Slide is connected through a 1mm inner-diameter stainless-steel tube (IDEX) to a 100μl glass syringe (Hamilton), mounted on a PHD ULTRA programmable syringe-pump (Harvard Apparatus).

The solution flowing out of each channel has been collected and stored for less than one day. The steady-state viscosity of the samples has been measured at 20°C in a controlled-stress rheometer (AR-

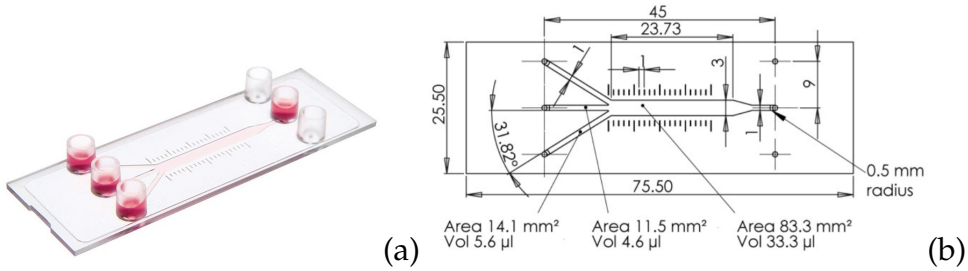

Fig. 6.2: *Flow-geometry:* µ*-Slide III 3in1 [125] and its main characteristic dimensions [126]*

G2, TA Instruments), equipped with a standard-steel cone geometry (D=25mm, cone angle=2°). Rheometer has been used in shear stress mode, and the samples have been conditioned for 60s at the desired temperature before each measurement. Furthermore, the electrical-conductivity of the samples has been measured using a PC 2700 conductivity-meter (Eutech Instruments). Lastly, samples have been placed in oven for three days, then their dry-weight has been measured.

6.3 Results

In order to study the effect of shear rate on the development of concentration-gradients, two different values of flow-rate have been studied.

Fig6.3 shows the viscosity of the collected samples, as a function of the shear rate. At lower value of flow-rate (Q = 1ml/h), all the samples show almost the same viscosity, and the differences between the curves can be barely appreciated. On the other hand, for high value of the flow-rate (Q = 10ml/h), the viscosity of the fluid collected from the side-outlet is slightly higher than that of the inlet, while

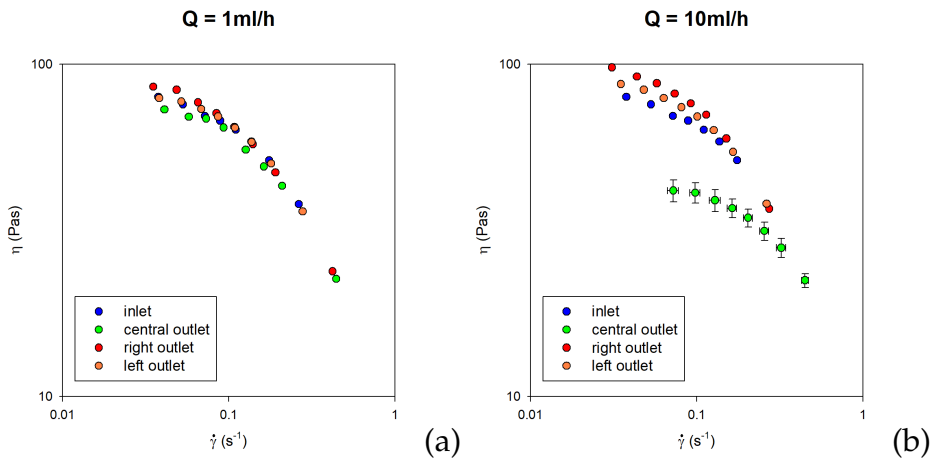

Fig. 6.3: *Viscosity of the samples collected from the outlet of the splitter (central (●), right (●) and left (●) outlet) respect to the viscosity of the model system (●): (a) Q = 1ml/h and (b) Q = 10ml/h*

the sample collected from the central-outlet shows a very low viscosity. This effect suggests a chemical demixing of the fluid under flow-conditions. Nevertheless, no considerations on the surfactant and/or salt-distributions can be based on these results. In fact, as already mentioned, the high viscoelasticity of a wormlike micellar solution is mainly ascribable to the interaction between salt and surfactant. For this reason, the low viscosity of the sample from the central-outlet can be related to both low salt or surfactant concentration.

In order to better understand the effective salt and surfactant-distributions, the electrical-conductivity of the samples has been measured.

First, two independent calibration-curves have been developed, by progressive-dilutions of a 0.1M solution of CTAB or NaSal.

Both calibration-curves show a linear relationship between the chemicals concentration and the electrical-conductivity; it is clear that,

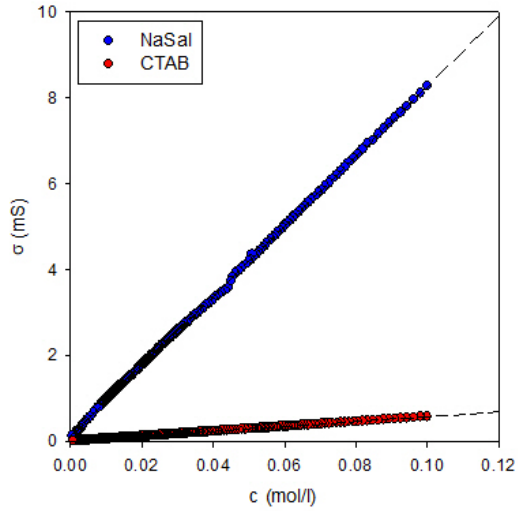

Fig. 6.4: *Calibration-curves for NaSal (●) and CTAB (●), and their linear fits (dashed lines)*

for given concentration, the NaSal affects the overall electrical-conductivity much more than the CTAB.

In view of this, it seems that there is no flow-induced concentration-gradient of Na^+ or Sal^-. In fact, regardless of the flow-rate, all the collected sample show the same electrical-conductivity (Tab.6.1).

Tab. 6.1: *Electrical-conductivity of the samples collected from the outlet of the splitter, respect to the electrical-conductivity of the model system*

Sample	**Dry-mass, mg/g**	
inlet	4.58	
	Q = 1ml/h	**Q = 10ml/h**
central-outlet	4.57	4.58
right-outlet	4.57	4.55
left-outlet	4.55	4.60

Nevertheless, the dry-mass measurement of the samples confirms a not-uniform distribution of the chemicals, as reported in Tab.6.2.

Tab. 6.2: *Dry-mass of the samples collected from the outlet of the splitter, respect to the dry-mass of the model system*

Sample	**Dry-mass, mg/g**	
inlet	30.07	
	Q = 1ml/h	**Q = 10ml/h**
central-outlet	30.60	22.05
right-outlet	29.43	36.83
left-outlet	30.40	38.61

In conclusion, by comparing the physical properties of the samples, it is possible to get information on the flow-behaviour of the model system. At high flow-rates, the solution flowing far from the walls shows the same electrical-conductivity of both the model system and the solution flowing close to the walls, but lower zero-viscosity and dry-mass.

Based on these data, it is possible to propose a mechanism in which the shear rate doesn't induce a demixing of Na^+ or Sal^-, but promotes surfactant-accumulation close to the walls.

The accumulation of micelles in one zone of the flow geometry is consistent with what Helfand and Fredrickson [51, 96] predicted for polymers, but the question whereas the high shear band corresponds or not to the concentrated one, is still open. In fact, from one hand there are only a few experimental papers reporting concentration-gradients, with the formation of an concentrated nematic phase [6, 52]; on the other hand, models proposed so far are contrasting one each other, and are developed on systems other than concentrated solution

of branched wormlike micelles [34, 40, 85, 99].

Conclusions

In this thesis, the flow-behaviour of a concentrated solution of branched wormlike micelles has been investigated, focusing the study on flow-induced phenomena within the stess pseudo-plateau.

Firstly, the rheology of the model system has been fully characterized:

- from oscillatory tests, the Maxwellian behaviour of the model system has been confirmed, and the relaxation time has been extracted;
- the flow curve over 11 decades of shear rate, and the oscillatory response over 6 decades of angular frequency, have been obtained by matching several techniques. Particularly interesting is the slow dynamic response of the system within the stress pseudo-plateau, that can be related to solution structuring;
- the wall-slip behaviour of the solution has been analysed, on both steel and glass surfaces. No slip-velocity has been detected on steel, whereas there is evidence of wall-slip phenomena when a glass geometry is used. This effect is lost when the characteristic length of the flow-geometry is above 500μm. The dependence of slip-velocity on shear stress has thus been measured and modelled;
- a rheometer-on-a-chip has been used to study the extensional

flow of the system;

- the possibility to measure structural parameters of the system using diffusive wave spectroscopy has been investigated.

Then, microfluidics has been coupled to advanced optical microscopy and to μPIV techniques, in order to analyse the flowing solution texture and to evaluate its velocity-profiles. At very low flow-rates, there is no evidence of flow-structuring in the solution, nor there is any discontinuity in the velocity-profile. As the flow-rate increases, shear-induced structures rise up, and a discontinuity-point in the velocity-profile has been detected and located at the interface between the homogeneous phase and the structured one. By further increase of the flow-rate, the velocity-profile becomes even more complex, showing several points of discontinuity. Birefringence analysis, lastly, has highlighted that such a structured phase is not related to an isotropic-to-nematic transition.

Results from microfluidics have been scaled-up to steel pipes. In order to separate the effect of changing the characteristic length and the material of the flowing geometry, both glass and steel pipes have been used, with different diameters and lengths. By fixing the flow-rate and measuring the pressure-drop, rheological data have been extracted. Regardless of the pipe material, all the measurements collapse on the same flow-curve, thus proving that the effect of slip-velocity can be neglected on the scale of 1mm. Furthermore, a complex rheological response has been detected when the wormlike micellar solution exits the stress pseudo-plateau.

Then, CFD analysis has been performed to stress out the difference between a pure-thinning behaviour and the detected response. Thus, the flow-behaviour of a pure-thinning fluid has been simulated, using both the measured flow-curve and the developed model for wall-slip.

When flow-structuring occurs, the predicted velocity-profiles are not consistent with the measured ones. Furthermore, the CFD analysis is not able to always predict the results from microfluidics, even if the macroscopic flow-texture is homogeneous. This suggests the onset of complex flow-phenomena on a scale smaller than 1μm.

Lastly, the possible occurrence of flow-induced concentration-gradients has been investigated, by using a complex flow-geometry, which allows the split of the solution flowing in diverse positions in the flow-channel. The analysis of the collected samples shows that the flow-rate doesn't have any impact on the local electrical-conductivity within the flow geometry. However, the flowing sample shows demixing-phenomena. In fact, both the zero-viscosity and the dry-mass far from the walls are lower respect to both the model system and the solution flowing close to the walls.

In conclusion, all the experiments highlights the non-trivial behaviour of a concentrated and highly-branched wormlike micellar solution showing a stress pseudo-plateau. Such a system shows the formation of shear-induced structures under strong-flow conditions; in non-branched micellar solutions, these structures are usually reported in dilute regime, whereas the shear banding is related to isotropic-to-nematic transition in the concentrated one, together with concentration-gradients and long under-damped rheological response at high Wi values. Both these latter have been detected in the investigated system, in which, however, there is no evidence of an isotropic-to-nematic transition, as highlighted by the analysis of the birefringent properties of the solution under flow.

Appendix A

Flow through PDMS channels

In the last decades, polydimethylsiloxane (PDMS) micro-channels have been extensively used to investigate the flow behaviour of worm-like micellar systems on micro-scale [19, 25, 37]. In fact, the fabrication of microfluidic devices in PDMS is easier and cheaper than in glass, and PDMS is transparent at optical frequencies, thus allowing the flow visualization.

Furthermore, new technologies as soft-lithography, based on printing patterns in soft polymeric molds, gives endless possibilities to fabricate very complex flow geometries.

Here, the possibility to use the PDMS to fabricate the splitter designed in Sec.6.2 is investigated. The advantages of such a PDMS splitter mainly concern the possibility to fabricate a number of flow geometries, characterized by different, changing the size of the channels. This would allow one to deduce the effective concentration profile within the channel.

The splitter is fabricated by using soft-lithography with SU-8 as photoresist [106]. Here, the height of the flow-geometry is 80μm, and Fig.A.1 shows the characteristic dimensions of the channels.

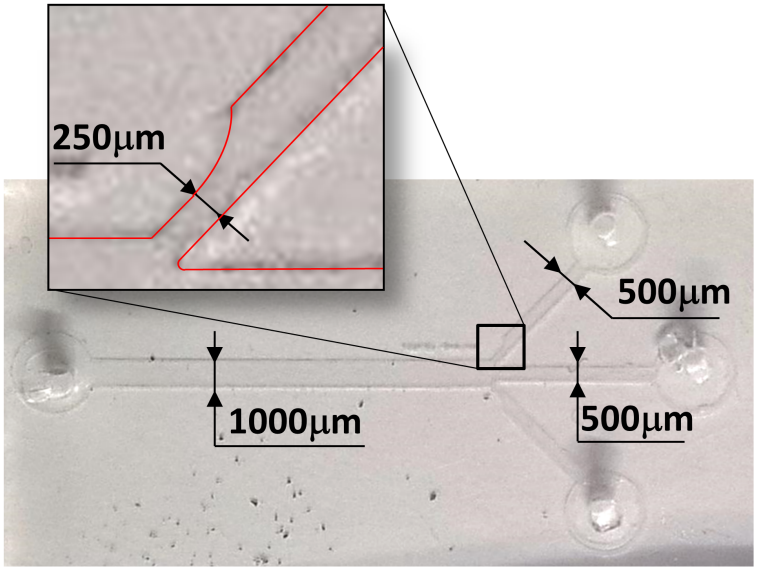

Fig. A.1: *PDMS splitter, and its characteristic dimensions*

The model system has been prepared as in Sec.2.2. The splitter has been connected through a 1mm inner-diameter ETFE tube (IDEX) to a micropump-system, consisting in a MFCSTM-FLEX pressure-driven flow-controller (FLUIGENT).

The solution flowing out the central channel and one side channel has been collected and stored for less than one day. The steady-state viscosity of the samples has been measured at 20°C in a controlled-stress rheometer (AR-G2, TA Instruments), equipped with a standard-steel cone geometry (D=25mm, cone angle=2°). Rheometer has been used in shear stress mode, and the samples have been conditioned for 60s at the desired temperature before each measurement.

FigA.2 shows the viscosity of the collected samples, as a function of the shear stress.

Regardless of the pressure drop, the viscosity of both the samples (from the central outlet and from the side outlet) is lower than that

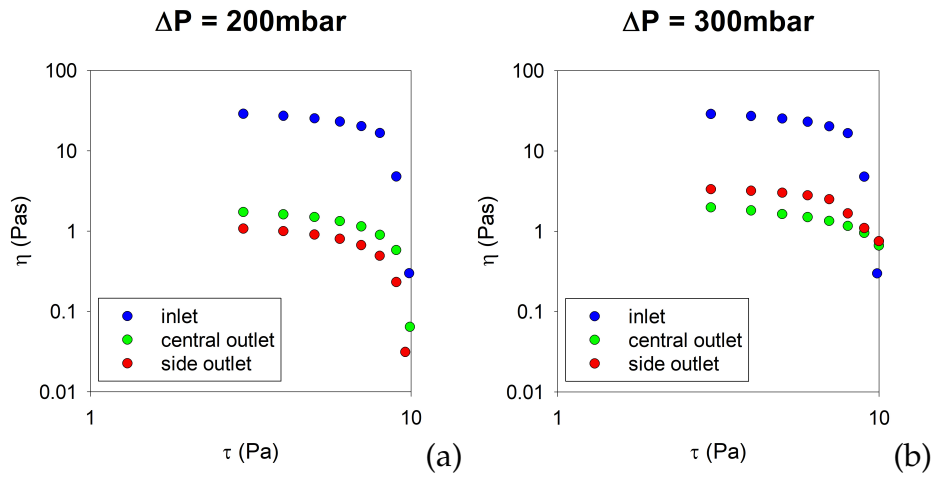

Fig. A.2: *Viscosity of the samples collected from the outlet of the splitter (central (●), and side (●) outlet) respect to the viscosity of the model system (●): (a) ΔP = 200mbar and (b) ΔP = 300mbar*

of the model system. Such an effect is consistent with flow-induced demixing. In fact, for example, in the extreme case in which all the surfactant moves toward the walls and all the salt moves toward the center of the channel, both the outlet would have lower viscosity respect to that of the inlet.

Nevertheless, in both the experiments, the two samples (from the central outlet and from the side outlet) show roughly the same viscosity; furthermore, lower the pressure-drop, lower the viscosity.

This considerations make one question whether the detected differences of viscosity can be really related to flow-induced demixing. In fact, the lower the pressure-drop, the lower the flow-rate, the higher the permanence-time, and thus the contact time between the model system and the PDMS. Thus, results in A.2 suggest a possible interaction between PDMS and one of the chemicals within the wormlike micellar solution.

In order to investigate this possibility, a cube (∼7mm*8mm*4mm, m = 0.5272g) of PDMS has been left to stay in 10ml of the model system. Two converslips (24mm*24mm each, m = 0.2418g each) have been left in other 10ml of the model system, for comparison. The solutions have been shaken for one week, after which the PDMS and the coverslips have been removed. Then, the steady-state viscosity of the samples has been measured at 20°C in a controlled-stress rheometer (MCR 702 TwinDrive, Anton-Paar), equipped with a standard-steel cone geometry (D=50mm, cone angle=1°). Rheometer has been used in shear rate mode, and the samples have been conditioned for 60s at the desired temperature before each measurement. FigA.3 shows the viscosity of the samples, respect to that of the model system.

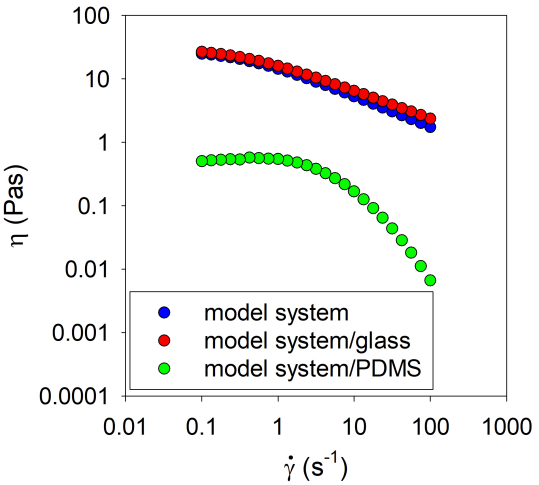

Fig. A.3: *Viscosity of the model system (●), after one week in contact with glass (●) and PDMS (●)*

The contact between the PDMS and the system, has lowered the zero-viscosity of this latter of almost 2 orders of magnitude; on the other hand, no effect can be appreciated when the model system is left in contact with glass. This effect shows the onset of strong interac-

tions between the PDMS and one or more chemicals within the sample. Understanding it this effect is related to absorption phenomena or chemical reactions, goes beyond the scope of this study.

It is worth underlining that, in absence of wall-slip phenomena, the permanence time of the solution close to the wall of a flow-channel is infinite. Thus, regardless of the flow rate, PDMS has always enought time to affect the composition of the solution close to the walls, whatever is the phenomenology at the base of their interaction.

For these reasons, using soft-litography to study a wormlike micellar system requires a proper functionalization of the PDMS, to remove any interaction with the flowing solution, or a different polymeric mold.

Appendix B

Flow between parallel plates

In this work, the flow-behaviour of a wormlike micellar solution has been investigated using a number of flow-geometries, such as microcapillary and pipes, plate-plate and cone-plate geometries in rotational rheometer, and microfluidic devices (rectangular slit, hyperbolic contraction, and 1-in-3 splitter).

Here, the response of the system under pure-shear flow conditions is investigated, by using a parallel plates setup.

The model system has been prepared as in Sec.3.2.1, without the addition of rhodamine B. Here, the system has been seeded with a solution of monodisperse polystyrene particles (d=4.5μm - Polysciences), whose concentration is 2.5% solid (1 drop every 25ml of solution).

The flow has been visualized in a parallel plates setup, described in details in [20] and references therein. Briefly, two optical-glass bars glued on optical glass slide are used as parallel plates. The movement of one of the slides ('moving plate') respect to the other ('fixed plate') provides the flow (Fig.B.1). When $H_2 \gg H_1$, wall effects are negligible, and pure-shear conditions can be assumed on the observation-plane. Here, in every experiment, H_1 = 0.7mm and H_2 = 3mm.

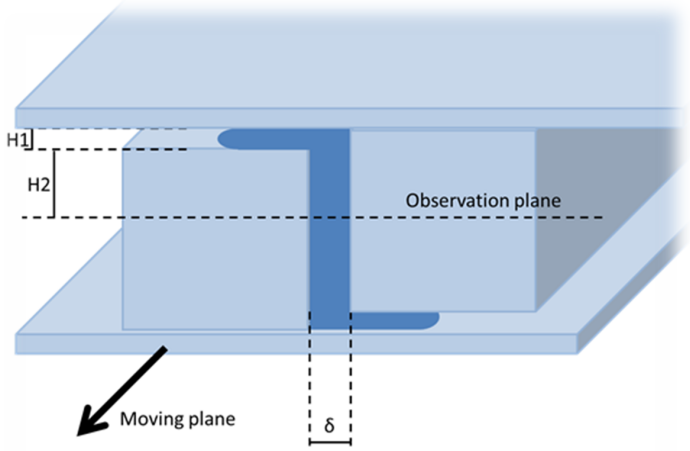

Fig. B.1: *Side-view of parallel plates setup with characteristic dimensions*

The dimensions of the glass bars here used are 10cm*10mm*10mm, and the solution is directly visualized from the top of the setup, using an EC Plan-Neofluar 20x/0.5 objective (Zeiss). Thus, here the flow is analysed along the velocity-vorticity direction.

The experimental procedure is:

1. the sample is loaded, and the gap between the plates is set (δ = 500µm);
2. the sample is left to relax for a couple of minutes;
3. a pre-shear has been applied for 10s, fixing v = 2mm/s;
4. the sample is left to relax for 15min;
5. a constant shear has been applied for 80s, fixing v = 2mm/s (run1);
6. steps 3 and 4 have been replicated;
7. step 5 has been replicated (run2).

Similarly to Sec.3.2.3, the tracking-procedure has been fully automated. The position of each particle has been detected off-line using the automatic Track Object, and the software MATLAB R2014b has

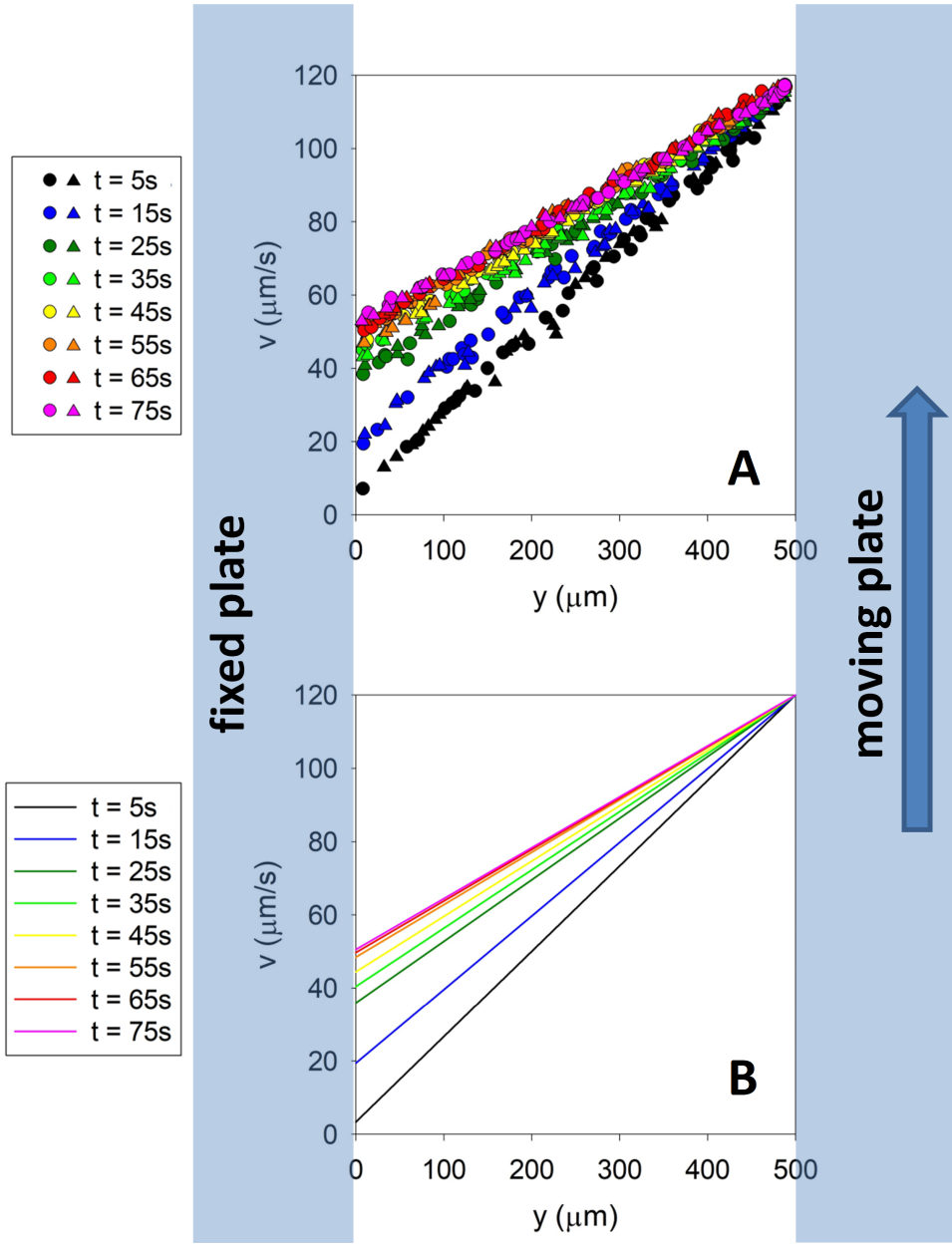

Fig. B.2: *Temporal evolution of the velocity profile in pure shear flow between glass parallel plates: (a) first (bullets) and second (triangles) run, and (b) fit of the data*

been used to write a custom code. First, the code divides the experimental time (80s) in 8 intervals of 10s, and groups the particles detected within the same interval. Then, it applies the Eq.3.1 to evaluate the velocity of each particle.

Fig.B.2 shows the so-obtained velocity-profiles as a function of time, and their linear fit. Here, the reported time is representative of the interval over which the profile is evaluated (e.g., t = 25s represents the interval 20-30s).

Wall-slip phenomena in complex fluids are usually modelled assuming equal slip-velocities on the two plates [38, 49, 55]. Here, the μPIV analysis highlights the onset of a condition of asymmetry, where the fluid slips on just one of the two plates.

It is worth underlining that this effect can't be related to structuring phenomena at very low scale, neither to shear banding, with the formation of a very thin band close to the fixed plate. In fact, the gap and velocity of the moving plate are such that $\dot{\gamma}_{fixed} = 0.24s^{-1}$, which is a value out of the stress pseudo-plateau.

A newtonian fluid has been used to check the reliability of the automatic measurement of the velocity-profile. Thus, 1 drop of solution of polystyrene particles has been dried, and the particles have been used to seed a silicon oil (Dow Corning 200 Fluid 12 500cSt); this latter has then been sheared for 180s between parallel plates, with δ = 500μm and v = 2mm/s.

As expected for a non-slip newtonian fluid under pure-shear flow, Fig.B.3 shows a triangular velocity-profile.

The behaviour of the model system can be easily modelled. In fact FigB.2 suggests a linear dependence of the velocity on the position y, for every time interval:

$$v = \dot{\gamma} y + v_{slip} \tag{B.1}$$

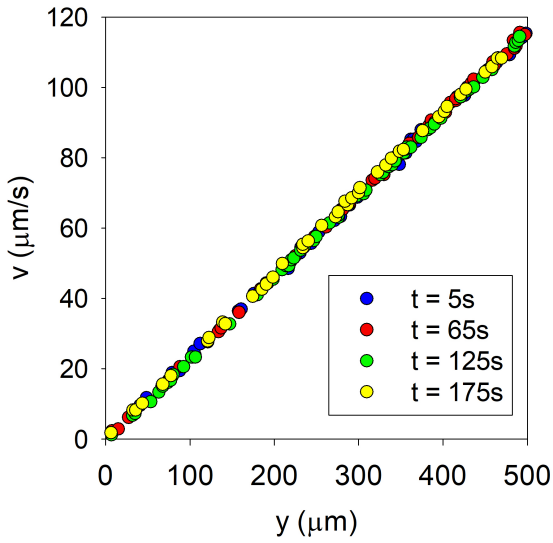

Fig. B.3: *Temporal evolution of the velocity profile of oil in pure shear flow between glass parallel plates*

where y is the distance from the fixed plate.

FigB.4 shows the values of shear rate, $\dot{\gamma}$, and slip velocity, v_{slip}, from Eq.B.1, for every time interval.

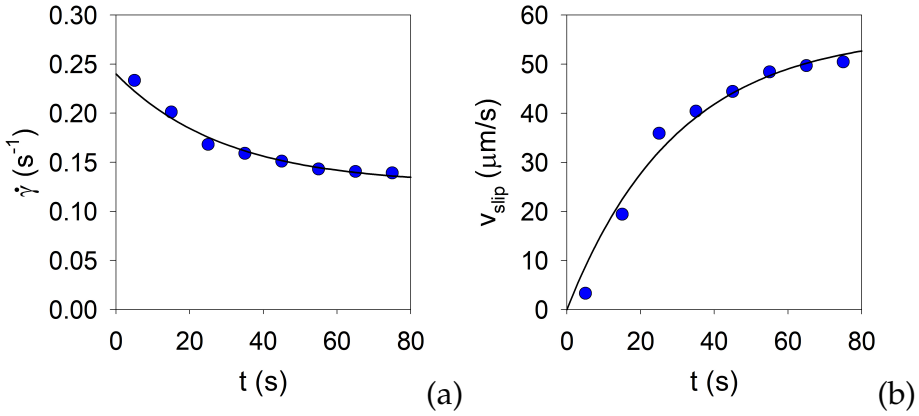

Fig. B.4: *Shear rate (a) and slip velocity (b) from fit of velocity profiles at given time interval: data (●) and fit (filled line)*

Data suggest an exponential decay of the shear rate in time, and an exponential growth of the slip velocity:

$$\dot{\gamma} = a + b * \exp\left(-\frac{t}{\tau_1}\right) \quad \dot{\gamma}\big|_{t=0} = 0.24\text{s}^{-1} \tag{B.2}$$

$$v_{slip} = c\left[1 - \exp\left(-\frac{t}{\tau_2}\right)\right] \tag{B.3}$$

Thus, the bivariate-fit used here for the velocity profile is:

$$v = \left[a + b * \exp\left(-\frac{t}{\tau_1}\right)\right] * y + c\left[1 - \exp\left(-\frac{t}{\tau_2}\right)\right] \qquad a + b = 0.24\text{s}^{-1} \tag{B.4}$$

Such a model properly fits all the data in Fig.B.2 when $a = 0.101\text{s}^{-1}$, $b = 0.139\text{s}^{-1}$, $c = 65.702\mu\text{m/s}$, and $\tau_1 = \tau_2 = 44.979\text{s}$. These values can be put in Eq.B.3 to estimate the time to reach steady state conditions, t_{ss}, for instance assuming that

$$v_{slip,ss} = 0.98 v_{slip}\big|_{t\to\infty} \tag{B.5}$$

hence

$$c\left[1 - \exp\left(-\frac{t_{ss}}{\tau_2}\right)\right] = 0.98c \tag{B.6}$$

where $v_{slip,ss}$ is the value of slip velocity in steady state conditions. Eq.B.6 gives $t_{ss} \sim 176\text{s}$.

As already depicted, each velocity profiles in Fig.B.2 is an average on 10s. The analysis of the instantaneous velocity of the single particles highlights a more complex behaviour.

Fig.B.5 shows the instantaneous velocity of particles at a given position (y = 230μm), together with the values predicted from Eq.B.4.

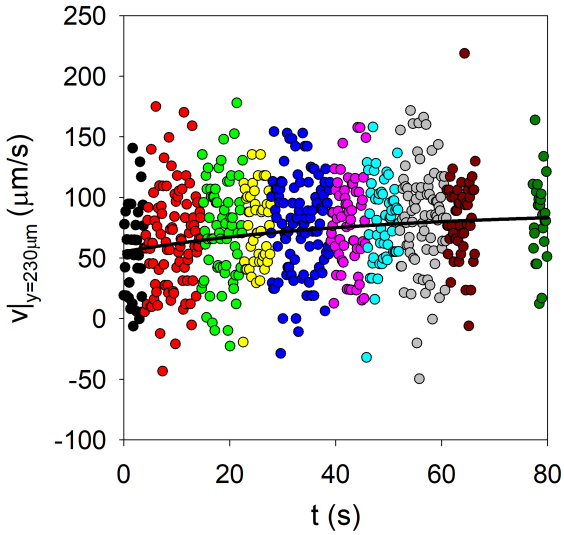

Fig. B.5: *Instantaneous velocity of particles at $y = 230\mu m$ (bullets, different colours refer to different particles), and prediction from bivariate-fit*

Particles continuously accelerate and decelerate, and in some moments their velocity is negative, as they move in the opposite direction, respect to that of the moving plate.

In order to investigate the relationship between this behaviour and the elastic component of the model system, an highly-elastic Boger fluid has been tested. Here, the fluid has been prepared as suggested by Caserta et al. [20], replacing the Indopol 100 with Indopol 50 (BP Chemicals). Then, similarly to what has been done with the oil, 1 drop of solution of polystyrene particles has been dried, and the particles have been used to seed the fluid; this latter has then been sheared for 180s between parallel plates, with $\delta = 500\mu m$ and $v = 2mm/s$.

The Boger fluid doesn't show any wall-slip phenomenon, neither temporal fluctuations of the instantaneous velocity of the particles (Fig.B.6). Thus, the uncommon temporal response of the wormlike micellar system under pure-shear flow can't be simply considered as

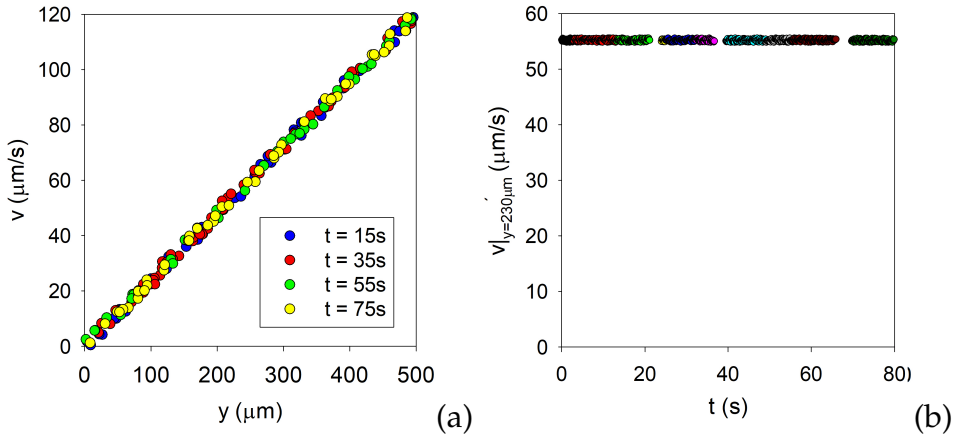

Fig. B.6: *Pure shear flow of a Boger fluid: (a) temporal evolution of the velocity profile, and (b) instantaneous velocity of particles at y = 230μm (different colours refer to different particles)*

a result of its elastic component.

In conclusion, the study of the flow-behaviour of the model system under pure-shear flow has highlighted that, in this specific geometry, wall-slip is not negligible when δ = 500μm; μPIV shows the development of an asymmetric velocity profile after long transients, and fluctuations of the tracers, which can't be related only to the elastic-behaviour of the system.

Bibliography

[1] Appell J., Porte G., Khatory A., Kern F., Candau S. J., Static and Dynamic Properties of a Network of Wormlike Surfactant Micelles (Cetylpyridinium Chlorate in Sodium Chlorate Brine), J. Phys. II France 2 (1992) 1045-1052

[2] Baravian C., Quemada D., Using Instrumental Inertia in Controlled Stress Rheometry, Rheol. Acta 37 (1998) 223-233

[3] Barhoum S., Castillo R., Yethiraj A., Characterization of Dynamics and Internal Structure of a Mixed-Surfactant Wormlike Micellar System Using NMR and Rheometry, Soft Matter 8 (2012) 6950-6957

[4] Berret J. F., Appell J., Porte G., Linear Rheology of Entangled Wormlike Micelles, Langmuir 9 (1993) 2851-2854

[5] Berret J. F., Roux D. C., Porte G., Isotropic-to-Nematic Transition in Wormlike Micelles Under Shear, J. Phys. II France 4 (1994) 1261-1279

[6] Berret J. F., Roux D., Porte G., Lindner P., Shear-Induced Isotropic-To-Nematic Phase Transition in Equilibrium Polymers, Europhys. Lett. 25 (1994) 521-526

[7] Berret J. F., Transient Rheology of Wormlike Micelles, Langmuir 13 (1997) 2227-2234

[8] Berret J. F., Roux D. C., Lindner P., Structure and Rheology of Concentrated Wormlike Micelles at the Shear-Induced Isotropic-to-Nematic Transition, Eur. Phys. J. B 5 (1998) 67-77

[9] Berret J. F., Porte G., Metastable Versus Stable Transients at the Onset of a Shear-Induced Phase Transition, Phys. Rev. E 60 (1999) 4268-4271

[10] Berret J. F., Rheology of Wormlike Micelles: Equilibrium Properties and Shear Banding Transitions. In: Weiss R. G., Terech P. (eds.) Molecular Gels: Material with Self-Assembled Fibrillar Networks, Springer, Dordrecht, 2005

[11] Britton M. M., Mair R. W., Lambert R. K., Callaghan P. T., Transition to Shear Banding in Pipe and Couette Flow of Wormlike Micellar Solutions, J. Rheol. 43 (1999) 897-909

[12] Britton M. M., Callaghan P. T., Shear Banding Instability in Wormlike Micellar Solutions, Eur. Phys. J. B 7 (1999) 237-249

[13] Calabrese M. A., Rogers S. A., Murphy R. P., Wagner N. J., The Rheology and Microstructure of Branched Micelles Under Shear, J. Rheol. 59 (2015) 1299-1328

[14] Calabrese M. A., Wagner N. J., Rogers S., Porcar L. (2017) The Effect of Branching on Shear Band Formation and Evolution in Wormlike Micelles (WLMs). In: 2017 AIChE Annual Meeting

[15] Calabrese M., Wagner N. J., New Insights from Rheo-small-angle Neutron Scattering. In: Herb C., Dreiss C. A., Feng Y. (eds)

Wormlike Micelles: Advances in Systems, Characterisation and Applications, RSC, Cambridge (2017)

[16] Candau S. J., Khatory A., Lequeux F., Kern F., Rheological Behaviour of Wormlike Micelles: Effect of Salt Content, J. Phys. IV 03 (1993) C1-197-C1-209

[17] Cappelaere E., Cressely R., Decruppe J. P., Linear and Non-Linear Rheological Behaviour of Salt-Free Aqueous CTAB Solutions, Colloids Surf. A 104 (1995) 353-374

[18] Cardiel J. J., Dohnalkova A. C., Dubash N., Zhao Y., Cheung P., Shen A. Q., Microstructure and Rheology of a Flow-Induced Structured Phase in Wormlike Micellar Solutions, PNAS 110 (2013) E1653-E1660

[19] Cardiel J. J., Zhao Y., De La Iglesia P., Pozzo L. D., Shen A. Q., Turning Up the Heat on Wormlike Micelles With a Hydrotropic Salt in Microfluidics, Soft Matter 10 (2014) 9300-9312

[20] Caserta S., D'Avino G., Greco F., Guido S., Maffettone P. L., Migration of a Sphere in a Viscoelastic Fluid Under Planar Shear Flow: Experiments and Numerical Predictions, Soft Matter 7 (2011) 1100-1106

[21] Cates M. E., Reptation of Living Polymers: Dynamics of Entangles Polymers in the Presence of Reversible Chain-Scission Reactions, Macromolecules 20 (1987) 2289-2296

[22] Cates M. E., Candau S. J., Statics and Dynamics of Worm-Like Surfactant Micelles, J. Phys.: Condens. Matter 2 (1990) 6869-6892

[23] Cates M. E., Fieldings S. M., Rheology of Giant Micelles, Adv. Phys. 55 (2006) 799-879

[24] Chellamuthu M., Rothstein J. P. Distinguishing Between Linear and Branched Wormlike Micelle Solutions Using Extensional Rheology Measurements, J. Rheol. 52 (2008) 865-884

[25] Cheung P., Dubash N., Shen A. Q., Locel Micelle Concentration Fluctuations in Microfluidic Flow and Its Relation to a Flow-Induced Structured Phase (FISP), Soft Matter 7 (2012) 2304-2309

[26] Chu Z., Dreiss C. A., Feng C., Smart Wormlike Micelles, Chem. Soc. Rev. 42 (2013) 7174-7203

[27] Cicuta P., Donald A. M., Microrheology: A Review of the Method and Applications, Soft Matter 3 (2007) 1449-1455

[28] Clasen C., McKinley G. H., Gap-Dependent Microrheometry of Complex Liquids, J. Non-Newtonian Fluid Mech. 124 (2004) 1-10

[29] Connelly R. W., Greener J., High-Shear Viscometry with a Rotational Parallel-Disk Device, J. Rheol. 29 (1985) 209-226

[30] Davies G. A., Stokes J. R., On the Gap Error in Parallel Plate Rheometry that Arises from the Presence of Air when Zeroing the Gap, J. Rheol. 49 (2005) 919-922

[31] Davies G. A., Stokes J. R., Thin Film and High Shear Rheology of Multiphase Complex Fluids, J. Non-Newtonian Fluid Mech. 148 (2008) 73-87

[32] de Gennes P. G., Scaling Concepts in Polymer Physics, Cornell University Press, Ithaca (1979)

[33] Delgado J., Kriegs H., Castillo R., Flow Velocity Profiles and Shear Banding Onset in Semidilute Wormlike Micellar System Under Couette Flow, J. Phys. Chem. B 113 (2009) 15485-15494

[34] Dhont J. K. G., Briels W. J., Gradient and Vorticity Banding, Rheol. Acta 47 (2008) 257-281

[35] Dimitriou C. J., Casanellas L., Ober T. J., Rheo-PIV of a Shear-Banding Wormlike Micellar Solution Under Large Amplitude Oscillatory Shear, Rheol. Acta 51 (2012) 395-411

[36] Douglass B. S., Colby R. H., Madsen L. A., Callaghan P. T., Rheo-NMR of Wormlike Micelles Formed from Nonionic Pluronic Surfactants, Macromolecules 41 (2008) 804-814

[37] Dubash N., Cardiel J., Cheung P., Shen A. Q., A Stable Flow-Induced Structured Phase in Wormlike Micellar Solutions, Soft Matter 7 (2011) 876-879

[38] Durairaj R., Man L. W., Ekere N. N., Mallik S., The Effect of Wall-Slip Formation on the Rheological Behaviour of Lead-Free Solder Pastes, Mater. Des. 31 (2010) 1056-1062

[39] Einaga Y., Ebihara M., Uchida R., Wormlike Micelles of Hexaoxyethylene Decyl $C_{10}E_6$ and Tetradecyl $C_{14}E_6$ Ethers Containing *n*-Dodecanol, Polym. J. 39 (2007) 792-801

[40] Fielding S. M., Olmsted P. D., Flow Phase Diagrams for Concentration-Coupled Shear Banding, European Physical Journal E 11 (2003) 65-83

[41] Fischer E., Callaghan P. T., Shear Banding and the Isotropic-to-Nematic Transition in Wormlike Micelles, Phys. Rev. E Physical Review E 011501

[42] Frounfelker B. D., Kalur G. C., Cipriano B. H., Danino D., Raghavan S. R., Persistence of Birefringence in Sheared Solutions of Wormlike Micelles, Langmuir 25 (2009) 167-172

[43] Galvan-Miyoshi J., Delgado J., Castillo R., Diffusing Wave Spectroscopy in Maxwellian Fluids, Eur. Phys. J. E 26 (2008) 369-377

[44] Gardel M. L., Valentine M. T., Weitz D. A., Microrheology. In: Breuer K. (ed) Microscale Diagnosis Techniques, Springer, Berlin (2005)

[45] Grand C., Arraule J., Cates M. E., Slow Transient and Metastability in Wormlike Micelle Rheology, J. Phys. II France 7 (1997) 1071-1086

[46] Granek R., Cates M. E., Stress Relaxation in Living Polymers: Results from a Poisson Renewal Model, J. Chem. Phys. 96 (1992) 4758-4767

[47] Gurnon A. K., Lopez-Barron C., Wasbrough M. J., Porcar L., Wagner N. J., Spatially Resolved Concentration and Segmental Flow Alignment in a Shear-Banding Solution of Polymer-Like Micelles, ACS Macro Lett. 3 (2014) 276-280

[48] Hartmann V., Cressely R., Occurrence of Shear Thickening in Aqueous Micellar Solutions of CTAB with Some Added Organic Counterions, Colloid Polym. Sci. 276 (1998) 169-175

[49] Hatzikiriakos S. G., Wall Slip of Molten Polymers, Prog. Polym. Sci. 37 (2012) 624-643

[50] Haward S. J., McKinley G. H., Stagnation Point Flow of Wormlike Micellar Solutions in a Microfluidic Cross-Slot Device: Ef-

fects of Surfactant Concentration and Ionic Environment, Phys. Rev. E 85 (2012) 031502

[51] Helfand E., Fredrickson G. H., Large Fluctuations in Polymer Solutions Under Shear, Physical Review Letters 62 (1989) 2468-2471

[52] Helgeson M. E., Porcar L., Lopez-Barron C., Wagner N. J., Direct Observation of Flow-Concentration Coupling in a Shear-Banding Fluid, Phys. Rev. Lett. 105 (2010) 084501

[53] Henson D. J., Mackay M. E., Effect of Gap on the Viscosity of Monodisperse Polystyrene Melts: Slip Effects, J. Rheol. 39 (1995) 359-373

[54] Herle V. Kohlbrecher J., Pfister B., Fischer P., Windhab E. J., Alternating Vorticity Bands in a Solution of Wormlike Micelles, Phys. Rev. Lett. 99 (2007) 158302

[55] Himmel T., Wagner M. H., Experimental Determination of Interfacial Slip Between Polyethylene and Thermoplastic Elastomers, J. Rheol. 57 (2013) 1773-1785

[56] Hu Y. T., Boltenhagen P., Shear Thickening in Low-Concentration Solutions of Wormlike Micelles. I. Direct Visualization of Transient Behavior and Phase Transition, J. Rheol. 42 (1998) 1185-1208

[57] Hu Y. T., Lips A., Kinetics and Mechanism of Shear Banding in an Entangled Micellar Solution, J. Rheol. 49 (2005) 1001-1027

[58] Hu Y. T., Palla C., Lips A., Comparison Between Shear Banding and Shear Thinning in Entangled Micellar Solutions, J. Rheol. 52 (2008) 379-400

[59] Israelachvili J. N., Intermolecular and Surface Forces, Academic Press, New York (1992)

[60] Kadoma I. A., van Egmond J. W., Shear-Enhanced Orientation and Concentration Fluctuations in Wormlike Micelles: Effect of Salt, Langmuir 13 (1997) 4551-4561

[61] Kalur G. C., Raghavan S. R., Anionic Wormlike Micellar Fluids that Display Cloud Points: Rheology and Phase Behavior, J. Phys. Chem. B 109 (2005) 8599-8604

[62] Kang K., Lee J., Koelling K. W., High Shear Microfluidics and Its Applications in Rheological Measurement, Exp. Fluids 38 (2005) 222-232

[63] Kern F., Lequeux F., Zana R., Candau S. J., Dynamic Properties of Salt-Free Viscoelastic Micellar Solutions, Langmuir 10 (1994) 1714-1723

[64] Khatory A., Lequeux F., Kern F., Candau S. J., Linear and Nonlinear Viscoelasticity of Semidilute Solutions of Wormlike Micelles at High Salt Content, Langmuir 9 (1993) 1456-1464

[65] Kim N. J., Pipe C. J., Ahn K. H., Lee S. J., McKinley G. H., Capillary Breakup Extensional Rheometry of a Wormlike Micellar Solution, Korea-Aust. Rheol. J., 22 (2010) 31-41

[66] Transient, Near-Wall Shear-Band Dynamics in Channel Flow of Wormlike Micelle Solutions, J. Nonnewton. Fluid Mech. 232 (2016) 77-87

[67] Koehler R. D., Raghavan S. R., Kaler E. W., Microstructure and Dynamics of Wormlike Micellar Solutions Formed by Mixing

Cationic and Anionic Surfactants, J. Phys. Chem. B 104 (2000) 11035-11044

[68] Kuczera S., Perge C., Fardin M.-A., Brox T. I., Williams M. A. K., Manneville S., Galvosas P., Anomalous Shear Banding Revisited with Rheo-NMR and Rheo-USV, Rheol. Acta 54 (2015) 619-636

[69] Lequeux F., Reptation of Connected Wormlike Micelles, Europhys. Lett. 19 (1992) 675-681

[70] Lequeux F., Candau S. J., Dynamical Properties of Wormlike Micelles. In: Herb C., Prudhomme R. (eds) Structure and Flow in Surfactant Solutions, ACS Symposium Series 578, Am. Chem. Soc., Washington DC (1994)

[71] Lettinga M. P., Manneville S., Competition Between Shear Banding and Wall Slip in Wormlike Micelles, Phys. Rev. Lett. 103 (2009) 248302

[72] Liberatore M. W., Nettesheim F., Wagner N. J., Spatially Resolved Small-Angle Neutron Scattering in the 1-2 Plane: A Study of Shear-Induced Phase-Separating Wormlike Micelles, Phys. Rev. E 73 (2006) 020504

[73] Lopez-Diaz D., Castillo R., Microrheology of Solutions Embedded with Thread-Like Supramolecular Structures, Soft Matter 7 (2011) 5926-5937

[74] Lopez-Gonzalez M. R., Holmes W. M., Callaghan P. T., Rheo-NMR Phenomena of Wormlike Micelles, Soft Matter 2 (2006) 855-869

[75] Macosko C. W., Rheology, Principles, Measurements and Applications, VCH, New York, 1994

[76] Marques C. M., Turner M. S., Cates M. E., Relaxation Mechanisms in Worm-Like Micelles, J. Non-Cryst. Solids 172-174 (1994) 1168-1172

[77] Mason T. G., Estimating the Viscoelastic Moduli of Complex Fluids Using the Generalized Stokes-Einstein Equation, Rheol. Acta 39 (2000) 371-378

[78] Masselon C., Salmon J. B., Colin A., Nonlocal Effects in Flow of Wormlike Micellar Solutions, Phys. Rev. Lett 100 (2008) 038301

[79] Miller E., Rothstein J. P., Transient Evolution of Shear-Banding Wormlike Micellar Solutions, J. of Non-Newtonian Fluid Mech. 143 (2007) 22-37

[80] Mohammadigoushki H., Muller S. J., A Flow Visualization and Superposition Rheology Study of Shear-Banding Wormlike Micelles Solutions, Soft Matter 12 (2016) 1051-1061

[81] Nagarajan R., Molecular Packing Parameter and Surfactant Self-Assembly: the Neglected Role of the Surfactant Tail, Langmuir 18 (2002) 31-38

[82] Ober T. J., Soulages J., McKinley G. H., Spatially Resolved Quantitative Rheo-Optics of Complex Fluids in a Microfluidic Device, J. Rheol 55 (2011) 1127-1159

[83] Ober T. J., Haward S. J., Pipe C. J., Soulages J., McKinley G. H., Microfluidic Extensional Rheometry Using a Hyperbolic Contraction Geometry, Rheol. Acta 52 (2013) 529-546

[84] Oelaschlaeger C., Schopferer M., Scheffold F., Willenbacher N., Linear-To-Branched Micelles Transition: A Rheometry and Diffusing Wave Spectroscopy Study, Langmuir 25 (2009) 716-723

[85] Olmsted P. D., Lu C.-Y. D., Phase Separation of Rigid-Rod Suspensions in Shear Flow, Physical Review E 60 (1999) 4397-4415

[86] Olmsted P. D., Radulescu O., Lu C. Y. D., The Johnson-Segalman Model with a Diffusion Term in Cylindrical Couette Flow, J. Rheol. 44 (2000) 257-275

[87] Parker A., Fieber W., Viscoelasticity of Anionic Wormlike Micelles: Effects of Ionic Strength and Small Hydrophobic Molecules, Soft Matter 9 (2013) 1203-1213

[88] Pipe C. J., Majmudar T. S., McKinley G. H., High Shear Rate Viscometry, Rheol. Acta 47 (2008) 621-642

[89] Preziosi V., Tarabella G., D'Angelo P., Romeo A., Barra M., Guido S., Cassinese A., Iannotta S., Real-Time Monitoring of Self-Assembling Worm-Like Micelle Formation by Organic Transistors, RSC Adv. 5 (2015) 16554-16561

[90] Prud'homme R. K., Warr G. G., Elongational Flow of Solutions of Rodlike Micelles, Langmuir 10 (1994) 3419-3426

[91] Raghavan S. R., Fritz G., Kaler E. W., Wormlike Micelles Formed by Synergistic Self-Assembly in Mixtures of Anionic and Cationic Surfactants, Langmuir 18 (2002) 3797-3803

[92] Rehage H., Hoffmann H., Rheological Properties of Viscoelastic Surfactant Systems, J. Phys. Chem. 92 (1988) 4712-4719

[93] Rehage H., Hoffmann H., Viscoelastic Surfactant Solutions: Model System for Rheological Research, Mol. Phys. 74 (1991) 933-973

[94] Rogers S. A., Calabrese M. A., Wagner N. J., Rheology of Branched Wormlike Micelles, Curr. Opin. Colloid Interface Sci. 19 (2014) 530-535

[95] Rothstein J. P., Transient Extensional Rheology of Wormlike Micelle Solutions, J. Rheol. 47 (2005) 1227-1247

[96] Rothstein J. P., Strong Flows of Viscoelastic Wormlike Micelle Solutions, In: Binding D. M., Walters K. (eds.) Rheology Reviews, The British Society of Rheology, Aberystwyth, 2008

[97] Salmon J. B., Colin A., Manneville S., Molino F., Velocity Profiles in Shear-Banding Wormlike Micelles, Phys. Rev. Lett. 90 (2003) 228303

[98] Schmitt V., Lequeux F., Pousse A., Roux D., Flow Behavior and Shear Induced Transition near an Isotropic/Nematic Transition in Equilibrium Polymers, Langmuir 10 (1994) 955-961

[99] Schmitt V., Marques C. M., Lequeux F., Shear-Induced Phase Separation of Complex Fluids: The Role of Flow-Concentration Coupling, Phys. Rev. E 52 (1995) 4009-4015

[100] Schubert B. A., Wagner N. J., Kaler E. W., Raghavan S. R., Shear-Induced Phase Separation in Solutions of Wormlike Micelles, Langmuir 20 (2004) 3564-3573

[101] Sheely M. L., Glycerol Viscosity Tables, Ind. Eng. Chem. 24 (1932) 1060-1064

[102] Shikata T., Hirata H., Micelle Formation of Detergent Molecules in Aqueous Media: Viscoelastic Properties of Aqueous Cetyltrimethylammonium Bromide Solutions, Langmuir 3 (1987) 1081-1086

[103] Shikata T., Hirata H., Takatori E., Osaki K., Nonlinear Viscoelastic Behavior of Aqueous Detergent Solutions, J. Nonnewton. Fluid Mech. 28 (1988) 171-182

[104] Smith M. L., Long D. S., Smith M. L., Long D. S., Damiano E. R., Ley K., Near-Wall Micro-PIV Reveals a Hydrodynamically Relevant Endothelial Surface Layer in Venules in Vivo, Biophys. J., 85 (2003) 637-645

[105] Spenley N. A., Cates M. E., McLeish T. C. B., Non-linear Rheology of Wormlike Micelles, Phys. Rev. Lett. 71 (1993) 939-942

[106] Tomaiuolo G., Barra M., Preziosi V., Cassinese A., Rotoli B., Guido S., Microfluidics Analysis of Red Blood Cell Membrane Viscoelasticity, Lab Chip 11 (2011) 449-454

[107] Turner M. S., Cates M. E., Linear Viscoelasticity of Wormlike Micelles: A Comparison of Micellar Reaction Kinetics, J. Phys. II France (1992) 503-519

[108] Turner M. S., Marques C. M., Cates M. E., Dynamics of Wormlike Micelles: the 'Bond-Interchange' Reaction Scheme, Langmuir 9 (1993) 695-701

[109] Yamashita A., Mori K., Sawa K., Yamamoto T., Creep Tests, Flow Birefringence Measurements, and Flow Visualization of Aqueous Solutions of CTAB and NaSal in Shear Flow between Parallel Plates, JFST 4 (2009) 699-710

[110] Yan Z. Dai C., Feng H., Liu Y., Wang S., Study of the Formation and Solution Properties of Worm-Like Micelles Formed Using Both *N*-Hexadecyl-*N*-Methylpiperidinium Bromide-Based

Cationic Surfactant and Anionic Surfactant, PLoS ONE 9 (2014) e110155

[111] Yang J., Viscoelastic Wormlike Micelles and Their Applications, Curr. Opin. Colloid Interface Sci. 7 (2002) 276-281

[112] Yesilata B., Clasen C., McKinley G. H., Non-linear Shear and Extensional Flow Dynamics of Wormlike Surfactant Solutions, J. Non-Newtonian Fluid Mech. 133 (2006) 73-90

[113] Walker L. M., Moldenaers P., Berret J.-F., Macroscopic Response of Wormlike Micelles to Elongational Flow, Langmuir 12 (1996) 6309-6314

[114] Walker L. M., Rheology and Structure of Worm-Like Micelles, Curr. Opin. Colloid Interface Sci. 6 (2001) 451-456

[115] Zana R., Kaler E. W., Giant Micelles: Properties and Applications, CRC Press, Boca Raton (2007)

[116] Zhang J., Wang Y., Xu G., Lin M., Fan T., Yang Z., Dong Z., Formation and Rheological Behavior of Wormlike Micelles in a Catanionic System of Fluoroacetic Acid and Tetradecyldimethylaminoxide, Soft Matter 13 (2017) 670-676

[117] Zhao Y., Cheung P., Shen A. Q., Microfluidic Flows of Wormlike Micellar Solutions, Adv. Colloid Interface Sci. 211 (2014) 34-46

[118] Zhao Y., Haward S. J., Shen A. Q., Rheological Characterizations of Wormlike Micellar Solutions Containing Cationic Surfactant and Anionic Hydrotropic Salt, J. Rheol. 59 (2015) 1229

[119] Zhao Y., Shen A. Q., Haward S. J., Flow of Wormlike Micellar Solutions Around Confined Microfluidic Cylinders, Soft Matter 12 (2016) 1051-1061

[120] Zhou L., Cook L. P., McKinley G. H., Multiple Shear-Banding Transitions for a Model of Wormlike Micellar Solutions, SIAM Appl. Math. 72 (2012), 11921212

[121] Ziserman L., Abezgauz L., Ramon O., Raghavan S. R., Danino D., Origins of the Viscosity Peak in Wormlike Micellar Solutions. 1. Mixed Cationic Surfactants. A Cryo-Transmission Electron Microscopy Study, Langmuir 25 (2009) 10483-10489

[122] Zou W., Tang X., Weaver M., Koenig P., Larson R. G., Determination of Characteristic Lengths and Times for Wormlike Micelle Solutions from Rheology Using a Mesoscopic Simulation Method, J. Rheol. 59 (2015) 903-934

[123] http://www.rheosense.com/hs-fs/hub/296746/file-2438655427-pdf/Application/_Notes/VROC/_-_Principle.pdf?t=1505263431707

[124] http://www.rheosense.com/hubfs/Application_Notes/Extensional_Viscosity/Shear%20Correction%20to%20Extensional%20Viscosity%20App%20%20Finalv2.pdf?t=1505263431707

[125] https://ibidi.com/channel-slides/55--slide-iii-3in1.html

[126] https://ibidi.com/img/cms/products/labware/channel_slides/S_8031X_Slide_III3in1/IN_8031X_III_3in1.pdf